Centre Énergie Matériaux Télécommunications

Design and Analysis of Dual-Band Mode-Switchable OAM Antenna for Integrated Microwave and Millimeter-Wave Systems

Par

Huifang Wu

Mémoire présenté pour l'obtention du grade de
Maître ès Sciences (M.Sc.)
en télécommunications

Jury d'évaluation

Président du jury et examinateur interne	Prof. Serioja Ovidiu Tatu *INRS-ÉMT*
Examinateur externe	Prof. Chan-Wang Park *Université de Québec à Rimouski (UQAR)*
Directeur de recherche	Prof. Tayeb A. Denidni *INRS-ÉMT*

©Huifang Wu, June 2025

Acknowledgments

First and foremost, I would like to express my sincere and profound gratitude to my supervisor, Prof. Tayeb A. Denidni, for his exceptional guidance, constant support, and insightful feedback throughout my master's studies. His mentorship has played a pivotal role in shaping this research.

I am also deeply thankful to my colleagues and collaborators, whose discussions, suggestions, and encouragement have greatly contributed to this work. I am grateful to the faculty members and administrative staff at INRS for fostering a welcoming and intellectually stimulating environment.

I wish to extend special thanks to my family and friends for their unconditional love, patience, and continuous encouragement. Their support has been a vital source of motivation and strength throughout this journey.

Finally, I gratefully acknowledge the examiners for their time and valuable feedback, which significantly improved the quality of this thesis.

To everyone who has accompanied me in any way during this academic endeavor—thank you.

Résumé

Avec l'avancée rapide des technologies de communication sans fil, en particulier avec le développement de la 5G et des générations suivantes, la demande en transmission à haute capacité et en efficacité spectrale accrue a considérablement augmenté. L'intégration des bandes de fréquences micro-ondes et millimétriques (mm-wave) s'avère essentielle pour les systèmes de communication de nouvelle génération, car elle permet une transmission de données à haut débit et une amélioration des performances réseau. Les antennes capables de générer des modes à moment angulaire orbital (OAM) suscitent un grand intérêt en raison de leur capacité à améliorer l'efficacité spectrale et à accroître la capacité de transmission en exploitant des modes d'onde spatiaux orthogonaux. Toutefois, les conceptions d'antennes multi-bandes classiques, y compris celles fonctionnant à la fois dans les bandes micro-ondes et millimétriques, peinent souvent à assurer un fonctionnement multi-bande efficace tout en restant compatibles avec les modes OAM. Par conséquent, la conception d'antennes capables à la fois de générer des modes OAM et de fonctionner efficacement sur plusieurs bandes de fréquences représente un enjeu de recherche majeur, car elle peut considérablement améliorer la capacité des systèmes sans fil et leur efficacité spectrale.

Pour répondre à ces défis, ce mémoire présente la conception, l'optimisation, la fabrication et la validation expérimentale d'une antenne OAM bi-bande à commutation de mode, capable de fonctionner à 5.8 et 28 GHz. Le système d'antenne proposé est composé de deux réseaux circulaires uniformes (UCAs), chacun utilisant une configuration à double port. En excitant sélectivement un port tout en adaptant l'autre par une charge de 50 Ω, une génération stable et efficace de modes OAM de charges topologiques $l = \pm 1$ est obtenue. Cette configuration permet la commutation des modes OAM sur deux bandes sans nécessiter de circuits de déphasage externes. Le schéma simplifié à double port facilite non seulement la commutation de mode, mais permet également d'ajuster la fréquence de fonctionnement en adaptant les dimensions physiques de l'antenne, ce qui démontre la scalabilité du concept proposé. Dans l'ensemble, cette approche répond aux limites des antennes OAM multi-bandes traditionnelles et démontre la faisabilité d'intégrer les fonctionnalités OAM dans les futurs systèmes de communication sans fil.

Afin de valider l'efficacité de l'antenne proposée, des simulations numériques ont été réalisées à l'aide de CST Microwave Studio pour analyser les paramètres clés, notamment les paramètres S, les fronts de phase, l'amplitude et les diagrammes de rayonnement en champ lointain. Les résultats de simulation confirment que l'antenne permet une génération stable de modes OAM sur les deux bandes de fréquences. Pour valider davantage la faisabilité pratique, un prototype a été fabriqué et testé expérimentalement. Les mesures des paramètres S ont été effectuées à l'aide d'un analyseur de réseau vectoriel (VNA), tandis que les caractéris-

tiques de rayonnement — incluant les fronts de phase, les amplitudes et les diagrammes en champ lointain — ont été évaluées en chambre anéchoïque. Les résultats expérimentaux sont en bon accord avec les simulations, démontrant la capacité de l'antenne à prendre en charge la commutation de mode OAM à la fois dans les bandes micro-ondes et millimétriques.

Ainsi, ce travail établit une base solide pour le développement futur d'antennes OAM multi-bandes à commutation de mode, contribuant au développement de systèmes de communication sans fil à haute capacité et à efficacité spectrale optimisée.

Mots-clés: antenne double bande, intégration micro-ondes et ondes millimétriques, moment angulaire orbital (OAM), réseau circulaire uniforme (UCA).

Abstract

With the rapid advancement of wireless communication technology, especially with the development of 5G and beyond, the demand for high-capacity transmission and enhanced spectral efficiency has significantly increased. The integration of microwave and millimeter-wave (mm-wave) frequency bands is essential for next-generation communication systems, enabling high-speed data transmission and enhanced network performance. Antennas capable of generating orbital angular momentum (OAM) modes have attracted significant attention due to their ability to improve spectral efficiency and increase data transmission capacity by utilizing orthogonal spatial wave modes. However, conventional multi-band antenna designs, including those operating at both microwave and mm-wave frequencies, often struggle to effectively support multi-band operation while maintaining compatibility with OAM modes. Therefore, the design of antennas that not only support OAM modes but also operate efficiently across multiple frequency bands is of great research interest, as they have the potential to enhance the capacity of the wireless system and spectral efficiency.

To address these challenges, this thesis presents the design, optimization, fabrication, and experimental validation of a mode-switchable dual-band OAM antenna capable of operating at 5.8 and 28 GHz. The proposed antenna system comprises two uniform circular arrays (UCAs), each utilizing a dual-port feeding configuration. By selectively exciting one port while terminating the other with a 50 Ω matched load, stable and efficient generation of OAM modes with topological charges of $l = \pm 1$ is achieved. This configuration enables dual-band OAM mode switching without the need for external phase-shifting networks. The simplified dual-port scheme not only facilitates mode switching but also allows the operating frequency to be flexibly adjusted by scaling the antenna's physical dimensions. This demonstrates the scalability of the proposed design and its potential to be adapted for various frequency bands. Overall, the proposed approach addresses the limitations of conventional multi-band OAM antennas and demonstrates the feasibility of integrating OAM functionality into next-generation wireless communication systems.

To verify the effectiveness of the proposed antenna, extensive numerical simulations were conducted in CST Microwave Studio to analyze key performance metrics, including S-parameters, phase wavefronts, amplitude, and far-field radiation patterns. The simulation results confirm that the antenna achieves stable OAM mode generation across both frequency bands. To further validate the practical feasibility of the design, a prototype was fabricated and experimentally tested. Measurements of S-parameters were conducted using a vector network analyzer (VNA), while radiation characteristics—including phase wavefronts, amplitude, and far-field patterns—were evaluated in an anechoic chamber. The experimental

results exhibit good agreement with simulations, demonstrating the antenna's capability to support OAM mode switching in both microwave and mm-wave bands.

Therefore, this research provides a foundation for future advancements in mode-switchable, multi-band OAM antenna design, contributing to the development of high-capacity, spectrum-efficient wireless communication systems.

Keywords: dual-band antenna, microwave and millimeter-wave integration, orbital angular momentum (OAM), uniform circular array (UCA).

Chapter 0

SOMMAIRE RÉCAPITULATIF

0.1 Titre de la Thèse en Français

Conception et analyse d'une antenne OAM à double bande et à modes commutables pour les systèmes intégrés micro-ondes et millimétriques

0.2 Introduction

0.2.1 Contexte et motivation

Avec le développement rapide des technologies de communication sans fil, porté par des applications émergentes telles que l'Internet des objets (IoT), les systèmes de transport intelligents, ainsi que la 5G et les générations futures, les exigences en matière de capacité élevée, de faible latence et d'efficacité spectrale se sont considérablement accrues. Les systèmes de communication à base de micro-ondes ont été largement adoptés en raison de leur infrastructure mature, de leur transmission fiable et de leur large couverture. Toutefois, le spectre limité dans les bandes micro-ondes conventionnelles entraîne une forte congestion, limitant leur capacité à répondre à la croissance du nombre d'appareils connectés et aux besoins élevés en débit des réseaux de nouvelle génération [1–7].

Pour remédier à cette limitation, la technologie des ondes millimétriques (mm-wave) a suscité un intérêt croissant grâce à ses larges ressources spectrales, ses débits ultra-élevés et sa faible latence [1–3, 8]. Bien qu'elle soit considérée comme une technologie centrale pour la 5G et au-delà, la propagation des signaux mm-wave souffre de pertes importantes, d'une faible pénétration dans les obstacles et d'une portée limitée, rendant leur déploiement autonome peu pratique à grande échelle [9–15].

Il est donc peu probable que la technologie mm-wave remplace entièrement les systèmes micro-ondes à court terme. Compte tenu de la complémentarité de ces deux bandes, leur

intégration est devenue un pilier fondamental des systèmes de communication sans fil de prochaine génération [15, 16]. Dans ce contexte, les antennes multibandes jouent un rôle essentiel, en permettant une exploitation flexible des différentes bandes de fréquences afin d'améliorer la couverture, la fiabilité des communications et l'utilisation du spectre [17–23]. Il devient donc crucial de concevoir des structures d'antennes compactes, commutables en mode, capables de fonctionner à la fois dans les bandes micro-ondes et mm-wave, afin de soutenir les avancées vers la 5G et au-delà [1, 2, 9, 10, 16, 24–34].

La demande croissante en débits élevés et en capacité réseau a conduit à des recherches intensives sur l'amélioration de la capacité et de l'efficacité spectrale. Traditionnellement, ces efforts se sont concentrés sur l'élargissement de la bande passante (BW) et l'augmentation du rapport signal sur bruit (SNR). Selon le théorème de Shannon, la capacité théorique du canal est donnée par $C = B\log_2(1 + \mathrm{SNR})$. Néanmoins, dans la pratique, l'augmentation de la BW est souvent limitée par des compromis entre gain et bande, ou par des contraintes sur le rapport d'ondes axial, tandis que le SNR peut être fortement dégradé par les interférences, les trajets multiples ou le bruit du système [35–39].

Face à ces limites, de nouvelles approches ont été explorées pour améliorer l'efficacité spectrale sans se reposer uniquement sur l'augmentation de la BW ou du SNR. Parmi elles, le multiplexage spatial permet de transmettre plusieurs flux de données sur une même fréquence en exploitant la diversité spatiale [40]. Une approche particulièrement prometteuse est le multiplexage par division de modes, fondé sur l'utilisation du moment cinétique orbital (OAM). Contrairement aux schémas classiques basés sur la fréquence ou la polarisation, les antennes OAM utilisent l'orthogonalité des charges topologiques pour générer des canaux spatiaux indépendants. Les faisceaux OAM sont caractérisés par un front d'onde hélicoïdal dont la phase azimutale est décrite par $\exp(-jl\phi)$, où l est l'indice du mode OAM. Grâce à cette orthogonalité, plusieurs canaux indépendants peuvent coexister sur la même fréquence sans consommation supplémentaire de spectre [41–44].

Depuis la première démonstration expérimentale d'une transmission OAM radio en 2012 [45], de nombreuses recherches ont été menées pour développer des antennes OAM efficaces destinées aux systèmes à haute capacité [46–49]. Outre leurs avantages en matière d'efficacité spectrale, les antennes OAM sont de plus en plus considérées pour une intégration dans des systèmes bi-bandes micro-ondes/mm-wave, permettant une commutation dynamique des modes et répondant ainsi aux défis de congestion fréquentielle et d'augmentation de capacité dans les réseaux futurs [48, 50–53].

Des stratégies de conception d'antennes multibandes ont été proposées, telles que l'approche par empilement [54–56] et celle à couche unique [57–59]. Parallèlement, diverses méthodes de génération d'ondes OAM ont été explorées, comme les réseaux circulaires uniformes (UCA) [60–69], les réflecteurs paraboliques spirales [45, 70–72], les antennes patch à polarisation circulaire [73–78], les antennes annulaires à ondes progressives [49, 79–82], les métasurfaces ou réflecteurs plans [50, 52, 83–90], ainsi que les antennes à résonateur diélectrique (DRA) [91–93]. Toutefois, la génération d'ondes OAM commutables sur plusieurs bandes reste un défi majeur, principalement en raison de la complexité des structures d'alimentation, du besoin de contrôle précis de la phase, d'un isolement insuffisant entre les bandes, et des contraintes d'intégration physique.

Pour répondre à ces limitations, cette thèse propose une antenne OAM compacte et bi-bande, dotée d'un mécanisme de commutation basé sur une excitation symétrique à double port. La conception permet une génération stable des modes $l = \pm 1$ aux fréquences de 5.8 et 28 GHz, sans recours à des circuits externes de déphasage. Une étude complète incluant la conception, la simulation, la fabrication et la validation expérimentale est présentée.

0.2.2 État de la recherche

0.2.2.1 Stratégies de conception pour les antennes multibandes et intégrées micro-ondes / ondes millimétriques

Aux premières étapes du développement des antennes bi-bandes ou multibandes, l'approche la plus courante consistait à placer côte à côte deux antennes indépendantes, chacune fonctionnant dans une bande de fréquence distincte [94–96]. Cependant, cette méthode entraînait généralement des dimensions globales importantes et une faible efficacité d'ouverture, limitant ainsi son adéquation aux systèmes compacts ou intégrés.

Pour surmonter ces limitations, le concept d'antenne à ouverture partagée a été introduit et est depuis considéré comme une solution prometteuse [54–56, 58, 59, 97–103]. En intégrant plusieurs structures rayonnantes — chacune conçue pour une bande de fréquence spécifique — au sein d'une topologie unifiée, les systèmes d'antennes à ouverture partagée offrent des avantages notables, notamment une réduction de la taille globale, un poids système plus faible et une meilleure efficacité d'ouverture [104].

0.2.2.2 Vue d'ensemble des architectures d'antennes OAM

Depuis les travaux pionniers de L. Allen et al. en 1992, qui ont analysé de manière systématique le moment cinétique orbital (OAM) transporté par les ondes lumineuses et mis en évidence sa correspondance avec la structure de phase hélicoïdale $\exp(-jl\phi)$ des modes de Laguerre–Gauss (LG) [105], cette propriété a suscité un intérêt considérable. L'OAM est aujourd'hui reconnu comme un mécanisme physique essentiel offrant un degré de liberté supplémentaire pour le multiplexage, avec le potentiel d'accroître la capacité des systèmes de communication sans fil. L'une des caractéristiques les plus distinctives des faisceaux OAM réside dans leurs fronts d'onde hélicoïdaux, qui font « tourner » le faisceau pendant la propagation. Ces faisceaux présentent une singularité de phase au centre du front d'onde, d'où résulte une amplitude nulle le long de l'axe de propagation. L'intensité adopte ainsi un profil annulaire ou « en beignet », marque caractéristique des modes porteurs d'OAM. Les différents modes OAM sont mutuellement orthogonaux et la charge topologique l peut, en principe, prendre un nombre infini de valeurs discrètes ; il est donc théoriquement possible de transmettre un nombre illimité de canaux de données indépendants sur une même fréquence porteuse [42, 106–108].

À la suite de cette découverte initiale, la recherche sur les faisceaux OAM s'est fortement développée [109–117]. Bien que les premières études aient principalement concerné le

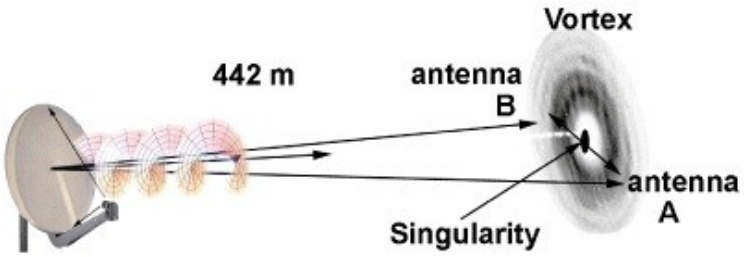

Figure 1: Expérimentation d'un lien OAM à 2.4 GHz sur 442 m: antenne parabolique émettrice et deux antennes Yagi réceptrices [45].

domaine optique, il est reconnu que les ondes optiques et radio sont toutes deux des ondes électromagnétiques, se distinguant principalement par leurs plages de fréquences. Cette similitude fondamentale confère donc à l'OAM un fort potentiel dans le domaine radio-fréquence (RF). En conséquence, la section suivante passe en revue les avancées récentes relatives aux faisceaux OAM dans les domaines RF.

0.2.2.3 Avancées récentes des faisceaux OAM dans les domaines RF

Depuis la démonstration pionnière de Thidé et al. en 2007, qui ont proposé pour la première fois l'application de l'OAM aux communications sans fil [118], de nombreuses recherches ont été menées aussi bien sur le plan théorique que pratique. Notamment, Tamburini et al. ont réalisé en 2012 le premier lien de communication OAM véritablement fonctionnel à 2.4 GHz: en utilisant une antenne parabolique comme émetteur et des antennes Yagi comme récepteurs, ils ont obtenu un multiplexage bi-mode sur une distance de 442 m (Fig. 1) [45].

Les progrès se sont ensuite rapidement étendus aux fréquences millimétriques. En 2013, Mahmouli et al. ont employé des plaques holographiques (HP) ou des plaques à phase spiralée (SPP) pour générer des faisceaux OAM à 60 GHz, transmettant avec succès une vidéo non compressée de 4 Gbps sur une courte distance (Fig. 2) [119]. En 2014, Yan et al. ont démontré un lien à 28 GHz combinant quatre modes OAM et deux polarisations orthogonales, atteignant un débit de 32 Gbps et une efficacité spectrale d'environ 16 bit/s/Hz sur 2.5 m [48]. En 2015, Hui et al. ont exploré la bande 60 GHz à l'aide d'antennes à ondes progressives annulaires, transmettant les modes $l = \pm 3$ avec succès pour des signaux d'image et de forme carrée [49]. À des fréquences RF plus basses, Chen et al. ont généré en 2016 un faisceau OAM de mode $l = 2$ avec une antenne patch elliptique à 2 GHz, démontrant la transmission d'images [78].

Des avancées industrielles notables proviennent de la société NTT. En 2018, Sasaki et al. ont proposé un système OAM-MIMO à 28 GHz basé sur des UCAs multi-anneaux, atteignant un débit remarquable de 100 Gbps à 10 m grâce au multiplexage de plusieurs faisceaux OAM générés sur le même anneau, puis démultiplexés par des algorithmes MIMO avancés [120]. En 2021, NTT a doublé le débit à 200 Gbps en introduisant le multiplexage de polarisation [121].

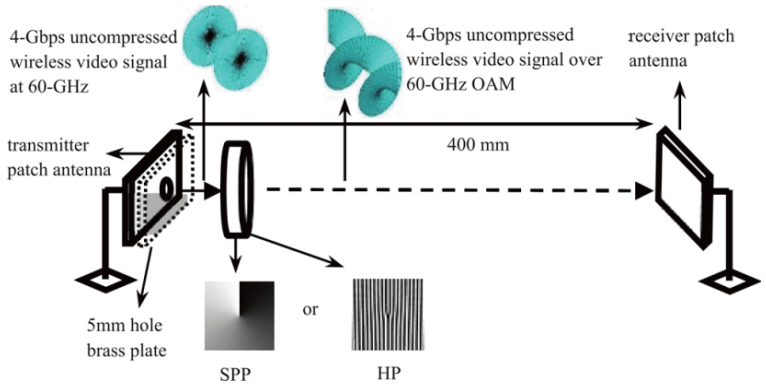

Figure 2: Montage expérimental de Mahmouli et al.: transmission d'un faisceau OAM à 60 GHz au moyen d'une HP ou d'une SPP, transportant une vidéo non compressée de 4 Gbps sur 400 mm [119].

La même année, l'équipe a étendu ses travaux à l'extérieur : un lien OAM à 40 GHz a permis de transmettre 117 Gbps sur 200 m [122]. Ces démonstrations industrielles ont suscité un fort intérêt académique et industriel, établissant les bases des futures technologies OAM dans les réseaux sans fil de nouvelle génération.

Au-delà des communications, la modulation OAM trouve aussi des applications prometteuses en imagerie radar. Liu et al., en 2014, ont introduit une méthodologie d'imagerie radar modulée par OAM qui améliore la résolution angulaire du système [123].

0.2.3 Objectifs de recherche et innovations

0.2.3.1 Objectifs de recherche

Cette thèse porte sur la conception, la simulation et la validation expérimentale d'une antenne OAM bi-bande à capacité de commutation de mode, destinée à des systèmes de communication sans fil intégrant les bandes micro-ondes et ondes millimétriques. L'antenne proposée fonctionne à 5.8 et 28 GHz et adopte une structure à ouverture partagée sur une même couche afin d'offrir de hautes performances bi-bandes dans un format compact. La commutation de mode est assurée par une alimentation symétrique à double port, permettant de basculer entre les modes conjugués ($l = \pm 1$) sans recourir à des circuits externes de déphasage. Les tâches de recherche spécifiques sont les suivantes:

- Analyser les caractéristiques fondamentales des faisceaux OAM, notamment leurs propriétés physiques, leur orthogonalité et leurs mécanismes de génération;
- Passer en revue les avancées récentes en matière de conceptions d'antennes OAM multi-bandes et de stratégies d'intégration;
- Proposer une nouvelle antenne bi-bande basée sur un réseau circulaire uniforme (UCA) coplanaire, capable de fonctionner simultanément à 5.8 et 28 GHz;
- Réaliser une radiation OAM commutable en mode grâce à un schéma d'alimentation symétrique à double port, sans circuits externes de déphasage;

- Valider les performances de l'antenne par des simulations électromagnétiques complètes et des mesures expérimentales, incluant les paramètres S, les distributions en champ proche et les diagrammes de rayonnement en champ lointain.

0.2.3.2 Principales innovations

Les principales contributions et innovations de cette thèse se résument comme suit:

- **Structure d'antenne OAM bi-bande à ouverture partagée sur une même couche:** les deux réseaux circulaires uniformes (UCA) pour 5.8 et 28 GHz sont implantés sur un même plan, permettant une intégration compacte et une réutilisation efficace de l'ouverture;
- **Commutation des modes OAM conjugués sans circuits externes de déphasage:** un mécanisme d'alimentation symétrique à double port permet de basculer efficacement entre les modes $l = +1$ et $l = -1$ par simple sélection de port;
- **Isolation élevée entre les ports garantissant un fonctionnement indépendant:** la conception assure une isolation inter-port supérieure à 30 dB, offrant une génération OAM bi-bande stable et sans interférences;
- **Validation complète de bout en bout:** l'ensemble du cycle de conception est réalisé — analyse théorique, modélisation, fabrication du prototype — puis validé expérimentalement par mesures des paramètres S, cartographie en champ proche et caractérisation du rayonnement en champ lointain.

0.3 Fondements théoriques

0.3.1 Aperçu du moment cinétique orbital

En théorie électromagnétique classique, les ondes électromagnétiques transportent non seulement une quantité de mouvement linéaire, mais également un *moment cinétique total*. Celui-ci peut être décomposé en un *moment cinétique de spin* (SAM), associé à l'état de polarisation, et en un *moment cinétique orbital* (OAM), lié à la structure spatiale du front d'onde [106, 124, 125].

Le moment cinétique total du champ électromagnétique s'écrit [126]:

$$\vec{J} = \int \varepsilon_0 \, \vec{r} \times \mathrm{Re}\Big\{ \vec{E} \times \vec{B}^* \Big\} \, dV, \tag{1}$$

expression dérivée du vecteur de Poynting moyenné dans le temps qui représente la densité de moment cinétique total. Ici, ε_0 est la permittivité du vide, $\vec{r}$ le vecteur position, et $\vec{E}$ et

$\vec{B}$ les champs électrique et magnétique. On décompose classiquement [127]:

$$\vec{J} = \vec{L} + \vec{S}, \tag{2}$$

où $\vec{L}$ est le moment orbital et $\vec{S}$ le moment de spin.

Dans une formulation invariant-de-jauge de l'électrodynamique classique, les densités de $\vec{L}$ et $\vec{S}$ s'expriment via le potentiel vecteur magnétique $\vec{A}$:

$$\vec{L} = \varepsilon_0 \int \mathrm{Re}\Big\{ j\, \vec{E}^* \, (\hat{\vec{L}} \cdot \vec{A}) \Big\}\, dV, \tag{3}$$

$$\vec{S} = \varepsilon_0 \int \mathrm{Re}\Big\{ \vec{E}^* \times \vec{A} \Big\}\, dV, \tag{4}$$

avec $\hat{\vec{L}} = -j(\vec{r} \times \nabla)$, opérateur OAM [128]. L'OAM $\vec{L}$ dépend donc de la distribution spatiale du champ et de la structure hélicoïdale du front d'onde; il est quantifié par la *charge topologique* l: $l < 0$ pour une hélice antihoraire et $l > 0$ pour une hélice horaire. À l'inverse, le SAM $\vec{S}$ dépend uniquement de la polarisation: $s = 0$ pour une onde polarisée linéairement, $s = 1$ pour LHCP et $s = -1$ pour RHCP [129, 130].

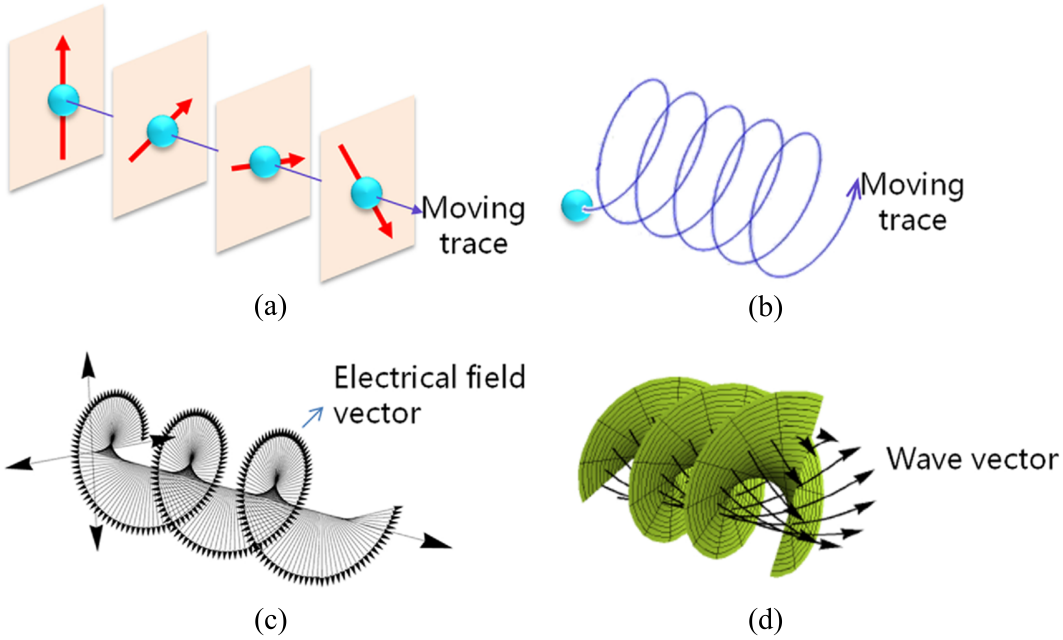

Figure 3: Illustrations conceptuelles du moment cinétique: (a) un objet tournant sur son propre axe (SAM); (b) un objet en orbite autour d'un axe externe (OAM); (c) un faisceau polarisé circulairement portant un SAM via la rotation du champ électrique; (d) un front d'onde hélicoïdal représentant l'OAM [107,131].

Pour clarifier la différence physique entre spin et moment orbital, la Fig. 3 présente ces schémas conceptuels [107, 131]. Les fronts d'onde hélicoïdaux des faisceaux OAM sont décrits par la phase $\exp(-jl\phi)$, où ϕ est l'angle azimutal et l la charge topologique [107, 130].

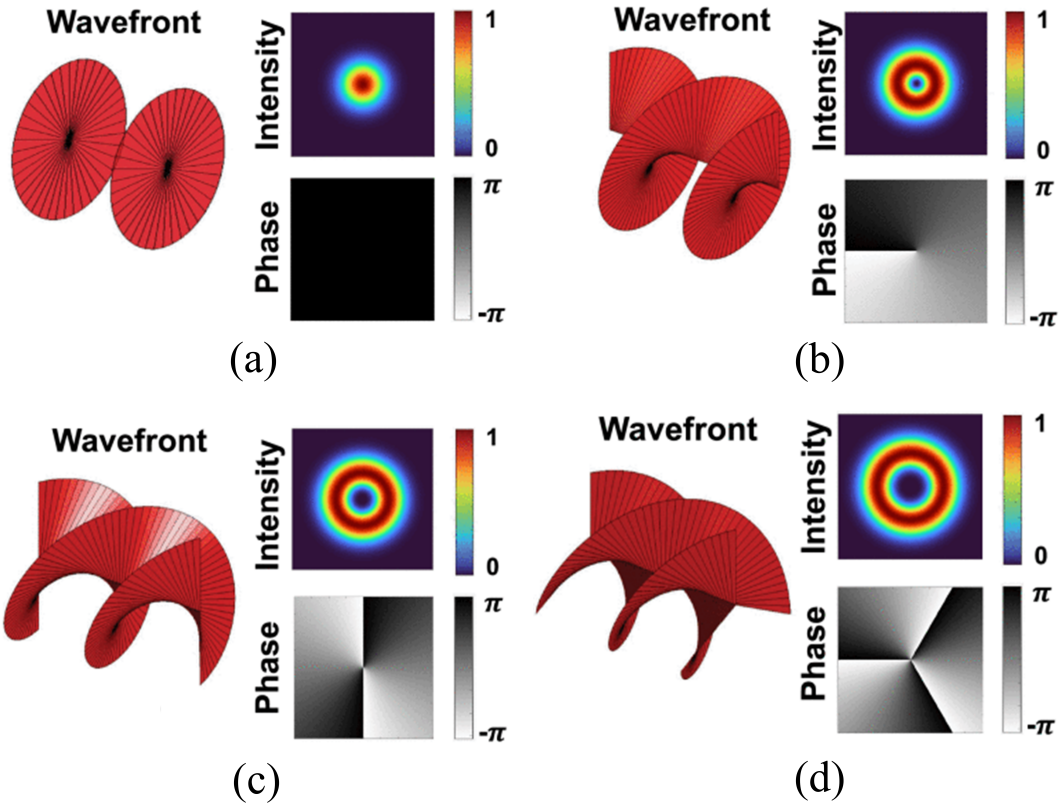

Figure 4: Fronts d'onde, intensité et distribution de phase pour les charges $l = 0, 1, 2, 3$: (a) $l = 0$; (b) $l = 1$; (c) $l = 2$; (d) $l = 3$ [132].

La Fig. 4 [132] illustre plus concrètement cette dépendance: plus l augmente, plus le front d'onde se torsade et le profil d'intensité passe d'une distribution gaussienne à une couronne annulaire avec un creux central:

(a) $l = 0$: front plan, phase uniforme, intensité gaussienne;

(b) $l = 1$: une rotation 2π; intensité en « beignet »;

(c) $l = 2$: deux rotations 2π; anneau radial élargi;

(d) $l = 3$: trois rotations 2π; couronne encore plus large et vortex de phase.

0.3.2 Orthogonalité des modes OAM

L'un des principaux atouts des ondes électromagnétiques transportant de l'OAM réside dans l'orthogonalité intrinsèque des différentes charges topologiques dans le domaine azimutal. Pour un réseau circulaire uniforme (UCA), le champ électrique complexe du mode OAM d'ordre l en coordonnées cylindriques (ρ, ϕ, z) s'écrit [80]:

$$E_l(\rho, \phi, z) = A_l(\rho, z)\, e^{-jl\phi}, \tag{5}$$

où $A_l(\rho, z)$ représente l'enveloppe d'amplitude sur le plan transverse, tandis que le facteur $\exp(-jl\phi)$ correspond à une phase hélicoïdale d'ordre l [80, 118, 126].

Sur un plan transverse donné, défini par ρ et z, deux modes quelconques l_1 et l_2 vérifient la condition d'orthogonalité suivante [80]:

$$\int_0^{2\pi} E_{l_1}(\rho, \phi, z)\, E_{l_2}^*(\rho, \phi, z)\, \mathrm{d}\phi = 0, \quad l_1 \neq l_2, \tag{6}$$

ce qui signifie qu'à la réception chaque mode OAM peut être considéré comme un canal de communication indépendant, sans nécessiter d'égalisation numérique complexe [80].

Cette « orthogonalité physique » intrinsèque contraste avec les techniques MIMO en visibilité directe (LOS-MIMO), qui reposent sur l'espacement des antennes et l'inversion de matrices pour découpler les canaux. Le multiplexage fondé sur l'OAM permet ainsi une suppression naturelle des interférences et réduit significativement la complexité du récepteur [80].

0.3.3 Mécanisme de génération des faisceaux OAM basé sur un UCA

En s'appuyant sur les notions de spin et de moment cinétique orbital introduites à la section 0.3.1, cette partie établit le cadre théorique de la génération de faisceaux OAM à l'aide d'un réseau circulaire uniforme (UCA). De telles configurations sont largement utilisées en conception d'antennes en raison de leur symétrie de rotation, de la simplicité de leur analyse et de leur capacité à fournir un contrôle discret de la phase azimutale, fondement du principe de fonctionnement de l'antenne proposée.

Considérons un UCA idéal composé de N éléments isotropes, uniformément répartis sur un anneau de rayon a dans le plan xy, comme illustré Fig. 5. La position angulaire du n-ième élément est

$$\phi_n = \frac{2\pi(n-1)}{N}, \qquad n = 1, 2, \ldots, N \tag{7}$$

Un point d'observation $Q(r, \theta, \phi)$ est défini en champ lointain via les coordonnées sphériques. Les vecteurs position du n-ième élément et de Q sont respectivement $\vec{r}_n$ et $\vec{r}$. Le vecteur allant de l'élément n vers Q est donc

$$\vec{R}_n = \vec{r} - \vec{r}_n \tag{8}$$

Sous l'hypothèse de champ lointain ($r \gg a$), la distance R_n se linéarise par un développement de Taylor au premier ordre:

$$R_n \approx r - a \sin\theta \cos(\phi - \phi_n) \tag{9}$$

Le courant d'excitation de chaque élément, exprimé sous forme phasorielle [133], est

$$I_n = I e^{j[\phi_0 + (n-1)\Delta\phi]} \tag{10}$$

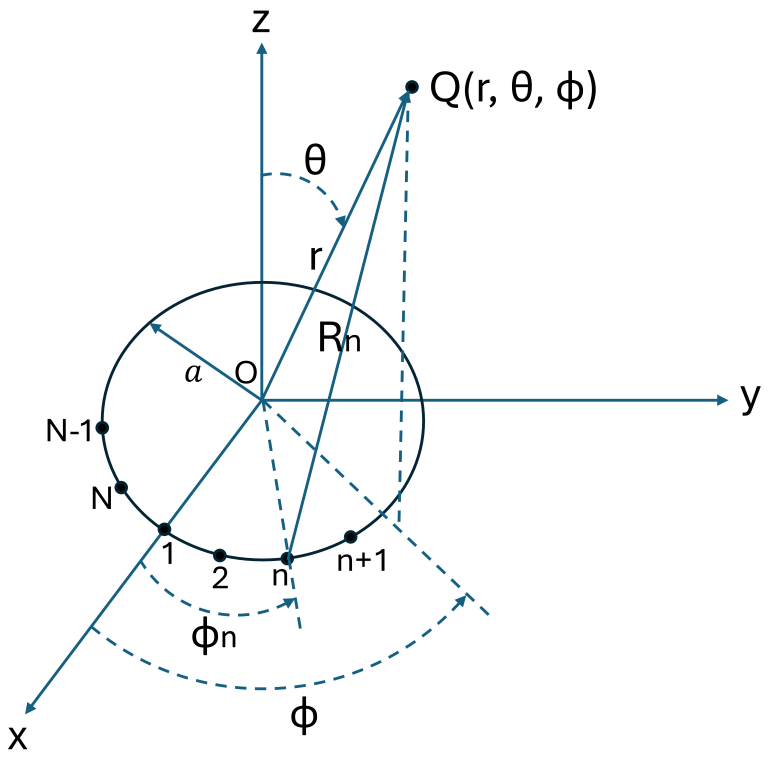

Figure 5: Géométrie d'un réseau circulaire uniforme à N éléments.

où $\Delta\phi = \frac{2\pi l}{N}$ est le déphasage progressif entre éléments, l l'indice de mode OAM (ou charge topologique), ϕ_0 la phase initiale, et I l'amplitude constante du courant. Dans un UCA pratique, le nombre de modes réalisables est limité à $|l| < N/2$ [118, 126].

Le champ électrique total en champ lointain au point Q est la superposition des contributions de tous les éléments [134]:

$$\vec{E} = \sum_{n=1}^{N} I_n \frac{e^{-jkR_n}}{R_n} \hat{a}_r \tag{11}$$

$\hat{a}_r$ désignant le vecteur unitaire radial.

En substituant R_n et I_n puis en appliquant l'approximation de champ lointain, on obtient

$$\vec{E} \approx \frac{Ie^{-jkr}}{r} \sum_{n=1}^{N} e^{j[ka\sin\theta\cos(\phi-\phi_n)+\phi_0+(n-1)\Delta\phi]} \hat{a}_r \tag{12}$$

Cette expression montre que le rayonnement résultant possède un front de phase hélicoïdal dans la direction azimutale, signature d'un faisceau OAM: le déphasage total sur la circonférence du réseau est $2\pi l$, et le pas de phase entre éléments est $\Delta\phi$.

Le signe de l indique la main du front d'onde : une rotation horaire correspond à $l > 0$, une rotation antihoraire à $l < 0$. Cette variation de phase engendre le profil d'intensité en « beignet » et la singularité de phase centrale, caractéristiques des modes OAM [129, 130, 132].

0.3.3.1 Réalisation des modes conjugués par alimentation symétrique à double port

Afin de renforcer la faisabilité pratique, ce travail adopte une architecture d'alimentation symétrique à deux ports permettant la commutation entre les modes $l = +1$ et $l = -1$, sans recourir à des réseaux externes de déphasage encombrants.

En posant $\phi_0 = 0$ dans l'équation (10), le courant d'excitation se simplifie en:

$$I_n^{(l)} = I_0 \, \mathrm{e}^{j(n-1)\Delta\phi}, \tag{13}$$

où I_0 représente l'amplitude constante du courant.

Pour $l = +1$ et $l = -1$, les courants d'excitation vérifient:

$$I_n^{(-1)} = \left(I_n^{(+1)}\right)^* \tag{14}$$

Cette relation de conjugaison complexe permet la commutation de modes OAM grâce à la symétrie d'alimentation : en excitant sélectivement un port et en chargeant l'autre par une impédance adaptée, on génère les modes OAM conjugués sans nécessiter de circuits supplémentaires de déphasage. Cette approche simplifie considérablement l'architecture tout en assurant une génération stable et reconfigurable des faisceaux OAM sur deux bandes de fréquences.

0.4 Conception et évaluation des performances de l'antenne OAM proposée

Afin de répondre à la demande croissante en systèmes de communication sans fil à haute capacité et multi-services, ce travail présente la conception et l'évaluation d'une antenne compacte, à une seule couche, capable de générer des faisceaux à moment angulaire orbital (OAM) sur deux bandes de fréquence distinctes: 5.8 et 28 GHz. Cette antenne permet une couverture simultanée des bandes micro-ondes et millimétriques au sein d'une structure à ouverture partagée.

La structure proposée repose sur deux réseaux circulaires uniformes (UCAs) concentriques, chacun composé de huit patches elliptiques alimentés en série et conçus pour leur bande respective. Le basculement de mode entre $l = +1$ et $l = -1$ est obtenu grâce à une excitation symétrique à double port, sans recours à des circuits de déphasage externes, ce qui réduit la complexité et améliore l'intégration.

La conception a été réalisée sur un substrat RO4350B (épaisseur 0.508 mm, $\varepsilon_r = 3.48$), assurant de faibles pertes sur les deux bandes. La Fig. 6 illustre la disposition géométrique des deux réseaux UCA et l'emplacement des ports d'alimentation. La Table 1 résume les principaux paramètres géométriques, où les indices i et o désignent respectivement les réseaux UCA intérieur et extérieur. Les dimensions ont été soigneusement optimisées par des simulations

Table 1: Paramètres géométriques de l'antenne proposée (unité : mm)

Paramètre	R_{o1}	F_{o1}	P_{o1}	L_{o2}	G_{o1}	A_{o1}	L_{o1}	R_{o3}	R_{o2}
Valeur	27.2	0.6	0.63	5	1.1	110°	12.63	9	17
Paramètre	R_{i1}	F_{i1}	P_{i1}	L_{i2}	G_{i1}	A_{i1}	L_{i1}	R_{i3}	R_{i2}
Valeur	7.73	0.2	0.3	1.9	1	100°	4.79	2.4	3.4

Remarque : R_{o3} et R_{o2} représentent respectivement le petit et le grand diamètre de l'élément elliptique dans l'UCA externe.

en champ complet afin d'assurer une bonne adaptation d'impédance, une faible diaphonie et une génération fiable des modes OAM.

Les résultats expérimentaux et simulés confirment une bonne adaptation d'impédance (taux de réflexion $<$ –10 dB), une isolation inter-port $>$ 30 dB, ainsi que la génération de faisceaux OAM stables sur les deux bandes. Des distributions caractéristiques de phase hélicoïdale et de profils d'amplitude annulaires ont été observées en champ proche, tandis que les diagrammes en champ lointain valident la présence de nœuds axiaux. Ces performances font de cette antenne une solution prometteuse pour les systèmes sans fil intégrés micro-ondes et ondes millimétriques de prochaine génération.

0.5 Conclusion et perspectives

0.5.1 Synthèse des travaux

Cette thèse a présenté la conception, la simulation et la validation expérimentale d'une antenne OAM bi-bande à commutation de mode, fonctionnant à 5.8 et 28 GHz. L'antenne proposée adopte une architecture à ouverture partagée sur une même couche et utilise une alimentation symétrique à double port pour commuter entre les modes conjugués $l = \pm 1$ sans nécessiter de réseaux externes de déphasage.

Les principales contributions peuvent être résumées comme suit:

- Proposition d'un double réseau circulaire uniforme (UCA) capable de générer des faisceaux OAM commutables sur deux bandes de fréquences grâce à une structure coplanaire compacte;
- Mise en œuvre d'une stratégie d'alimentation symétrique permettant la commutation entre les modes OAM conjugués, assurant une simplicité structurelle et une isolation inter-port élevée (>30 dB) ;
- Validation numérique et expérimentale complète — paramètres S, distributions d'amplitude et de phase en champ proche, diagrammes de gain en champ lointain — confirmant la capacité de l'antenne à générer des faisceaux OAM bi-bandes;

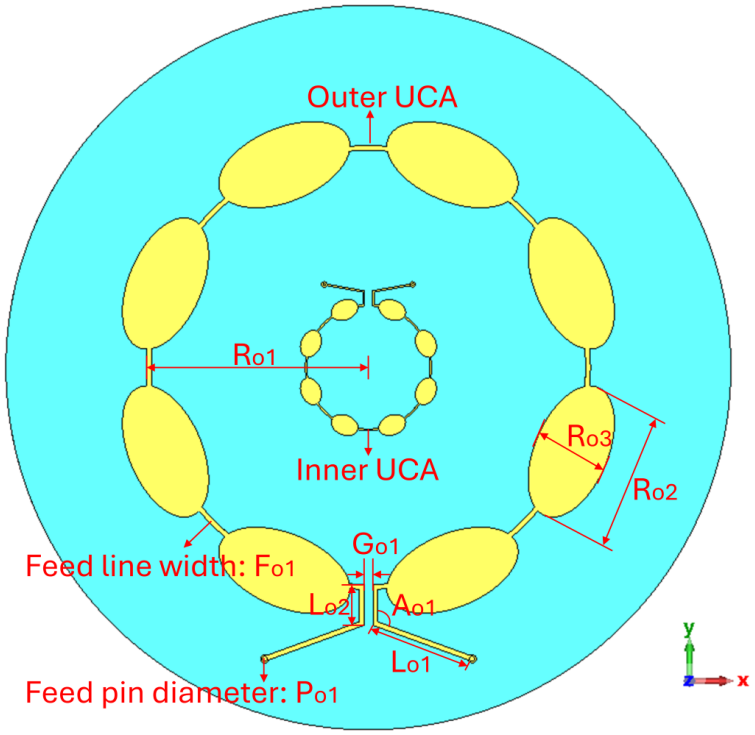

(a)

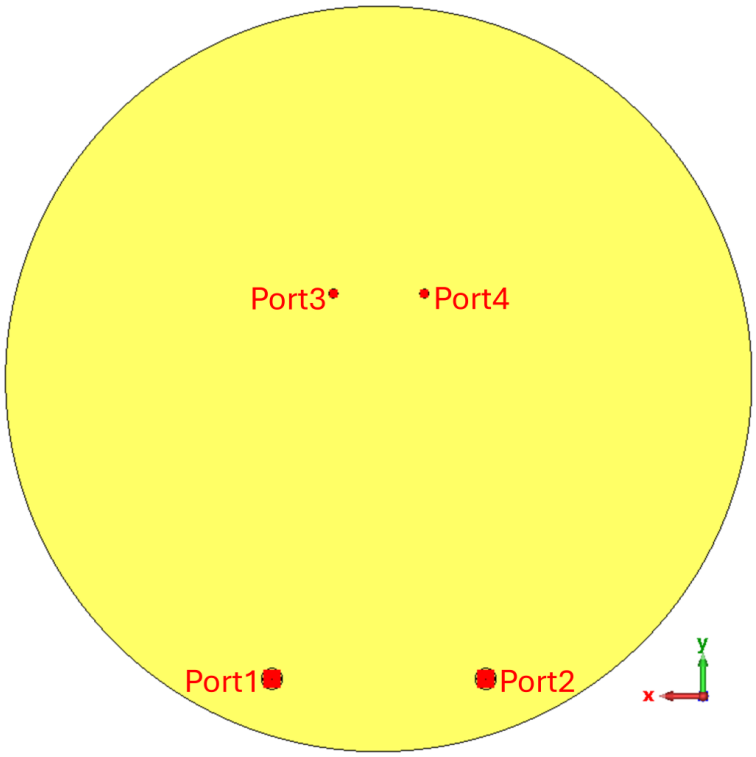

(b)

Figure 6: Disposition de l'antenne : (a) Vue de dessus montrant les deux réseaux UCA ; (b) Vue de dessous avec les quatre ports d'alimentation.

- Introduction d'une solution d'antenne OAM bi-bande et commutable en mode pour les futurs systèmes de communication micro-ondes et millimétriques, favorisant une utilisation spectrale efficace et une diversité de modes.

0.5.2 Perspectives

Bien que la conception présentée affiche des performances prometteuses, plusieurs axes de recherche peuvent être poursuivis:

- **Modes OAM d'ordre supérieur :** explorer la génération et la reconfiguration de modes $l = \pm 2$, ± 3, etc., afin d'accroître encore les capacités de multiplexage spatial;
- **Systèmes hybrides OAM–MIMO :** combiner l'OAM avec des architectures MIMO pour permettre une réutilisation tridimensionnelle du spectre (fréquence, espace, mode) et améliorer la capacité globale du système;
- **Intégration système et déploiements réels :** adapter l'antenne à des scénarios pratiques — réseaux véhiculaires, couverture intérieure, IoT — nécessitera des recherches supplémentaires sur l'optimisation structurelle, l'encapsulation et la robustesse environnementale.

En conclusion, les antennes basées sur l'OAM offrent un potentiel considérable pour les systèmes de communication sans fil à haute capacité de prochaine génération. L'approche proposée dans cette thèse constitue une solution compacte et pratique pour une mise en œuvre OAM bi-bande et établit une base solide pour des avancées futures vers des architectures de communication plus complexes et intégrées.

Contents

Acknowledgments **iii**

Résumé **v**

Abstract **vii**

0 SOMMAIRE RÉCAPITULATIF **ix**
0.1 Titre de la Thèse en Français ix
0.2 Introduction ix
0.2.1 Contexte et motivation ix
0.2.2 État de la recherche xi
0.2.2.1 Stratégies de conception pour les antennes multibandes et intégrées micro-ondes / ondes millimétriques xi
0.2.2.2 Vue d'ensemble des architectures d'antennes OAM xi
0.2.2.3 Avancées récentes des faisceaux OAM dans les domaines RF xii
0.2.3 Objectifs de recherche et innovations xiii
0.2.3.1 Objectifs de recherche xiii
0.2.3.2 Principales innovations xiv
0.3 Fondements théoriques xiv
0.3.1 Aperçu du moment cinétique orbital xiv
0.3.2 Orthogonalité des modes OAM xvi
0.3.3 Mécanisme de génération des faisceaux OAM basé sur un UCA . . . xvii
0.3.3.1 Réalisation des modes conjugués par alimentation symétrique à double port xix
0.4 Conception et évaluation des performances de l'antenne OAM proposée . . . xix
0.5 Conclusion et perspectives xx
0.5.1 Synthèse des travaux xx
0.5.2 Perspectives xxii

Contents **xxiii**

List of Figures **xxv**

List of Abbreviations **xxvii**

1 Introduction **1**
1.1 Background and Motivation 1

1.2 Research Status . . . 3
1.2.1 Design Strategies for Multi-Band and Integrated Microwave and Mm-Wave Antennas . . . 3
1.2.1.1 Stacked Design Approach . . . 4
1.2.1.2 Same-Layer Design Approach . . . 7
1.2.2 Overview of OAM Antenna Architectures and Generation Techniques 11
1.2.2.1 Recent Advances of OAM beams in RF Domains . . . 11
1.2.2.2 Generation Methods of OAM Beams in RF Domains . . . 13
1.3 Research Objectives, Innovations, and Thesis Structure . . . 19
1.3.1 Research Objectives . . . 19
1.3.2 Key Innovations . . . 20
1.3.3 Thesis Structure . . . 20

2 Theoretical Background 23
2.1 Overview of Orbital Angular Momentum . . . 23
2.2 Mode Orthogonality of OAM Beams . . . 26
2.3 UCA-Based Generation Mechanism of OAM Beams . . . 26
2.3.1 Conjugate Mode Realization via Symmetric Dual-Port Feeding . . . 29
2.4 Summary . . . 29

3 Design and Performance Evaluation of the Proposed OAM Antenna 31
3.1 Antenna Design Requirements and Specification . . . 32
3.1.1 Target Performance Requirements . . . 32
3.1.2 Design Challenges and Considerations . . . 33
3.2 Antenna Configuration and Working Mechanism . . . 34
3.2.1 Antenna Geometry and Layer Description . . . 34
3.2.2 UCA Element Layout and Phase Feeding Principle . . . 36
3.2.3 Geometric Parameters of the Proposed Antenna . . . 36
3.3 Simulation and Experimental Validation . . . 38
3.3.1 Fabricated Prototype . . . 40
3.3.2 Measurement Setup . . . 40
3.3.3 S-Parameter Validation . . . 41
3.3.4 Near-Field Phase and Amplitude Verification . . . 44
3.3.5 Far-Field Radiation Patterns . . . 46
3.4 Performance Comparison . . . 48
3.5 Summary . . . 49

4 Conclusion and Future Work 51
4.1 Summary of Research . . . 51
4.2 Future Work . . . 52

References 53

List of Figures

1 Expérimentation d'un lien OAM à 2.4 GHz sur 442 m: antenne parabolique émettrice et deux antennes Yagi réceptrices [45]. xii
2 Montage expérimental de Mahmouli et al.: transmission d'un faisceau OAM à 60 GHz au moyen d'une HP ou d'une SPP, transportant une vidéo non compressée de 4 Gbps sur 400 mm [119]. xiii
3 Illustrations conceptuelles du moment cinétique: (a) un objet tournant sur son propre axe (SAM); (b) un objet en orbite autour d'un axe externe (OAM); (c) un faisceau polarisé circulairement portant un SAM via la rotation du champ électrique; (d) un front d'onde hélicoïdal représentant l'OAM [107,131]. . . . xv
4 Fronts d'onde, intensité et distribution de phase pour les charges $l = 0, 1, 2, 3$: (a) $l = 0$; (b) $l = 1$; (c) $l = 2$; (d) $l = 3$ [132]. xvi
5 Géométrie d'un réseau circulaire uniforme à N éléments. xviii
6 Disposition de l'antenne : (a) Vue de dessus montrant les deux réseaux UCA ; (b) Vue de dessous avec les quatre ports d'alimentation. xxi

1.1 Hybridizing FPC and FZC antenna [54]. 5
1.2 Dual-band shared-aperture antenna [55]. 6
1.3 Dual-broadband dual-polarized magnetoelectric-dipole antenna [56]. 7
1.4 A single layer dual-band shared-aperture antenna [57]. 8
1.5 Dual-Band Shared Aperture Reflectarray and Patch Antenna [58]. 9
1.6 Multiband MIMO Microwave and Mm-Wave Antenna [59]. 10
1.7 Illustration of 2.4 GHz OAM wireless communication experiment over a 442-meter link using a parabolic transmitting antenna and dual Yagi receiving antennas [45]. 12
1.8 Experimental setup by Mahmouli et al. for 60 GHz OAM beam transmission using a HP or a SPP to send a 4-Gbps uncompressed video signal over a 400 mm wireless link [119]. 12
1.9 Uniform Circular Array antenna [62]. 14
1.10 Spiral parabolic reflector antenna [45]. 15
1.11 Multimode circular patch antenna with three concentric radiating patches [75]. 16
1.12 Configuration of circular traveling-wave antenna [79]. 17
1.13 Fabricated flat-lensed SPP based on multilayer phase-shifting surface for generating focused OAM beam at 60 GHz [83]. 18
1.14 Cylindrical DRA for OAM generation [93]. 19

2.1 Conceptual illustrations of angular momentum: (a) A spinning object exhibiting SAM; (b) An orbiting object exhibiting OAM; (c) A circularly polarized beam carrying SAM via electric field rotation; (d) A helical wavefront structure representing OAM [107,131]. 24
2.2 OAM beam wavefronts, intensity, and phase distributions for topological charges $l = 0, 1, 2, 3$: (a) $l = 0$; (b) $l = 1$; (c) $l = 2$; (d) $l = 3$ [132]. 25
2.3 Geometry of a N-element uniform circular array. 27

3.1 Antenna layout: (a) Top view showing dual UCA rings; (b) Bottom view with four feeding ports. 35
3.2 Patch rotation layout illustrating 45° inter-element alignment for $l = \pm 1$. . . 37
3.3 Fabricated prototype of the proposed dual-band mode-switchable OAM antenna: (a) Top view; (b) Bottom view. 39
3.4 Measurement setups: (a) S-parameter testing with VNA; (b) Near-field scanning; (c) Far-field radiation pattern acquisition. 40
3.5 Simulated and measured S-parameters of the proposed antenna at 5.8 GHz . 41
3.6 Simulated and measured S-parameters of the proposed antenna at 28 GHz . 42
3.7 Simulated amplitude and phase distributions of the y-component in the plane at $z = 60$ mm from the antenna surface at 5.8 GHz: (a) Port 1 excitation (OAM mode $l = -1$); (b) Port 2 excitation (OAM mode $l = +1$). 43
3.8 Measured amplitude and phase distributions of the y-component in the plane at $z = 60$ mm from the antenna surface at 5.8 GHz: (a) Port 1 excitation (OAM mode $l = -1$); (b) Port 2 excitation (OAM mode $l = +1$). 44
3.9 Simulated amplitude and phase distributions of the y-component in the plane at $z = 60$ mm from the antenna surface at 28 GHz: (a) Port 3 excitation (OAM mode $l = +1$); (b) Port 4 excitation (OAM mode $l = -1$). 45
3.10 Measured amplitude and phase distributions of the y-component in the plane at $z = 60$ mm from the antenna surface at 28 GHz: (a) Port 3 excitation (OAM mode $l = +1$); (b) Port 4 excitation (OAM mode $l = -1$). 46
3.11 Simulated and measured normalized gain radiation patterns at 5.8 GHz: (a) Port 1 excitation ($l = -1$); (b) Port 2 excitation ($l = +1$). 47
3.12 Simulated and measured normalized gain radiation patterns at 28 GHz: (a) Port 3 excitation ($l = +1$); (b) Port 4 excitation ($l = -1$). 48

List of Abbreviations

5G	fifth-generation
BW	bandwidth
CMAs	Circular microstrip antennas
DRA	dielectric resonator antenna
FPC	Fabry–Pérot cavity
FZP	Fresnel zone plate
Gbps	Gigabits-Per-Second
GCPW	grounded coplanar waveguide
HPs	holographic plates
IoT	Internet of Things
LG	Laguerre–Gaussian
LHCP	left-handed circular polarization
LOS	Line-of-Sight
MDM	mode-division multiplexing
MIMO	multiple-input multiple-output
mm-wave	millimeter-wave
OAM	orbital angular momentum
PB	Pancharatnam–Berry
PCB	printed circuit board
PP	polypropylene
PSS	phase-shifting surfaces
RF	radio-frequency
RHCP	right-handed circular polarization
RTWA	ring travelling-wave antenna
SAM	spin angular momentum
SIW	substrate integrated waveguide
SNR	signal-to-noise ratio
SPPs	spiral phase plates
UCA	uniform circular array
V2V	vehicle-to-everything
VNA	vector network analyzer

Chapter 1

Introduction

1.1 Background and Motivation

With the rapid advancement of wireless communication technologies—driven by emerging applications such as the internet of things (IoT), intelligent transportation systems, and fifth-generation (5G) and beyond—the demand for high-capacity, low-latency, and spectrum-efficient communication systems has increased dramatically. To meet these requirements, microwave-based communication systems have been widely adopted due to their mature infrastructure, reliable transmission, and broad coverage. However, the limited spectrum available in the conventional microwave band has led to severe congestion, restricting the ability of existing systems to accommodate the massive number of connected devices and high-throughput demands of next-generation networks [1–7].

To address this issue, millimeter-wave (mm-wave) technology has attracted significant attention owing to its abundant spectrum resources, ultra-high data rates, and low-latency characteristics [1–3,8]. Mm-wave communication has emerged as a core technology for 5G and future wireless systems. However, mm-wave signals suffer from high propagation loss, limited penetration through obstacles, and a restricted coverage range, making it impractical to rely solely on mm-wave systems for large-scale wireless deployments [9–15].

As a result, fully replacing microwave technology with mm-wave solutions remains unlikely in the near future. Recognizing the complementary strengths of both frequency bands, the integration of microwave and mm-wave technologies has become a fundamental feature of next-generation wireless

communication systems [15, 16]. In this context, multi-band antennas play a crucial role, enabling flexible operation across different frequency bands to enhance coverage, improve communication reliability, and achieve more efficient spectrum utilization [17–23]. Therefore, investigating compact and mode-switchable antenna structures that can support both microwave and mm-wave frequencies is of great importance for advancing 5G and beyond [1, 2, 9, 10, 16, 24–34].

The increasing demand for high-speed and high-capacity wireless communication networks has spurred extensive research aimed at enhancing channel capacity and spectral efficiency. Traditionally, efforts in this area have focused on increasing bandwidth (BW) and improving the signal-to-noise ratio (SNR). According to Shannon's theorem, the theoretical channel capacity is given by $C = B\log_2(1+\mathrm{SNR})$, where B denotes the system BW and SNR is the signal-to-noise ratio. While this equation suggests that capacity can be improved through either wider BW or higher SNR, both approaches are constrained in practical implementations. BW is often limited by gain-BW trade-offs or axial ratio constraints, whereas SNR can be significantly degraded by environmental interference, multipath fading, and system noise [35–39].

As wireless systems continue to evolve, these limitations have motivated the exploration of alternative strategies to boost spectral efficiency without solely relying on BW or SNR improvements. Among them, spatial multiplexing has emerged as a powerful technique that allows multiple data streams to be transmitted simultaneously over the same frequency band by exploiting spatial domain diversity [40]. One particularly promising form of spatial multiplexing is based on the use of orbital angular momentum (OAM) modes. Unlike conventional multiplexing schemes that rely on frequency, polarization, or spatial separation, OAM antennas utilize the orthogonality of distinct topological charges to create independent spatial channels. OAM-based communication systems generate helical wavefronts characterized by an azimuthal phase term of the form $\exp(-jl\phi)$, where l is the OAM mode index and ϕ is the azimuth angle. By leveraging the orthogonality of distinct OAM modes, these antennas enable the establishment of multiple independent spatial channels [41, 42]. This form of spatial multiplexing, commonly referred to as mode-division multiplexing (MDM), allows multiple data streams to coexist on the same frequency without additional BW consumption [43, 44]. Since the first experimental demonstration of radio OAM transmission in 2012 [45], significant research efforts have been directed toward developing practical OAM antennas and exploring their potential in high-capacity wireless communication systems [46–49]. In addition to their spectral efficiency benefits, OAM-capable antennas are increasingly being consid-

ered for integration into dual-band microwave and mm-wave systems. Such integration supports multi-band operation while enabling dynamic mode-switching, presenting a promising solution to the dual challenge of frequency congestion and capacity enhancement in next-generation wireless networks [48, 50–53].

Recent studies have proposed a variety of techniques to achieve multi-band functionality in antenna systems, including stacked design approach [54–56], and same-layer design approach [57–59]. In parallel, a range of strategies has been developed for generating OAM waves, such as uniform circular array (UCA) [60–69], spiral parabolic reflector [45, 70–72], circularly polarised patch antenna [73–78], ring travelling-wave (leaky-wave) antenna [49, 79–82], metasurface or reflectarray [50, 52, 83–90], and dielectric resonator antenna (DRA) [91–93]. While each of these methods offers specific advantages, achieving mode-switchable OAM generation across multiple frequency bands remains a significant challenge. Key limitations include the complexity of feeding structures, the need for precise phase control, inadequate isolation between bands, and constraints on physical scalability. To address these challenges, this thesis proposes a compact, dual-band OAM antenna featuring a mode-switchable mechanism based on symmetric dual-port excitation. The design enables stable generation of OAM modes ($l = \pm 1$) at both 5.8 and 28 GHz, without requiring external phase-shifting networks. A comprehensive study involving design, simulation, fabrication, and experimental validation is presented.

1.2 Research Status

1.2.1 Design Strategies for Multi-Band and Integrated Microwave and Mm-Wave Antennas

While the previous section outlined the system-level motivations for integrating microwave and mm-wave frequency bands in future wireless networks, this subsection focuses specifically on the antenna-level design strategies that enable such integration. In particular, it examines the architectural evolution and technical approaches that support dual-band and multi-band operation within compact and efficient antenna systems.

In the early stages of dual-band or multi-band antenna development, the most common approach was to place two independent antennas adjacent to each other, each operating at a distinct frequency band [94–96]. However, this method typically resulted in large overall dimensions and low aperture efficiency, which limited its suitability for compact or integrated systems. To overcome these limitations, the concept of shared-aperture antennas was introduced and has since been regarded as a promising solution [54–56, 58, 59, 97–103]. By integrating multiple radiating structures—each designed for a specific frequency band—into a unified topology, shared-aperture antenna systems offer notable advantages, including reduced size, lower system weight, and improved aperture efficiency [104].

In the following sections, various antenna design methodologies for integrating microwave and mm-wave bands are explored.

1.2.1.1 Stacked Design Approach

The stacked design approach is widely adopted for dual- or multi-band antenna integration across microwave and mm-wave regimes. Distinct radiating or resonant elements for each band are vertically superimposed, enabling aperture sharing and a reduced planar footprint—though often at the expense of increased profile height. In the following, we review three representative stacked-design approaches for shared-aperture dual- or multi-band antennas: a Fabry–Pérot cavity (FPC) combined with a Fresnel zone plate (FZP) metasurface, a low-frequency patch nested within a high-frequency substrate integrated waveguide (SIW) slot-array, and a magnetoelectric-dipole layer stacked beneath tilted-horn radiators.

A classic stacked-design approach was demonstrated by Zhu et al., who hybridize a FPC with a FZP metasurface to achieve operation at 3 and 28 GHz [54]. As shown in Fig. 1.1, the antenna comprises a dual-band patch radiator placed at the bottom, serving as a common source for both frequency bands. For the sub-6 GHz band, the structure forms a Fabry–Pérot resonant cavity by sandwiching a partially reflective FZP metasurface above a metallic ground plane. At the same time, the same FZP structure acts as a focusing lens for the mm-wave signal, enabling beam collimation and gain enhancement at 28 GHz. This stacked configuration demonstrates the effective reuse of radiating aperture across disparate frequency bands while maintaining high gain performance, showcasing a viable approach for compact and efficient multi-band antenna integration.

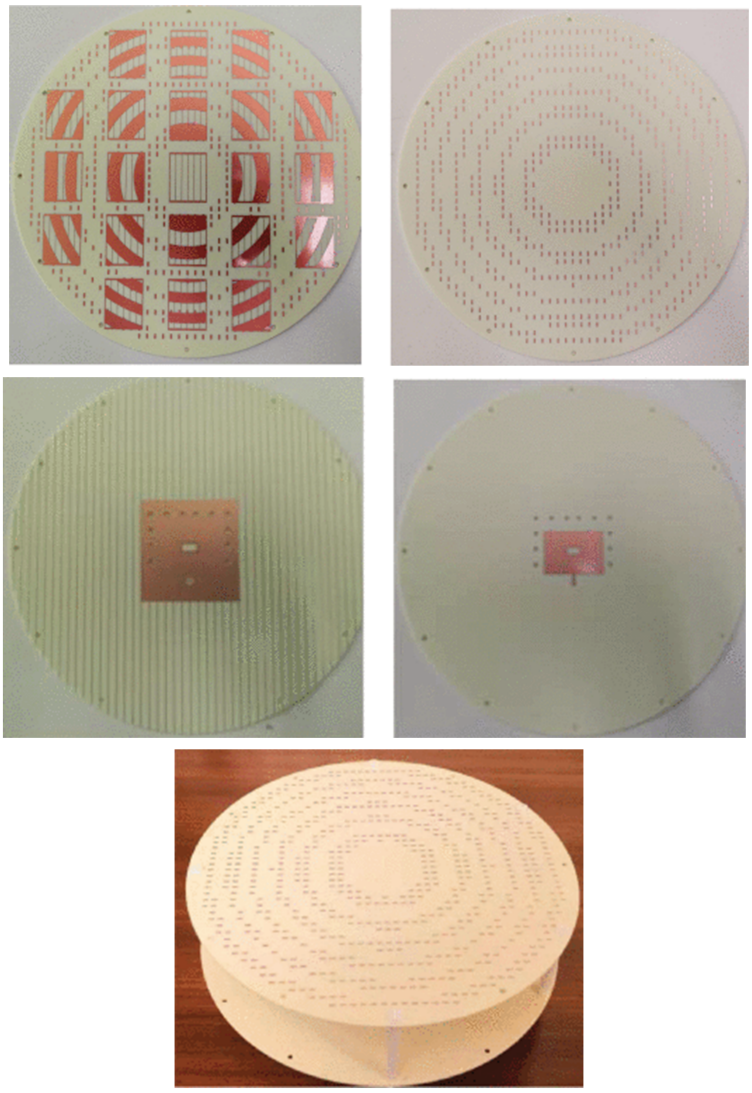

Figure 1.1: Hybridizing FPC and FZC antenna [54].

Building on similar aperture-sharing principles, Zhang et al. propose a shared-aperture solution combining a 3.5 GHz patch with a 12×12 SIW slot-array for 60 GHz operation [55]. As shown in Fig. 1.2, the antenna uses the 60 GHz SIW slot array as the radiator for the 3.5 GHz band by reusing its patch structure. For the sub-6 GHz band, four tuning vias and an H-slot in the top metal layer fine-tune the rectangular patch's resonance to 3.5 GHz without impacting the mm-wave performance, producing a broadside pattern with a peak gain of 7.3 dBi. Simultaneously, for the 60 GHz band, the 12×12 SIW slot-array—fed through a multiway SIW power divider and compact right-angle transition—achieves a 24 dBi gain and a 6.4% impedance bandwidth (58.6–62.5 GHz). This structure-reuse topology yields a high aperture reuse efficiency of 77% and channel isolation

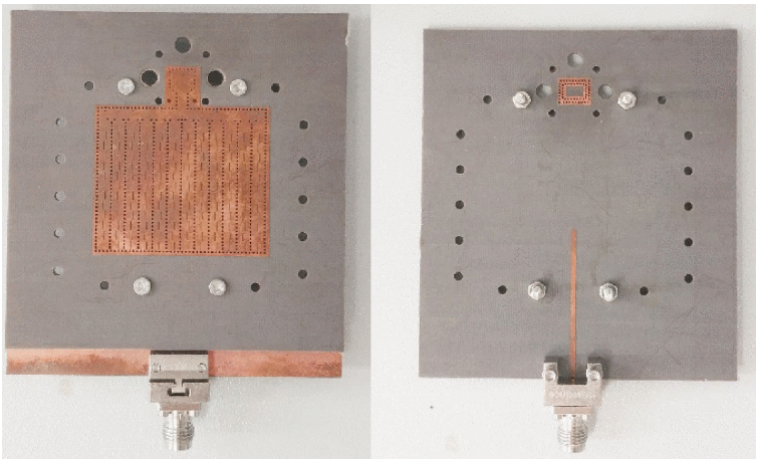

Figure 1.2: Dual-band shared-aperture antenna [55].

better than 130 dB at 3.5 GHz and 65 dB at 60 GHz, demonstrating a compact ($80\times86\times2.6$ mm^3) and efficient solution for large-frequency-ratio dual-band shared-aperture antenna design.

In another example, Cheng and Dong present a dual-broadband, dual-polarized magnetoelectric-dipole design, integrating four SIW-fed magnetoelectric-dipoles and four tilted-wall horns to cover 2.35–3.93 GHz and 24–34 GHz [56]. As shown in Fig. 1.3, the antenna is constructed on two Rogers substrates separated by a thin air gap: the top layer (L1) carries four SIW-cavity-fed magnetoelectric-dipoles printed on Rogers 5880, while the middle Rogers 4350B layer (L2) supports the SIW cavities and orthogonal aperture-coupled slots. The four horns, machined from a single aluminum block, are mounted above the magnetoelectric-dipoles via grounded coplanar waveguide (GCPW)-to-SIW transitions. For the sub-6 GHz band, the four magnetoelectric-dipoles—each composed of orthogonal electric and magnetic loops—combine electromagnetically to form a dual-polarized radiator with 50.31 % impedance BW (2.35–3.93 GHz) and a peak gain of 10.67 dBi, aided by a 25 mm metal cavity for enhanced efficiency. Simultaneously, for the 24–34 GHz band, each SIW-fed magnetoelectric-dipole excites a horn with an inclined inner wall, producing a tilted beam and enabling $\pm20^\circ$ two-dimensional beam switching with dual polarization; this achieves 33.91 % BW (24–33.91 GHz) and a peak gain of 14.85 dBi. This layered shared-aperture configuration demonstrates robust reuse of the radiating aperture across a large frequency ratio ($\approx 9.2:1$), dual-polarization in both bands, high port isolation (>18 dB at S-band and >15 dB at mm-wave), and offering an effective solution for dual-band 5G base-station antenna integration.

These examples collectively highlight the versatility and performance advantages of stacked design strategies for dual-band antenna integration. By enabling shared aperture operation and

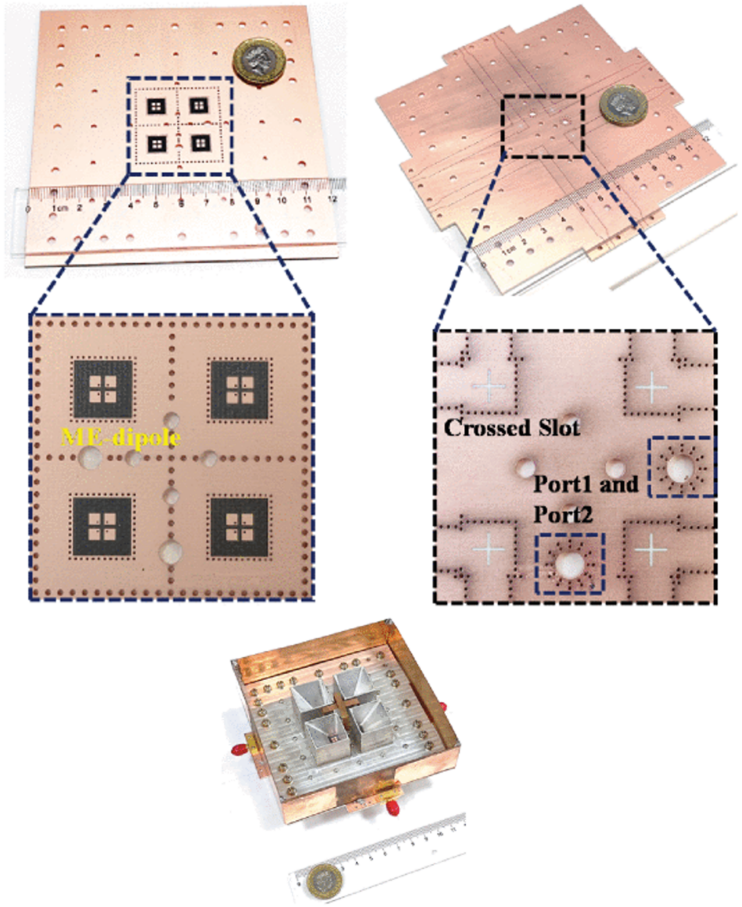

Figure 1.3: Dual-broadband dual-polarized magnetoelectric-dipole antenna [56].

efficient isolation between bands, the stacked approach provides a strong foundation for compact, high-performance antennas in future wireless and multi-functional communication systems.

1.2.1.2 Same-Layer Design Approach

The same-layer design approach achieves dual-band operation by embedding radiators for different frequency bands on a single planar substrate. Eliminating vertical layering simplifies fabrication, minimizes profile thickness, and facilitates integration into vehicular or handheld devices where low-profile form factors are critical. Compared with stacked designs, same-layer schemes demand more careful modal decoupling and shared-aperture optimization. The following present three illustrative same-layer designs: an annular-ring TM_{12}-mode patch combined with an SIW slotted cavity, a shared-aperture reflectarray coexisting with a patch-array, and a multiband multiple-input multiple-output (MIMO) monopole array with a defected ground tapered slot.

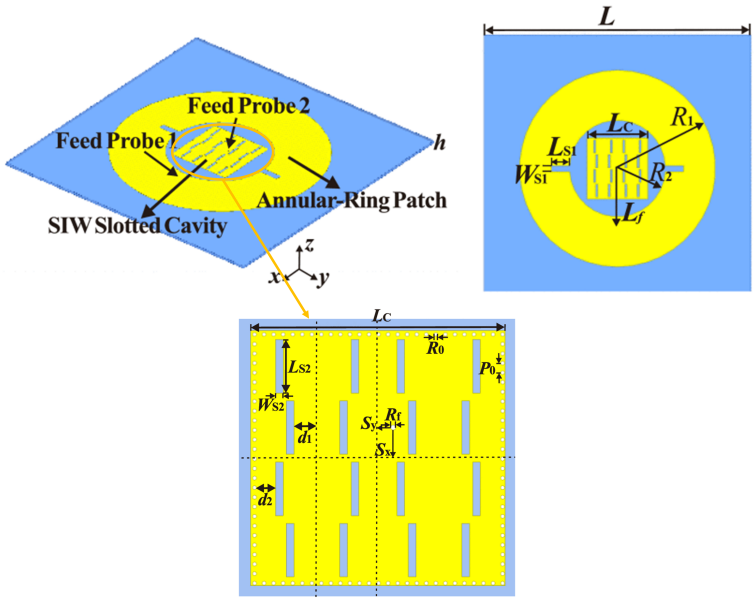

Figure 1.4: A single layer dual-band shared-aperture antenna [57].

In the first design, Wang et al. propose a single-layer antenna that nests an annular-ring TM_{12}-mode patch and an SIW slotted cavity to cover the Vehicle-to-Everything (V2X) band (5.905–5.925 GHz) and the 5G n257 mm-wave band (26.5–29.5 GHz) [57]. As shown in Fig. 1.4, the antenna is printed on a Rogers 5880 substrate: the top layer carries an annular-ring patch (outer radius R_1, inner radius R_2) excited by a coaxial probe at a distance L_f from center. By etching a pair of slots at the TM_{12} out-of-phase locations, the annular-ring patch achieves a 3.7 % impedance BW (5.74–5.96 GHz) and a peak gain of 10.8 dBi. Simultaneously, a 4×4 SIW slotted cavity-backed antenna—realized by metallized vias of radius R_0 and spacing p_0 in the same Rogers 5880 layer—supports the TE_{440} mode. Half-wavelength slots (size $L_{S2} \times W_{S2}$) are etched at the cavity's standing-wave peaks and fed via a coaxial probe positioned at (S_x, S_y), yielding a 10.9 % BW (26.66–29.72 GHz), sidelobe level below –14.8 dB, and peak gain of 13.7 dBi. The nested, shared-aperture configuration demonstrates isolation better than 45 dB between ports, and an ultralow profile ($\approx 0.015\,\lambda_0$ at 5.915 GHz), offering a compact, high-gain, low-sidelobe solution for dual-band vehicular communications.

A different approach is presented by Serup et al., who integrate a 3×3 S-band patch array with a Ka-band reflectarray within the same 156 mm × 156 mm aperture to achieve operation at 3.5 and 25.8 GHz [58]. As shown in Fig. 1.5, the antenna comprises nine low-frequency square patches printed on the top Rogers RO4003 substrate layer (forming a 3×3 array) and a high-frequency

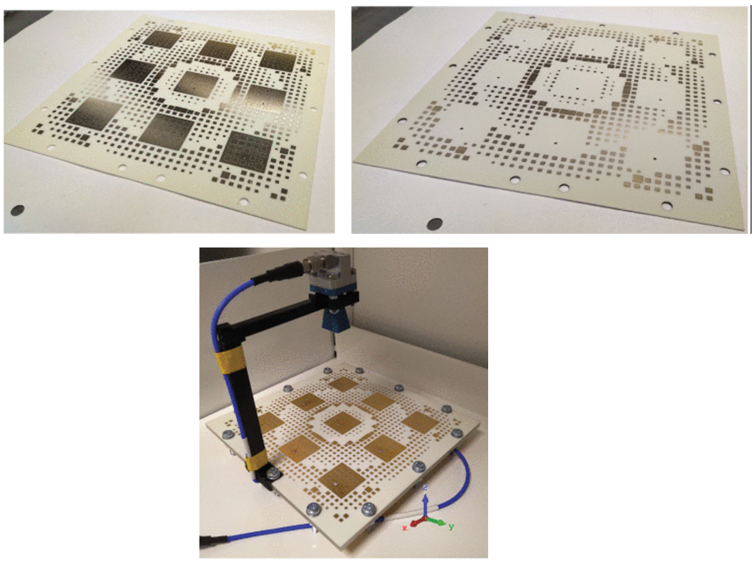

Figure 1.5: Dual-Band Shared Aperture Reflectarray and Patch Antenna [58].

reflectarray realized by 980 stacked square-patch unit cells and 200 annular-loop cuts distributed across the top and bottom RO4003 layers, all separated by a 3 mm polypropylene (PP) layer. For the S-band (3.5 GHz), the low-frequency patch array—fed through nine independent SMA connectors—produces a broadside pattern with 13.70 dBi peak gain and 200 MHz (6%) impedance BW, aided by the added PP layer that enhances BW through increased substrate thickness. Simultaneously, for the Ka-band (25.8 GHz), the reflectarray—illuminated by a standard gain horn at an optimized 80 mm height—utilizes the stacked square-patch and annular-loop unit elements to impose the required phase distribution, achieving a 27.65 dBi peak realized gain and 5.1 GHz (20%) BW. This layered, shared-aperture configuration demonstrates high aperture reuse efficiency (44.5%) and excellent channel isolation, all within a compact 156 × 156 × 4.624 mm^3 form factor, offering an effective solution for high frequency-ratio dual-band antenna integration in nanosatellite applications.

Finally, Ikram et al. demonstrate a multiband MIMO antenna system that combines four dual-band monopoles with a dual-function tapered slot etched in the ground plane to cover 2.45 GHz, 2.6 GHz, 5.2 GHz, 24 GHz, and 28 GHz [59]. As shown in Fig. 1.6, the antenna comprises four dual-band printed monopoles—each covering 2.45 GHz and 5.2 GHz—fabricated on a 0.51 mm-thick Rogers 5880 substrate (104 mm × 104 mm). For the sub-6 GHz bands, the four monopoles combine to form a compact MIMO array with impedance bandwidths of 2.40–2.80 GHz and 5.10–5.60 GHz, achieving a peak gain of 5 dBi and inter-element isolation exceeding 16 dB. Simultaneously, a tapered

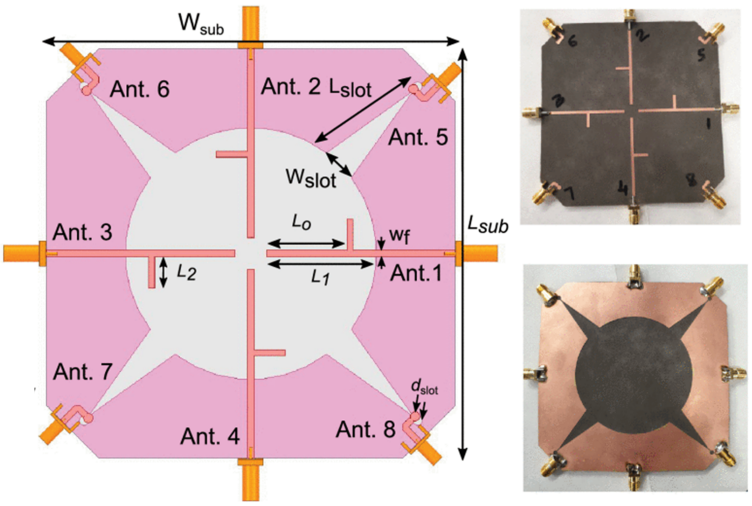

Figure 1.6: Multiband MIMO Microwave and Mm-Wave Antenna [59].

slot defined in the ground plane serves a dual role: it acts as a defected ground structure to suppress coupling among the low-band monopoles and, when excited by a $\lambda_0/4$-terminated microstrip feed, operates as a high-gain Vivaldi-type slot antenna for the 28 GHz band. The tapered slot achieves 23–30 GHz BW with a peak gain of 11 dBi and maintains isolation above 17 dB across all bands. This single-layer, shared-aperture configuration demonstrates efficient reuse of the radiating aperture across widely separated frequency bands (microwave and mm-wave), high port isolation, and a low-profile footprint ($104 \times 104 \times 0.51\,\text{mm}^3$), offering an effective solution for compact multiband MIMO integration.

Taken together, these three same-layer implementations demonstrate how carefully engineered modal decoupling and aperture sharing can achieve wide impedance bandwidths, strong inter-band isolation, and low profile within a single planar substrate. In particular, nesting a TM_{12} patch inside an SIW cavity yields an ultralow profile for V2X and mm-wave coexistence; embedding a Ka-band reflectarray above an S-band patch array maximizes aperture reuse in a compact footprint; and introducing a tapered slot in the ground plane of a MIMO monopole array enables multi-frequency operation without additional vertical stacking. As a result, same-layer topologies provide a cost-effective, low-profile solution for emerging 5G, vehicular, and IoT platforms where form factor and fabrication simplicity are critical.

1.2.2 Overview of OAM Antenna Architectures and Generation Techniques

Since the groundbreaking work by L.Allen et al. in 1992, which systematically analyzed the OAM carried by light waves and revealed its correspondence to the helical phase structure $\exp(-jl\phi)$ in Laguerre–Gaussian (LG) modes [105], this property has attracted widespread attention. It is now regarded as a key physical mechanism that offers an additional degree of freedom for multiplexing, with the potential to enhance the capacity of wireless communication systems. One of the most distinctive characteristics of OAM beams is their helical phase wavefronts, which cause the beam to twist as it propagates. These beams exhibit a phase singularity at the center of the wavefront, resulting in a null in field amplitude along the propagation axis. Consequently, the intensity distribution forms a ring-like or "donut-shaped" profile, which is a hallmark of OAM-carrying modes. Since different OAM modes are mutually orthogonal and the topological charge l can, in principle, take an infinite number of discrete values, it is theoretically possible to transmit an unlimited number of independent data channels over the same carrier frequency [42, 106–108].

Following this initial discovery, extensive research on OAM beams has flourished [109–117]. Although early investigations primarily focused on the optical domain, it is recognized that optical waves and radio waves are fundamentally both electromagnetic waves, differing mainly in their frequency ranges. This fundamental similarity indicates that OAM also holds considerable potential in the radio-frequency (RF) domain. Accordingly, the following sections review recent advances and explore practical methods for generating OAM beams in RF domains.

1.2.2.1 Recent Advances of OAM beams in RF Domains

Since the pioneering demonstration by Thidé et al. in 2007, who first proposed the application of OAM in wireless communications [118], substantial research has emerged focusing on both theoretical developments and practical implementations. Notably, Tamburini et al. in 2012 successfully demonstrated the first practical OAM wireless communication link at 2.4 GHz, achieving dual-mode multiplexing over a 442-meter link by using a parabolic reflector transmitting antenna and Yagi receiving antennas, as shown in Fig. 1.7 [45].

Progress continued rapidly into mm-wave frequencies. Mahmouli et al. in 2013 employed holographic plates (HPs) or spiral phase plates (SPPs) to generate OAM beams at 60 GHz, successfully

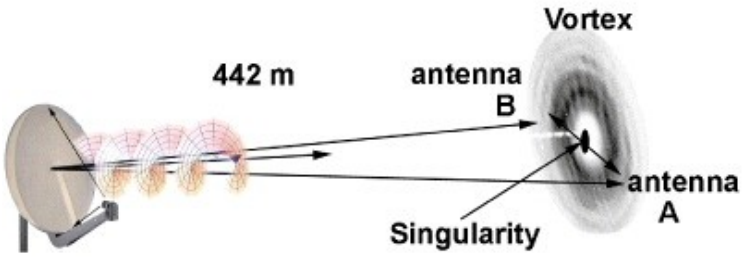

Figure 1.7: Illustration of 2.4 GHz OAM wireless communication experiment over a 442-meter link using a parabolic transmitting antenna and dual Yagi receiving antennas [45].

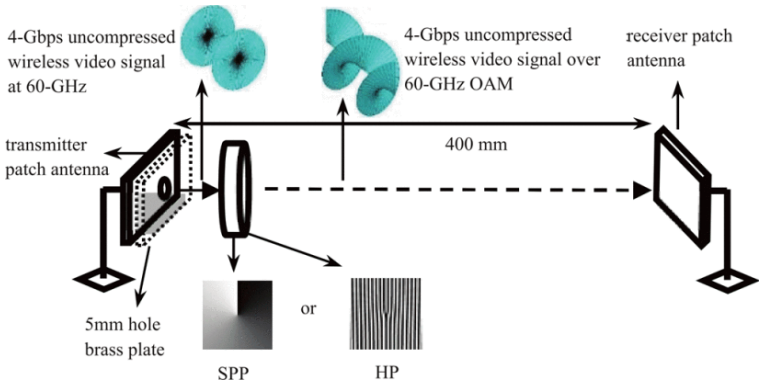

Figure 1.8: Experimental setup by Mahmouli et al. for 60 GHz OAM beam transmission using a HP or a SPP to send a 4-Gbps uncompressed video signal over a 400 mm wireless link [119].

transmitting a 4-Gbps uncompressed video signal over a short-range link as shown in Fig. 1.8 [119]. Subsequently, Yan et al. in 2014 demonstrated a mm-wave link at 28 GHz, combining four OAM modes and two orthogonal polarizations to achieve a data rate of 32 Gbps and spectral efficiency approaching 16 bit/s/Hz within a 2.5-meter transmission distance [48]. Hui et al. further explored the 60 GHz band in 2015, utilizing circular cavity leaky-wave antennas to transmit OAM modes $l = \pm 3$, successfully transmitting image signals and square wave signals [49]. At lower RF frequencies, Chen et al. in 2016 generated an OAM beam with mode number $l = 2$ using an elliptical patch antenna at 2 GHz, demonstrating successful image data transmission [78].

Industrial-level advancements emerged notably from NTT Corporation. In 2018, Sasaki et al. proposed a multi-ring UCA-based OAM-MIMO system at 28 GHz, achieving a remarkable throughput of 100 Gbps at 10-meters by multiplexing multiple OAM beams generated from the same ring and subsequently demultiplexed via advanced MIMO processing algorithms [120]. In 2021, NTT further improved the system by incorporating polarization multiplexing techniques, doubling

the throughput to 200 Gbps at the same distance [121]. The same group also extended their work to outdoor environments in 2021, demonstrating an OAM wireless link at 40 GHz that successfully transmitted data at 117 Gbps over 200-meters [122]. These industrial-level demonstrations have drawn extensive attention from academia and industry, laying a solid foundation for future OAM-based technologies in next-generation wireless communication systems.

Apart from communication systems, OAM-based modulation has also found promising applications in radar imaging. Liu et al. introduced an OAM-modulated radar imaging methodology in 2014, providing new insights into radar systems' angular resolution enhancements [123].

1.2.2.2 Generation Methods of OAM Beams in RF Domains

OAM beams in the RF domains can be generated either by discretely phased antenna arrays or by radiating apertures that inherently produce vortex wavefronts. This section provides a summary of six representative antenna architectures that have been widely reported in the literature for RF OAM generation.

- **Uniform Circular Array (UCA) [60–69]**: A UCA consists of N identical elements uniformly distributed on a plane. OAM beams can be synthesized by exciting the n-th element with a progressive phase shift $\phi_n = \frac{2\pi ln}{N}$, where l denotes the topological charge. This results in a far-field phase wavefront of the form $e^{jl\phi}$, corresponding to an OAM mode of order l. Such a phased excitation enables the generation of multiple OAM modes, where the mode index l can range within $(-N/2, N/2)$. This structure has been widely used due to its reconfigurability and theoretical support for mode multiplexing. Further details on the UCA-based antenna proposed in this study are discussed in Chapter 2.

  Advantage: capable of supporting multiple OAM modes with high flexibility; compatible with reconfigurable beamforming.

  Limitation: the feed network becomes increasingly complex for large element numbers or high-order modes.

  Reference structure: a representative implementation of UCA with OAM generation can be found in [62], as shown in Fig. 1.9.

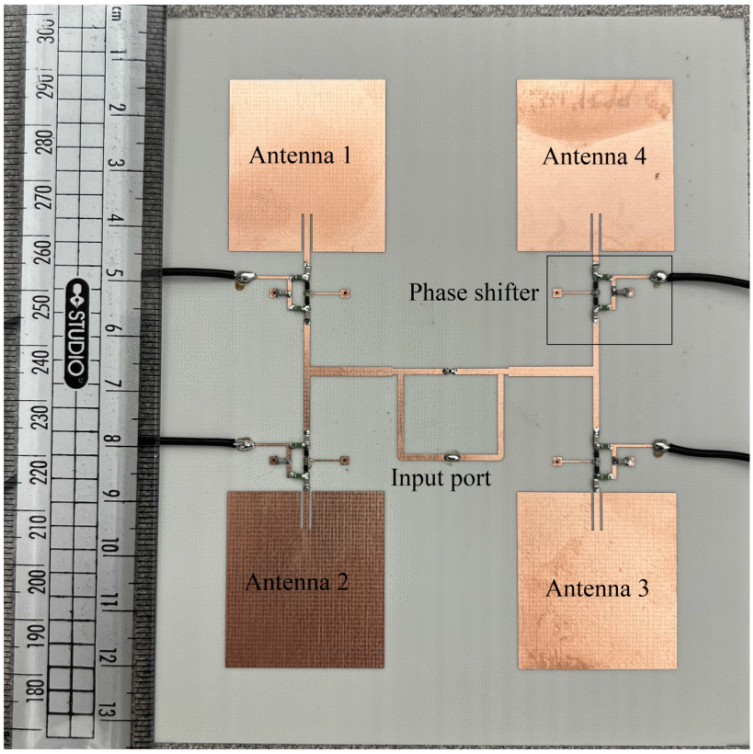

Figure 1.9: Uniform Circular Array antenna [62].

- **Spiral Parabolic Reflector [45, 70–72]**: A conventional parabolic reflector can be transformed into an OAM beam generator by introducing an axial displacement along the reflector surface in a spiral manner. When the surface deviation equals half of the wavelength ($\lambda/2$), the reflected wavefront acquires a phase term $e^{\pm j\phi}$, resulting in an OAM mode of $l = \pm 1$ when illuminated by a circularly polarised wave. This passive method manipulates the path length across azimuthal directions to achieve the desired helical phase wavefront, without requiring a complex feed networks.

  Advantage: simple implementation with high gain, suitable for far-field applications.

  Limitation: physically large and fixed-mode; lacks reconfigurability.

  Reference structure: a representative spiral reflector implementation can be found in [45], as illustrated in Fig. 1.10.

- **Circularly Polarised Patch Antenna [73–78]**: Circular microstrip antennas (CMAs) have emerged as a promising solution for generating OAM beams in planar microwave systems. These antennas operate by exciting higher-order resonant modes—typically TM_{n1}—whose



Figure 1.10: Spiral parabolic reflector antenna [45].

intrinsic azimuthal field dependence takes the form of $e^{jl\phi}$, enabling the synthesis of OAM modes.

Advantage: low-profile planar design; easy integration with RF front-end circuits; capable of supporting multi-mode and multi-band operation through structural modification; recent works allow single-feed high-order OAM generation without external circuitry.

Limitation: OAM mode purity and inter-mode isolation remain sensitive to fabrication tolerances and feed alignment; impedance and axial ratio bandwidths are typically narrow due to the resonant nature of patch elements.

Reference structure: a representative circularly polarised multimode patch antenna composed of three concentric circular patches for generating multiple OAM modes is presented in [75], as shown in Fig. 1.11.

- **Ring Travelling-Wave (Leaky-Wave) Antenna [49, 79–82]**: A ring travelling-wave antenna (RTWA) consists of a closed-loop waveguide or resonator that supports an azimuthally propagating surface wave. When the guided wavelength matches an integer multiple of the ring's perimeter, a standing or travelling wave is established. The resulting current distribution varies continuously with the azimuthal angle ϕ, forming a phase profile of $e^{jl\phi}$, where l corresponds to the mode number. This configuration enables the generation of OAM beams

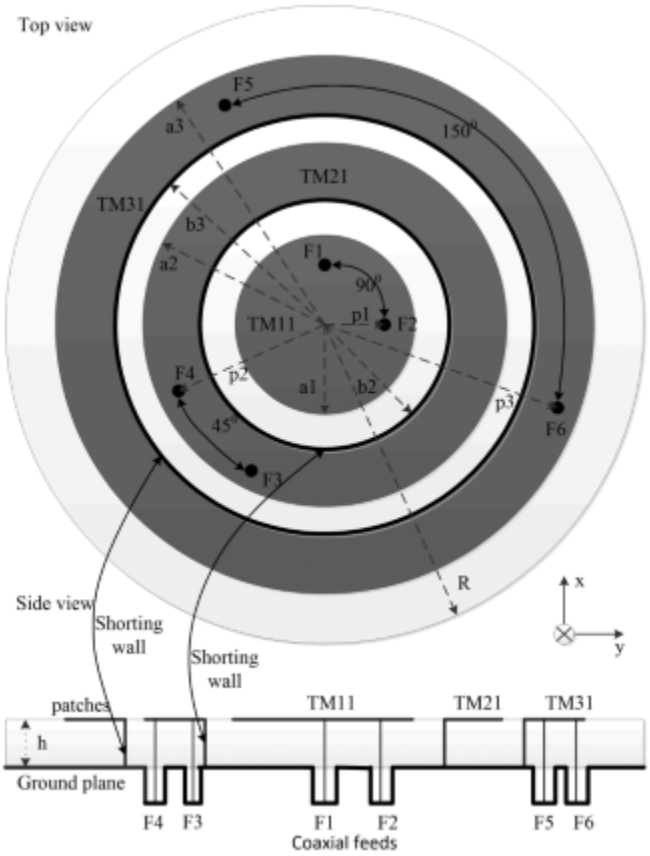

Figure 1.11: Multimode circular patch antenna with three concentric radiating patches [75].

with opposite mode indices (e.g., $l = \pm 1$) and allows for concentric arrangement of multiple rings with different radii to achieve spatial multiplexing of multiple OAM channels.

Advantage: intrinsic generation of high-purity OAM modes with smooth phase profile; suitable for dense OAM multiplexing.

Limitation: narrow bandwidth due to resonant nature; radiation efficiency decreases for high-order OAM modes.

Reference structure: a representative implementation of a ring travelling-wave antenna for OAM multiplexing is described in [79], as illustrated in Fig. 1.12.

- **Metasurface or Reflectarray [50, 52, 83–90]**: Metasurfaces and reflectarrays are planar structures composed of subwavelength-scale unit cells engineered to manipulate the phase of incident electromagnetic waves. To generate OAM beams, such structures impose an azimuthally varying phase shift $\Phi(\phi) = l\phi$ across the aperture, where l is the OAM mode index and ϕ is the azimuthal angle.

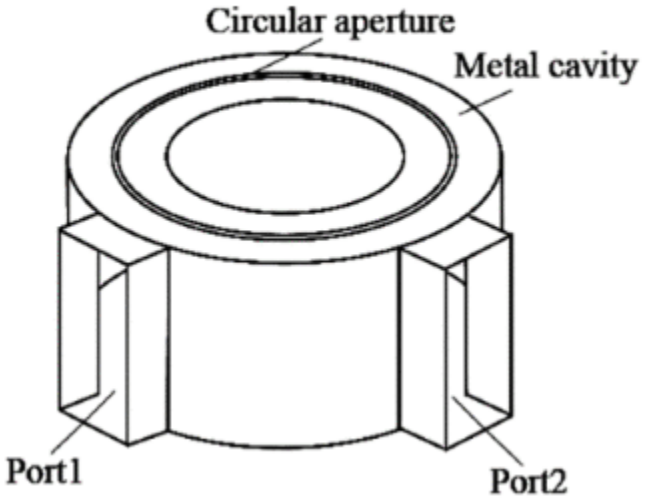

Figure 1.12: Configuration of circular traveling-wave antenna [79].

OAM-mode generation is typically achieved through reflection- or transmission-type designs. In reflective metasurfaces, the required phase distribution can be implemented via Pancharatnam–Berry (PB) phase manipulation or geometrical phase control using spatially rotated anisotropic elements [84]. Transmission-type metasurfaces, such as those based on phase-shifting surfaces (PSS) or complementary coding metasurfaces, offer lower reflection loss and support dual-polarisation or dual-band OAM operation [88].

Recent advances include spin-decoupled metasurfaces capable of generating multiple coaxial OAM beams at Ku- and Ka-band by independently encoding the left-handed circular polarization (LHCP) and right-handed circular polarization (RHCP) components [50].

Advantage: enables real-time OAM mode reconfiguration with planar, low-profile integration; capable of supporting dual-band, dual-mode, and spin-dependent OAM generation.

Limitation: typically narrow instantaneous BW due to resonant unit cells; sensitive to fabrication and alignment tolerances; high-gain operation requires large aperture area.

Reference structure: a multilayer phase-shifting metasurface that integrates both spiral phase and lensing functionalities to generate and focus OAM beams at 60 GHz is demonstrated in [83], as shown in Fig. 1.13.

- **Dielectric Resonator Antenna (DRA) [91–93]**: A dielectric resonator antenna (DRA) utilizes a high-permittivity dielectric block that supports resonant electromagnetic modes with

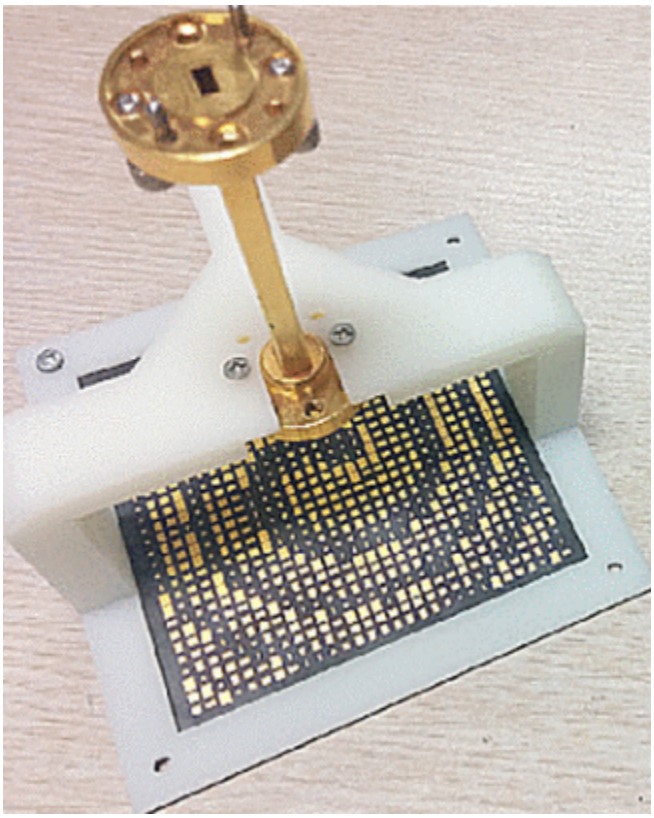

Figure 1.13: Fabricated flat-lensed SPP based on multilayer phase-shifting surface for generating focused OAM beam at 60 GHz [83].

azimuthal field components. By appropriately exciting higher-order modes (e.g., HE$mn\delta$ or TE$mn\delta$), the antenna can radiate beams exhibiting a helical phase profile of the form $e^{jl\phi}$, characteristic of orbital angular momentum (OAM) modes. Multimode and efficient OAM generation can be achieved through the use of cylindrical DRAs or other specially designed dielectric configurations.

Advantage: compact size, high radiation efficiency, and intrinsic support for higher-order OAM modes.

Limitation: narrow bandwidth and sensitivity to dielectric and feed geometry.

Reference structure: a representative cylindrical dielectric resonator supporting $l = 3$ and $l = 4$ OAM modes is shown in [93], as illustrated in Fig. 1.14.

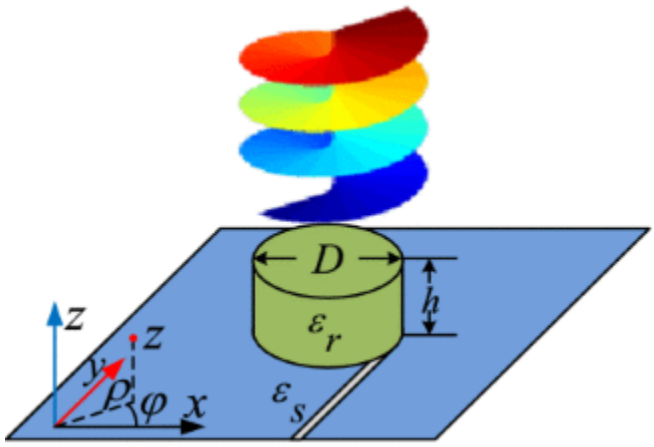

Figure 1.14: Cylindrical DRA for OAM generation [93].

1.3 Research Objectives, Innovations, and Thesis Structure

1.3.1 Research Objectives

This thesis focuses on the design, simulation, and experimental validation of a dual-band OAM antenna with mode-switching capability for integrated microwave and mm-wave wireless communication systems. The proposed antenna operates at both 5.8 and 28 GHz and employs a co-layer shared-aperture structure to achieve compact dual-band performance. Mode switching is realized through symmetric dual-port feeding, enabling conjugate OAM mode switching ($l = \pm 1$) without the need for additional phase-shifting circuits. The specific research tasks include:

- Analyzing the fundamental characteristics of OAM beams, including their physical properties, orthogonality, and generation mechanisms;
- Reviewing recent progress in multi-band OAM antenna designs and integration strategies;
- Proposing a novel dual-band co-layer UCA-based antenna design for simultaneous 5.8 and 28 GHz operation;
- Realizing mode-switchable OAM radiation using a symmetric dual-port feeding scheme without external phase-shifting circuits;
- Validating the antenna performance through full-wave simulations and experimental measurements, including S-parameters, near-field distributions, and far-field radiation patterns.

1.3.2 Key Innovations

The key contributions and innovations of this thesis are summarized as follows:

- **Co-layer dual-band shared-aperture OAM antenna structure:** The two UCAs for 5.8 and 28 GHz are implemented on the same plane, enabling compact integration and aperture reuse;
- **Conjugate OAM mode switching without external phase-shifting circuits:** A symmetric dual-port feeding mechanism is employed, which enables efficient switching between the $l = +1$ and $l = -1$ modes solely through port selection;
- **High port isolation ensuring independent operation:** The antenna design achieves inter-port isolation exceeding 30 dB, allowing for stable and interference-free dual-band OAM generation;
- **Complete end-to-end validation:** The full design cycle is completed, including theoretical analysis, simulation modeling, prototype fabrication, and experimental validation through S-parameter measurements, near-field scanning, and far-field radiation characterization.

1.3.3 Thesis Structure

To present the research content in a structured and logical manner, this thesis is organized as follows:

- **Chapter 1: Introduction.** Presents the background and motivation of the research, summarizes the state-of-the-art in OAM antennas, and outlines the research objectives and scope;
- **Chapter 2: Theoretical Background.** Discusses the fundamentals of OAM, mode orthogonality, UCA-based beam generation;
- **Chapter 3: Design and Performance Evaluation of the Proposed OAM Antenna.** Describes the antenna configuration, working mechanism, simulation results, and experimental validation; includes a performance comparison with reported frequency-tunable and dual-band OAM antennas to highlight the advantages of the proposed design;

- **Chapter 4: Conclusion and Future Work.** Summarizes the main contributions of this research and proposes potential directions for future study.

Chapter 2

Theoretical Background

2.1 Overview of Orbital Angular Momentum

In classical electromagnetic theory, electromagnetic waves not only carry linear momentum but also total angular momentum, which can be decomposed into spin angular momentum (SAM), associated with the polarization state, and OAM, related to the spatial structure of the wavefront [106,124,125].

The total angular momentum of the electromagnetic field is expressed as [126]:

$$\vec{J} = \int \varepsilon_0 \vec{r} \times \mathrm{Re}\left\{\vec{E} \times \vec{B}^*\right\} dV \tag{2.1}$$

This expression stems from the time-averaged Poynting vector and represents the total angular momentum density in the field. Here, ε_0 is the vacuum permittivity, $\vec{r}$ is the position vector, while $\vec{E}$ and $\vec{B}$ are the electric and magnetic field vectors, respectively. The total angular momentum can be divided into orbital and spin components using the Humblet decomposition [127]:

$$\vec{J} = \vec{L} + \vec{S} \tag{2.2}$$

In the context of classical electrodynamics, and based on a gauge-invariant field-theoretic formulation, the orbital and spin angular momentum densities can be expressed using the magnetic

vector potential $\vec{A}$ as follows:

$$\vec{L} = \varepsilon_0 \int \mathrm{Re}\left\{ j\vec{E}^*(\hat{\vec{L}} \cdot \vec{A}) \right\} dV \tag{2.3}$$

$$\vec{S} = \varepsilon_0 \int \mathrm{Re}\left\{ \vec{E}^* \times \vec{A} \right\} dV \tag{2.4}$$

where $\hat{\vec{L}} = -j(\vec{r} \times \nabla)$ is the OAM operator [128]. These expressions are derived from the canonical form of electromagnetic angular momentum and are particularly useful for analyzing structured optical fields and vortex beams in free space [106,125]. Equation (2.3) indicates that the OAM $\vec{L}$ is dependent on the spatial distribution of the field and is thus governed by the helical structure of the wavefront. The OAM mode is quantified by the topological charge l, which takes a negative value when the wavefront phase spirals counterclockwise and a positive value when it spirals clockwise. In contrast, Equation (2.4) reveals that the SAM $\vec{S}$ does not depend on the spatial distribution of the field and is instead determined by the polarization state of the wave, which originates purely from the field's intrinsic polarization property. The SAM mode is denoted by s, where linearly polarized waves correspond to $s = 0$, LHCP corresponds to $s = 1$, and RHCP corresponds to $s = -1$ [129,130].

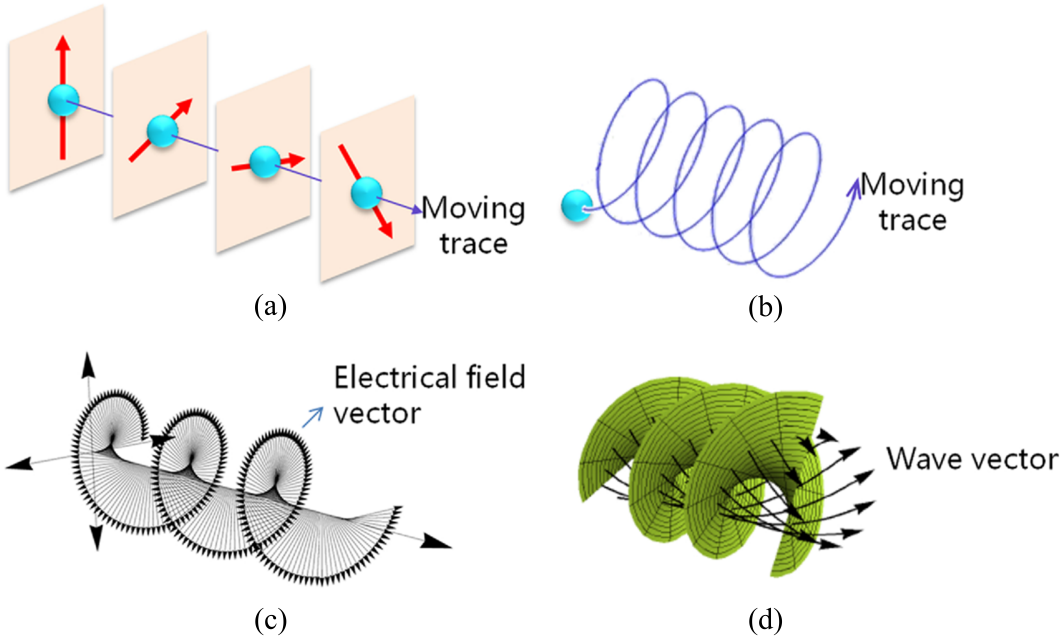

Figure 2.1: Conceptual illustrations of angular momentum: (a) A spinning object exhibiting SAM; (b) An orbiting object exhibiting OAM; (c) A circularly polarized beam carrying SAM via electric field rotation; (d) A helical wavefront structure representing OAM [107,131].

To further clarify the physical distinction between spin and orbital angular momentum, Fig. 2.1 presents conceptual illustrations [107, 131]: (a) a particle spinning about its own axis carries SAM, whereas (b) a particle orbiting around an external axis carries OAM. Analogously, (c) depicts a circularly polarized beam whose electric field vector rotates around the propagation axis—this is the electromagnetic manifestation of SAM. In contrast, (d) illustrates a helical wavefront associated with an OAM-carrying beam, where the spatial phase of the wave exhibits an azimuthally spiral phase profile around the beam axis. These helical wavefronts are mathematically described by a phase term of the form $\exp(-jl\phi)$, where ϕ denotes the azimuth angle and l is the topological charge of the mode [107, 130].

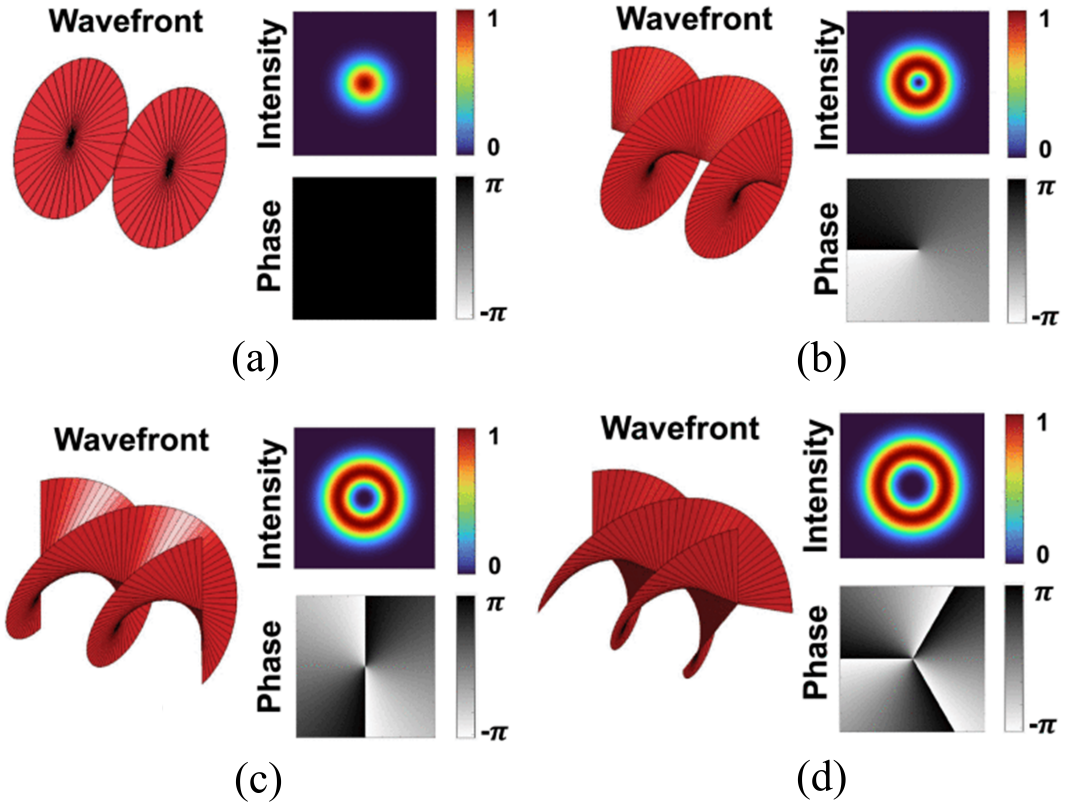

Figure 2.2: OAM beam wavefronts, intensity, and phase distributions for topological charges $l = 0, 1, 2, 3$: (a) $l = 0$; (b) $l = 1$; (c) $l = 2$; (d) $l = 3$ [132].

A more concrete illustration of the azimuthal phase dependence of OAM beams is provided in Fig. 2.2 [132], which presents the simulated wavefront shape, intensity distribution, and phase map for different OAM modes on a unified scale. As the topological charge l increases, the wavefront becomes more twisted and the intensity profile evolves from a Gaussian-like distribution to a ring-shaped pattern with a central null. Specifically:

(a) $l = 0$: planar wavefront, uniform phase, and Gaussian intensity profile.

(b) $l = 1$: one 2π azimuthal phase wrap; intensity forms a donut with a central null.

(c) $l = 2$: two 2π wraps; wider annular ring in intensity.

(d) $l = 3$: three 2π wraps; larger radius and phase vortex.

2.2 Mode Orthogonality of OAM Beams

A key advantage of OAM-carrying electromagnetic waves lies in the intrinsic orthogonality of different topological charges in the azimuthal domain. For a UCA, the complex electric field of the l-th OAM mode at cylindrical coordinates (ρ, ϕ, z) can be expressed as [80]:

$$E_l(\rho, \phi, z) = A_l(\rho, z)\, e^{-jl\phi}, \tag{2.5}$$

where $A_l(\rho, z)$ accounts for the field's amplitude envelope on the transverse plane, and the factor $\exp(-jl\phi)$ represents an l-fold helical phase term [80, 118, 126].

On a given transverse plane defined by ρ and z, any two modes l_1 and l_2 satisfy the orthogonality condition [80]:

$$\int_0^{2\pi} E_{l_1}(\rho, \phi, z)\, E_{l_2}^*(\rho, \phi, z)\, \mathrm{d}\phi = 0, \quad l_1 \neq l_2, \tag{2.6}$$

This implies that at the receiver side, each OAM mode can be treated as an independent communication channel, eliminating the need for complex digital equalization [80].

This intrinsic "physical orthogonality" contrasts with conventional line-of-sight (LOS)–MIMO techniques that rely on antenna spacing and matrix inversion for channel decoupling. As a result, OAM-based multiplexing provides natural interference suppression and significantly reduces receiver complexity [80].

2.3 UCA-Based Generation Mechanism of OAM Beams

Building upon the physical insights into spin and orbital angular momentum discussed in Section 2.1, this section presents the theoretical foundation for generating OAM beams using UCA.

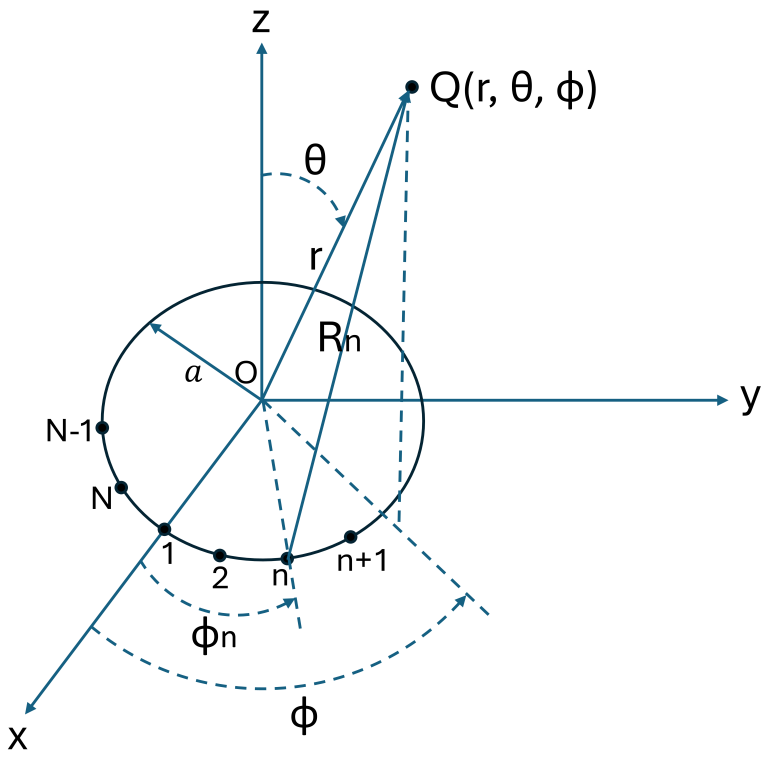

Figure 2.3: Geometry of a N-element uniform circular array.

Such configurations are widely adopted in antenna design due to their rotational symmetry, analytical tractability, and capability of providing discrete azimuthal phase control, thereby forming the basis for the operating principle of the proposed antenna.

Consider an ideal UCA composed of N isotropic radiating elements uniformly distributed along a circular ring of radius a in the xy-plane, as depicted in Fig. 2.3. The angular position of the n-th element is defined as:

$$\phi_n = \frac{2\pi(n-1)}{N}, \quad n = 1, 2, \ldots, N \tag{2.7}$$

An observation point $Q(r, \theta, \phi)$ is defined in the far-field region using spherical coordinates. The position vectors of the n-th array element and the observation point are $\vec{r}_n$ and $\vec{r}$, respectively. The vector pointing from the n-th element to point Q is then:

$$\vec{R}_n = \vec{r} - \vec{r}_n \tag{2.8}$$

Assuming far-field conditions ($r \gg a$), the distance R_n can be approximated using the first-order Taylor expansion:

$$R_n \approx r - a \sin\theta \cos(\phi - \phi_n) \tag{2.9}$$

The excitation current applied to each element is expressed in phasor form as [133]:

$$I_n = I e^{j[\phi_0 + (n-1)\Delta\phi]} \tag{2.10}$$

where $\Delta\phi = \frac{2\pi l}{N}$ represents the progressive phase shift between elements, l denotes the OAM mode index (also known as topological charge), ϕ_0 is the initial phase offset, and I is the constant current amplitude. In practical UCA systems, the achievable range of OAM modes is limited by the number of elements, with $|l| < N/2$ [118, 126].

The total far-field electric field $\vec{E}$ at point Q is then the superposition of the radiated fields from all N elements [134]:

$$\vec{E} = \sum_{n=1}^{N} I_n \frac{e^{-jkR_n}}{R_n} \hat{a}_r \tag{2.11}$$

where $\hat{a}_r$ is the unit vector in the radial direction.

Substituting R_n and I_n into the expression and applying the far-field approximation yields:

$$\vec{E} \approx \frac{I e^{-jkr}}{r} \sum_{n=1}^{N} e^{j[ka\sin\theta\cos(\phi-\phi_n)+\phi_0+(n-1)\Delta\phi]} \hat{a}_r \tag{2.12}$$

This formulation reveals that the resulting radiation exhibits a helical phase front in the azimuthal direction, a defining characteristic of OAM beams. Specifically, the total phase shift along the UCA circumference is $2\pi l$, and the progressive phase shift between elements is $\Delta\phi$.

The sign of l denotes the handedness of the helical phase: a clockwise azimuthal rotation corresponds to a positive l, while a counterclockwise rotation corresponds to a negative l. This spatial phase variation leads to the well-known doughnut-shaped intensity profile and the phase singularity at the beam center, both typical features of OAM modes [129, 130, 132].

2.3.1 Conjugate Mode Realization via Symmetric Dual-Port Feeding

To further enhance practical implementability, this work adopts a symmetric dual-port feeding architecture that enables mode-switching between $l = +1$ and $l = -1$ without the need for bulky external phase-shifting networks.

Setting $\phi_0 = 0$ in Equation (2.10), the excitation current simplifies to:

$$I_n^{(l)} = I_0 e^{j(n-1)\Delta\phi}, \tag{2.13}$$

where I_0 denotes the constant current amplitude.

For $l = +1$ and $l = -1$, the excitation currents satisfy:

$$I_n^{(-1)} = \left(I_n^{(+1)}\right)^* \tag{2.14}$$

This complex conjugate relationship permits OAM mode switching via feeding symmetry: by selectively exciting one port and terminating the other with a matched load, conjugate OAM modes can be generated without the need for additional phase-shifting circuits. This approach significantly simplifies system complexity while ensuring stable and mode-switchable OAM beam generation across dual frequency bands.

2.4 Summary

This chapter established the theoretical background essential for understanding the design and operation of OAM-based antenna systems. Section 2.1 reviewed the physical origin of angular momentum in electromagnetic waves, distinguishing between SAM, which is related to polarization, and OAM, which arises from the helical structure of the wavefront. Conceptual diagrams and simulated field distributions were used to illustrate the unique characteristics of OAM beams, such as helical phase wavefront and ring-shaped intensity profiles. Section 2.2 discussed the intrinsic orthogonality of OAM modes in the azimuthal domain, which enables spatial multiplexing without requiring complex digital equalization. This property offers significant advantages for high-capacity wireless communications. Section 2.3 presented the generation mechanism of OAM beams using a

UCA, supported by analytical formulations under the far-field approximation. A symmetric dual-port feeding strategy was also introduced to enable mode switching between $l = +1$ and $l = -1$ without additional phase-shifting circuits. These theoretical foundations lay the groundwork for the proposed antenna design presented in the next chapter, which introduces a dual-band, mode-switchable OAM antenna operating simultaneously at microwave and mm-wave frequencies, along with its configuration, operating mechanism, and both simulation and experimental validation.

Chapter 3

Design and Performance Evaluation of the Proposed OAM Antenna

With the increasing demand for high-speed and high-capacity wireless communication systems, OAM has emerged as a promising multiplexing technique. Due to the intrinsic orthogonality of different OAM modes in the azimuthal domain, multiple data streams can be transmitted simultaneously over the same frequency channel, thereby enabling MDM to enhance spectral efficiency without additional bandwidth consumption [40–44].

In recent years, various OAM antennas based on UCAs have been proposed to generate OAM beams in the microwave band. Several designs have demonstrated frequency-tunable, broadband, or dual-band performance [65, 67, 68, 135, 136]. Although these works represent important progress in reconfigurable or mode-switchable OAM generation, they are typically confined to sub-6 GHz operation and rely on multilayer structures or complex feeding networks, such as probe- or post-loaded stacked patches, varactor-tuned SIW cavities, power-divider networks, phase-shifting circuits, and wideband branch-line couplers. These features significantly increase system complexity, insertion loss, and fabrication challenges—especially when scaling to mm-wave frequencies. Moreover, in next-generation wireless systems such as 5G and beyond, the simultaneous utilization of microwave and mm-wave spectra is essential to balance coverage and capacity demands [1,2,9]. Microwave band (e.g., 5.8 GHz) offer superior propagation and penetration characteristics for long-range communication, owing to their lower free-space path loss and established deployment infrastructure [1,3]. In

contrast, mm-wave band (e.g., 28 GHz) provide abundant spectrum resources and ultra-high data throughput suitable for dense urban environments, but suffer from high propagation losses and limited coverage range [9–11]. Therefore, developing compact and mode-switchable OAM antennas capable of dual-band operation is crucial for enabling unified access across diverse deployment scenarios and supporting spectrum-efficient, multi-service wireless platforms [15, 16].

To address these challenges, this chapter presents the design and performance evaluation of a single-layer, dual-band, mode-switchable OAM antenna capable of operating at both 5.8 and 28 GHz. The proposed design achieves OAM mode switching ($l = \pm 1$) through a symmetric dual-port feeding strategy, which eliminates the need for external phase-shifting networks and enables compact, low-profile integration. The proposed design utilizes a UCA configuration optimized for supporting helical phase wavefronts at both 5.8 and 28 GHz. To assess its performance, full-wave simulations and experimental measurements are performed, focusing on key metrics such as impedance matching, port isolation, near-field phase and amplitude distributions, and far-field radiation patterns.

3.1 Antenna Design Requirements and Specification

The development of the proposed dual-band, mode-switchable OAM antenna is driven by the growing need for high-capacity wireless systems that can support both microwave and mm-wave bands simultaneously. Specifically, this antenna is intended to operate efficiently at 5.8 and 28 GHz, enabling flexible deployment across different coverage and capacity scenarios. The antenna is designed to support OAM modes switching between $l = +1$ and $l = -1$ through a compact, single-layer structure without relying on external phase-shifting networks. This approach significantly reduces system complexity and facilitates integration into practical platforms.

3.1.1 Target Performance Requirements

To satisfy the requirements for next-generation wireless communication systems, the proposed antenna design aims to achieve the following performance specifications:

- **Dual-band operation:** Reliable performance at 5.8 GHz (microwave) and 28 GHz (mm-wave) to support heterogeneous wireless networks.
- **OAM mode-switchable:** Generation of conjugate OAM modes ($l = +1$ and $l = -1$) using a symmetric dual-port excitation scheme.
- **Compact single-layer structure:** Low-profile and easily manufacturable design that eliminates the need for multilayer configurations.
- **Good impedance matching:** Reflection coefficients below -10 dB at both frequency bands.
- **High port isolation:** Isolation better than -30 dB between different UCA feeding ports to minimize mutual coupling and preserve independent excitation.
- **Generation of OAM modes:** Near-field and far-field results demonstrating the generation of helical phase fronts with clear phase singularities.

3.1.2 Design Challenges and Considerations

The primary challenge in realizing the above specifications lies in achieving consistent OAM characteristics across two widely separated frequency bands within a single, shared-aperture layout. Conventional dual-band, multi-band, or wideband UCA-based OAM antennas are typically constrained to sub-6 GHz operation. These designs often rely on complex feeding networks—such as multi-branch power dividers, phase-shifting circuits, or hybrid couplers—which become difficult to scale efficiently to mm-wave frequencies due to increased insertion loss, fabrication tolerance sensitivity, and signal integrity degradation.

In contrast, the proposed antenna adopts a co-planar, single-layer architecture where the microwave and mm-wave sub-arrays share the same physical aperture while operating independently at 5.8 and 28 GHz. A series-fed scheme is employed to meet the phase progression required for OAM beam generation, while a symmetric dual-port feeding configuration enables mode switching between $l = +1$ and $l = -1$. This approach significantly simplifies the antenna structure, reduces feeding complexity, and facilitates frequency scaling based on the intrinsic relationship between antenna size and operating wavelength—thereby allowing straightforward extension to the mm-wave regime.

Additionally, the antenna must maintain structural symmetry to ensure balanced phase excitation across ports for consistent mode switching. This imposes strict requirements on array geometry, port placement, and transmission line layout. The proposed design addresses these challenges through precise geometric optimization and improved port-to-port isolation, while the layout and spacing of transmission lines are carefully designed to minimize parasitic coupling and maintain broadband performance integrity.

3.2 Antenna Configuration and Working Mechanism

This section presents the structural layout, geometric parameters, and working principles of the proposed dual-band, mode-switchable OAM antenna. A shared-aperture, single-layer configuration is employed to support efficient operation at 5.8 and 28 GHz, targeting mode-switchable OAM generation with minimal hardware complexity. The design consists of two concentric UCAs, each optimized for its respective frequency band.

3.2.1 Antenna Geometry and Layer Description

The overall structure is fabricated on a single Rogers RO4350B substrate with a thickness of 0.508 mm. Two key views of the antenna layout are illustrated in Fig.3.1:

- **Top view:** Shows the outer UCA array (5.8 GHz) and the inner UCA array (28 GHz), with respective feeding networks and radiating elements.
- **Bottom view:** Illustrates the integrated ground plane and the four feeding ports located symmetrically beneath the antenna, enabling independent excitation of the dual-band UCAs and ensuring effective isolation and structural integrity.

As shown in Fig. 3.1, the ports are distributed in a symmetric layout to support mode-switchable excitation.

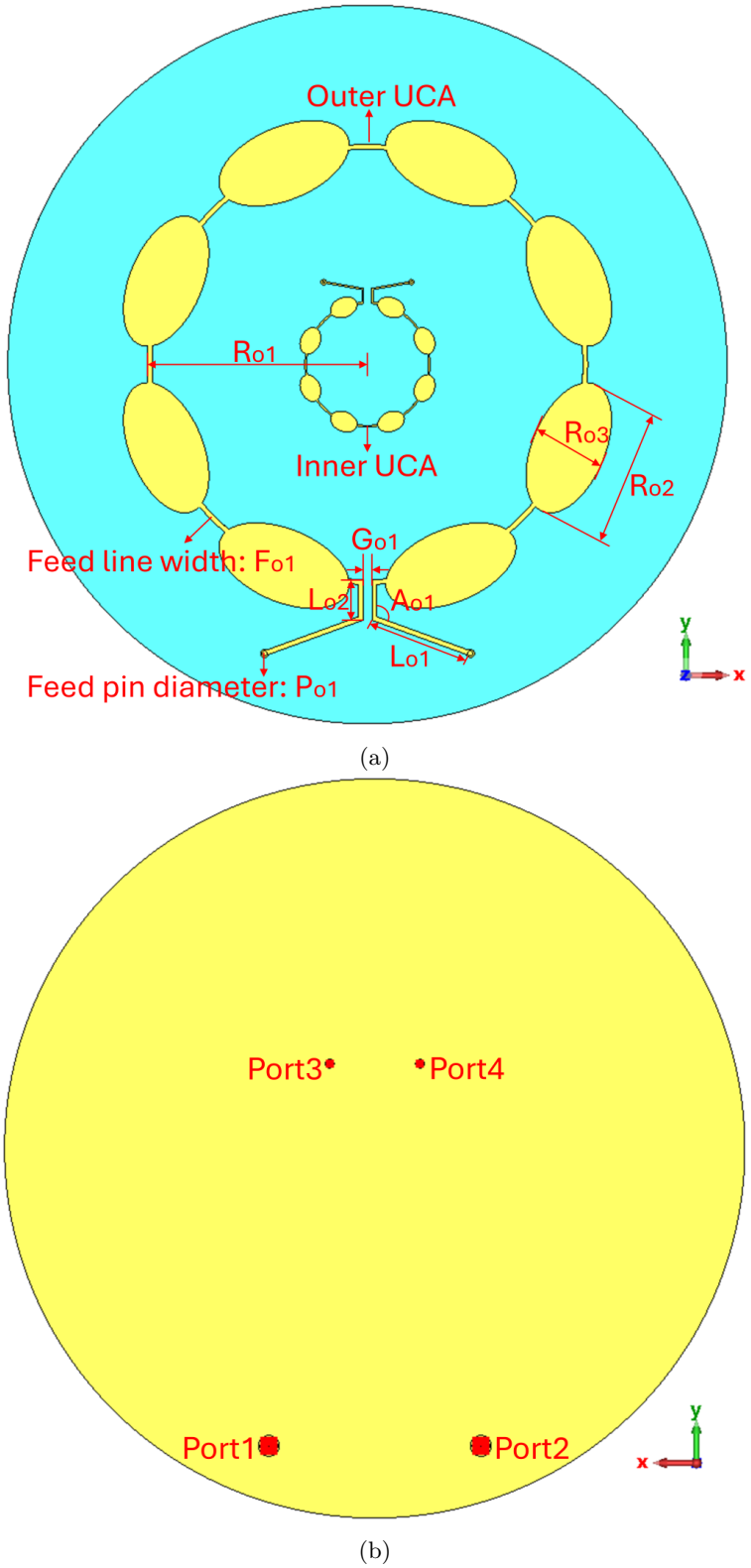

Figure 3.1: Antenna layout: (a) Top view showing dual UCA rings; (b) Bottom view with four feeding ports.

3.2.2 UCA Element Layout and Phase Feeding Principle

Each UCA consists of 8 equally spaced elements arranged on a circular ring. The outer UCA, operating at 5.8 GHz, has a larger radius and uses elliptical microstrip patches as radiators. The inner UCA, designed for 28 GHz, adopts miniaturized elliptical patches. Elliptical patches are chosen for their smooth impedance performance and better axial symmetry, which help to maintain mode purity in the azimuthal domain.

Both UCAs employ a series-fed network that ensures a progressive phase shift among adjacent elements, which is essential for generating OAM beams with topological charge l. According to the theoretical analysis in Chapter 2, the excitation phase difference between adjacent elements is given by:

$$\Delta\phi = \frac{2\pi l}{N}, \tag{3.1}$$

where l is the OAM mode index and $N = 8$ is the total number of elements in the UCA.

For the intended mode-switchable operation with $l = \pm 1$, this results in a phase shift of $\Delta\phi = \pm 45^\circ$ between neighboring elements. This phase progression ensures that the cumulative phase change along the ring is $2\pi l$, thereby forming the helical wavefront characteristic of OAM beams.

To physically align with the progressive phase structure, each elliptical patch is rotated by 45° relative to its neighbors, tangentially oriented along the circular array. This rotation scheme enhances the consistency between the geometric layout and the desired current phase, supporting symmetrical radiation and stable OAM mode generation. The rotation and phase progression strategy is illustrated in Fig. 3.2.

A symmetric dual-port configuration is implemented for each band. For a given UCA, exciting one port while terminating the other with a matched load enables the generation of conjugate OAM modes ($l = \pm 1$). This dual-port feeding corresponds to the conjugate current distributions discussed in Section 2.3, eliminating the need for external phase-shifting circuits.

3.2.3 Geometric Parameters of the Proposed Antenna

Building upon the structural principles introduced in the previous subsection, this section summarizes the detailed physical dimensions and material configuration of the proposed antenna.

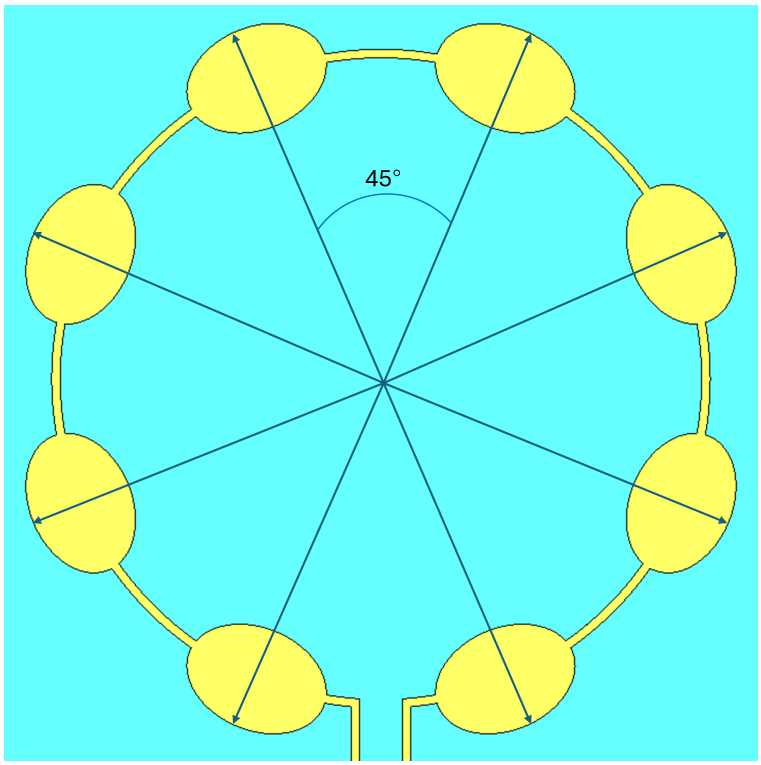

Figure 3.2: Patch rotation layout illustrating 45° inter-element alignment for $l = \pm 1$.

The design is implemented on a Rogers RO4350B substrate, selected for its low-loss characteristics ($\varepsilon_r = 3.48$, thickness 0.508 mm, loss tangent 0.0037), ensuring stable performance across both the microwave and mm-wave bands. The total circular substrate has an outer radius of 88.8 mm, within which two concentric UCAs are integrated.

Each UCA consists of 8 elliptical patch elements, consistent with the $N = 8$ configuration required to support OAM modes $l = \pm 1$. As established in Chapter 2, this corresponds to a progressive excitation phase shift of 45° between adjacent elements. The physical orientation of each patch is also rotated by 45° to align with the tangential phase distribution, as described in Section 3.2.2.

The inner UCA targets 28 GHz and uses compact elliptical patches arranged within the inner region of the substrate. The outer UCA operates at 5.8 GHz and occupies the remaining aperture, achieving frequency and spatial separation while maintaining aperture sharing.

Fig. 3.1 provides visual context for the structural components listed in Table 3.1, including patch placement, feedline routing, and aperture dimensions for both the inner and outer UCAs. Table 3.1 summarizes the key geometric parameters, where subscripts 'i' and 'o' denote the inner

Table 3.1: Geometric Parameters of the Proposed Antenna (Unit: mm)

Parameter	R_{o1}	F_{o1}	P_{o1}	L_{o2}	G_{o1}	A_{o1}	L_{o1}	R_{o3}	R_{o2}
Value	27.2	0.6	0.63	5	1.1	110°	12.63	9	17
Parameter	R_{i1}	F_{i1}	P_{i1}	L_{i2}	G_{i1}	A_{i1}	L_{i1}	R_{i3}	R_{i2}
Value	7.73	0.2	0.3	1.9	1	100°	4.79	2.4	3.4

Note: R_{o3} and R_{o2} represent the minor and major diameters of the elliptical element in the outer UCA, respectively.

and outer UCAs, respectively. The listed values are each carefully optimized through full-wave simulations in CST Microwave Studio to ensure good impedance matching, minimal coupling, and reliable generation of OAM modes.

3.3 Simulation and Experimental Validation

This section validates the performance of the proposed dual-band, mode-switchable OAM antenna through full-wave electromagnetic simulations and experimental measurements. Both 5.8 and 28 GHz operating bands are analyzed in terms of reflection and transmission characteristics, near-field phase and amplitude distributions, and far-field radiation patterns.

The antenna prototype was fabricated using printed circuit board (PCB) technology. A vector network analyzer (VNA) was employed to measure S-parameters, which were then used to evaluate impedance matching and port isolation. Near-field measurements were conducted in a microwave anechoic chamber to capture the electric field's amplitude and phase distributions at a fixed distance from the antenna aperture. Far-field measurements were also performed under the same chamber conditions to obtain the radiation patterns associated with different excitation ports. Simulation results were obtained using CST Microwave Studio, and measurement data were post-processed with Origin to enable visual comparison. The results confirm the antenna's ability to generate OAM beams with switchable topological charges ($l = \pm 1$) at both frequency bands.

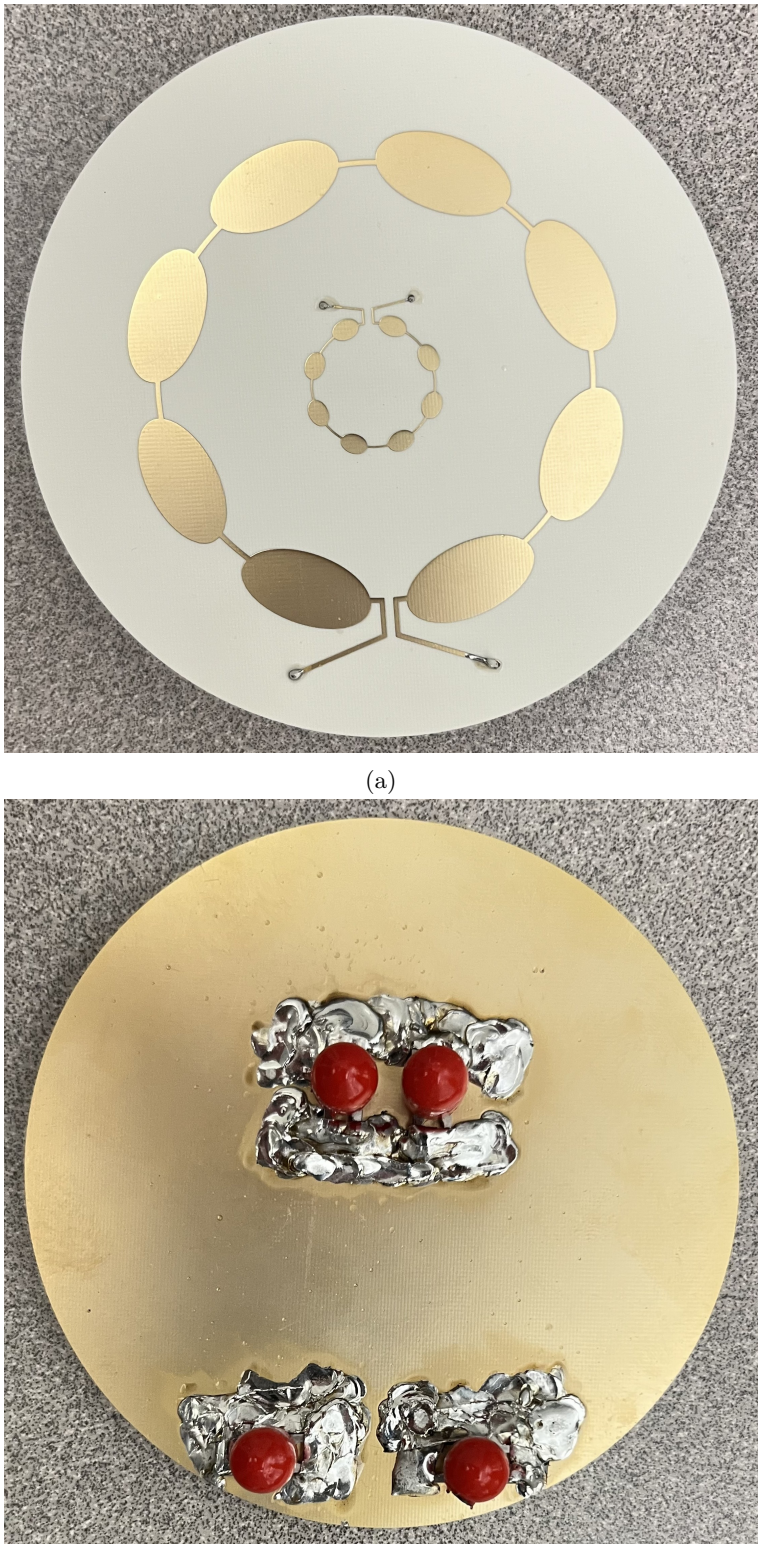

(a)

(b)

Figure 3.3: Fabricated prototype of the proposed dual-band mode-switchable OAM antenna: (a) Top view; (b) Bottom view.

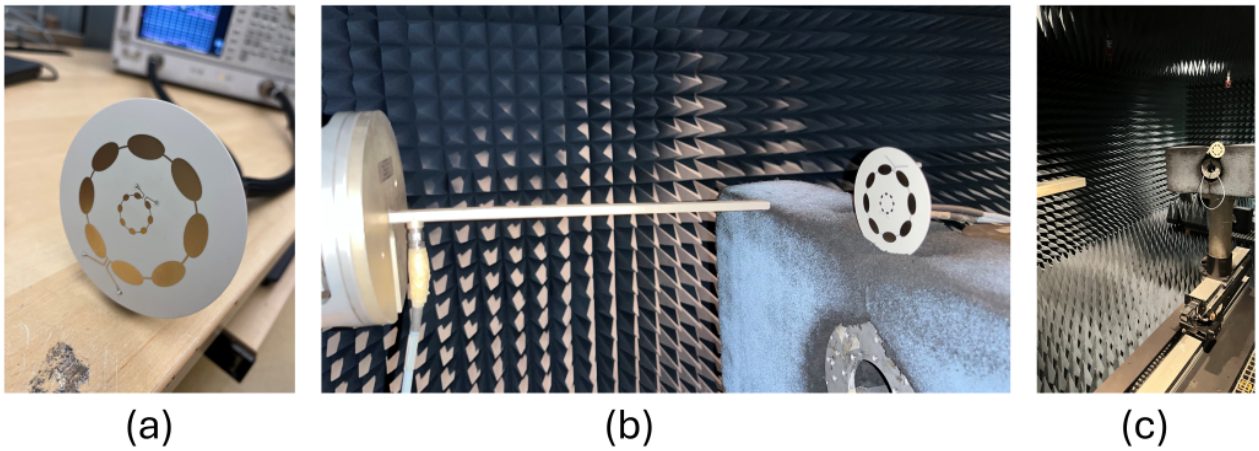

Figure 3.4: Measurement setups: (a) S-parameter testing with VNA; (b) Near-field scanning; (c) Far-field radiation pattern acquisition.

3.3.1 Fabricated Prototype

The fabricated prototype of the dual-band mode-switchable OAM antenna is shown in Fig. 3.3. The top view highlights the co-planar elliptical patch layout and feed networks, while the bottom view shows the integration of four SMA connectors, enabling symmetric dual-port excitation at both 5.8 and 28 GHz. All patches and feedlines were realized using standard PCB etching techniques.

3.3.2 Measurement Setup

A comprehensive set of measurements was conducted to validate the simulated performance. As illustrated in Fig. 3.4, the measurement procedures include:

- **S-parameter characterization:** Conducted using a VNA, with the antenna connected through calibrated cables. Reflection and transmission coefficients were recorded for all ports to verify impedance matching and port isolation.
- **Near-field scanning:** Performed in a microwave anechoic chamber using a 3D near-field probe scanner. The y-component of the electric field was measured on a transverse plane ($z =$ 60 mm) to evaluate OAM mode generation through spiral phase distributions and doughnut-shaped amplitude profiles.

- **Far-field measurements:** Carried out in the same chamber using a standard gain horn and a motorized turntable. Azimuthal radiation patterns were measured to identify the far-field null.

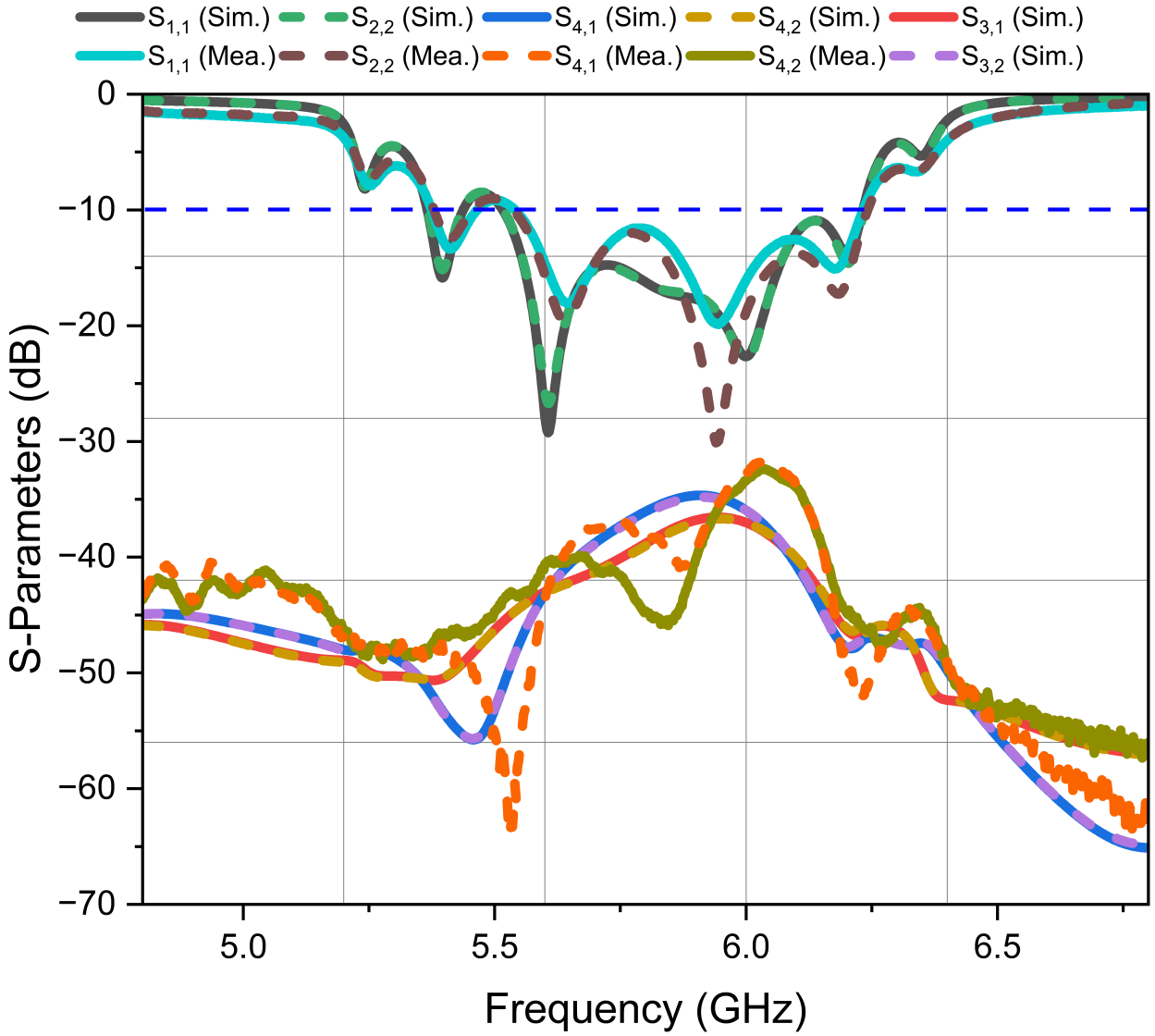

Figure 3.5: Simulated and measured S-parameters of the proposed antenna at 5.8 GHz

3.3.3 S-Parameter Validation

To evaluate the impedance matching and inter-port isolation of the proposed antenna, the simulated and measured S-parameters at both operating frequencies are presented in Figs. 3.5 and 3.6. These

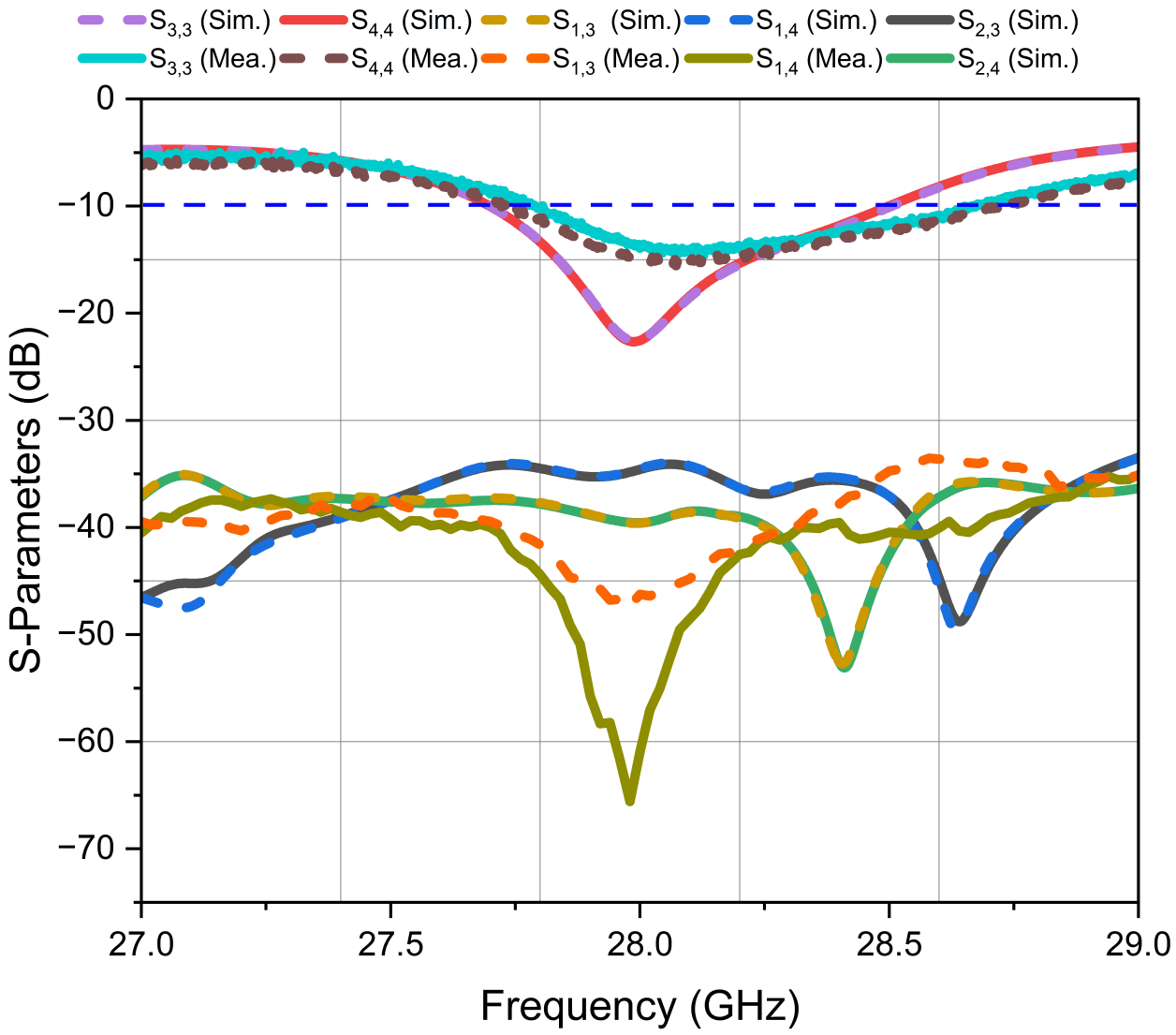

Figure 3.6: Simulated and measured S-parameters of the proposed antenna at 28 GHz

results verify the antenna's ability to achieve effective impedance matching and strong isolation across the 5.8 and 28 GHz bands.

At the microwave band (5.8 GHz), the reflection coefficients ($S_{1,1}$, $S_{2,2}$) are below −10 dB over the ranges of 5.52–6.24 GHz (simulated) and 5.54–6.24 GHz (measured), indicating good impedance matching. The corresponding transmission coefficients ($S_{4,1}$, $S_{3,2}$, $S_{3,1}$, $S_{4,2}$) are all below −30 dB, confirming excellent isolation between the microwave and mm-wave sub-arrays.

Similarly, at 28 GHz, the reflection coefficients ($S_{3,3}$, $S_{4,4}$) remain below −10 dB over 27.71–28.48 GHz (simulated) and 27.79–28.64 GHz (measured). The transmission coefficients ($S_{1,4}$, $S_{2,3}$,

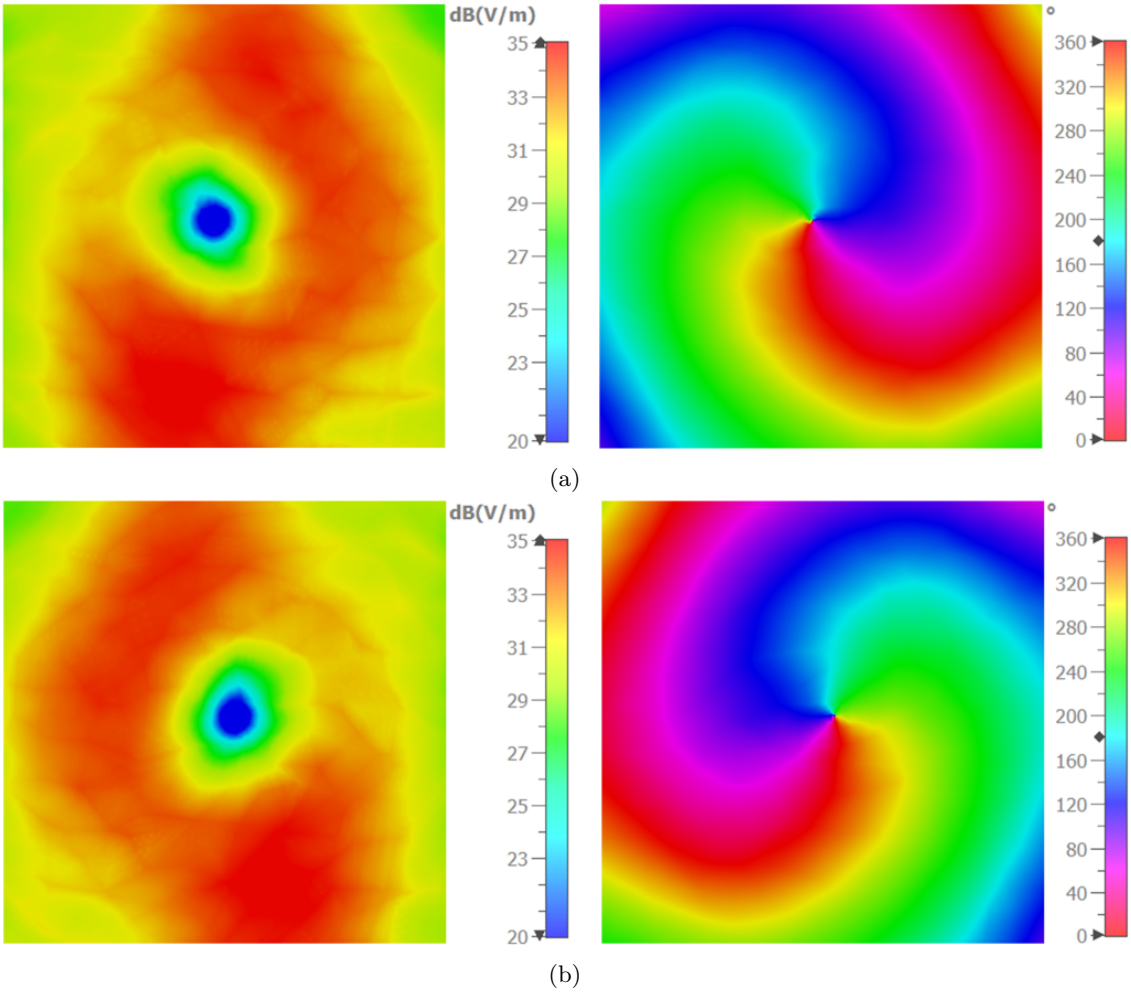

Figure 3.7: Simulated amplitude and phase distributions of the y-component in the plane at $z = 60$ mm from the antenna surface at 5.8 GHz: (a) Port 1 excitation (OAM mode $l = -1$); (b) Port 2 excitation (OAM mode $l = +1$).

$S_{1,3}$, $S_{2,4}$) also remain below -30 dB, confirming strong port-to-port isolation and minimal coupling between dual-band UCA layers.

Thanks to the x-axis symmetry in the antenna's dual-port layout, the transmission coefficients satisfy: $S_{4,1} = S_{3,2}$, $S_{3,1} = S_{4,2}$, $S_{1,3} = S_{2,4}$, and $S_{1,4} = S_{2,3}$. For brevity, only representative transmission coefficients are shown in the figures.

Minor discrepancies between simulation and measurement can be attributed to fabrication tolerance, soldering uncertainty, and measurement setup imperfections. Nevertheless, the results confirm stable dual-band impedance matching and high isolation essential for independent OAM mode operation at both frequency bands.

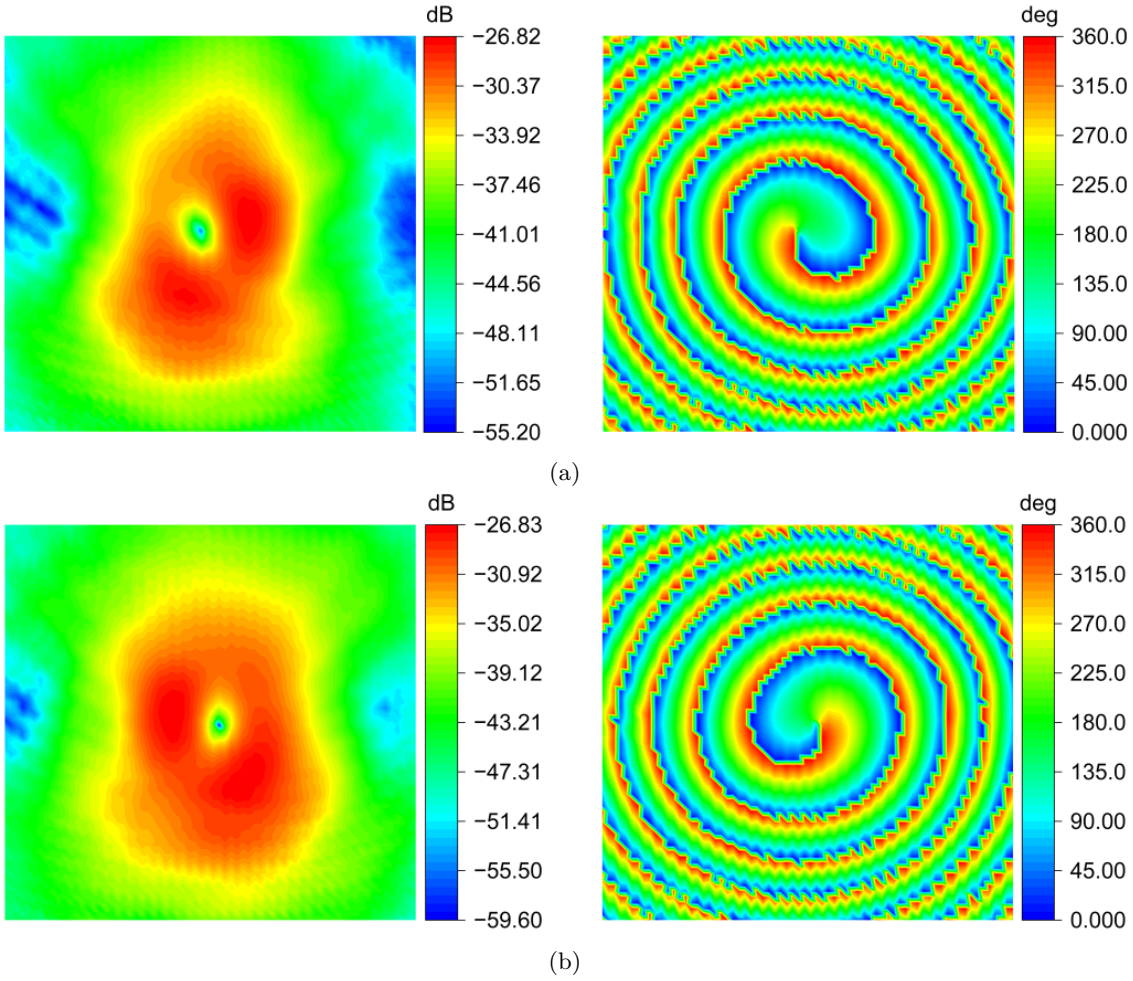

Figure 3.8: Measured amplitude and phase distributions of the y-component in the plane at $z = 60$ mm from the antenna surface at 5.8 GHz: (a) Port 1 excitation (OAM mode $l = -1$); (b) Port 2 excitation (OAM mode $l = +1$).

3.3.4 Near-Field Phase and Amplitude Verification

To confirm the generation of OAM modes, both simulated and measured near-field distributions of the y-component of the electric field were analyzed at $z = 60$ mm above the antenna surface. Figs. 3.7–3.10 present the amplitude and phase patterns at 5.8 and 28 GHz, demonstrating the antenna's ability to excite conjugate OAM modes ($l = \pm 1$) at both frequency bands.

At 5.8 GHz, Fig. 3.7 shows the simulated field distributions. Excitation of Port 1 yields an OAM mode of $l = -1$, while Port 2 excitation generates $l = +1$. The corresponding measured results are shown in Fig. 3.8, where the phase plots reveal spiral wavefronts, and the amplitude

distributions exhibit clear doughnut-shaped profiles with central nulls—consistent with typical OAM beam behavior.

At 28 GHz, Fig. 3.9 illustrates the simulated near-field results. Port 3 and Port 4 excitations yield OAM modes of $l = +1$ and $l = -1$, respectively. These patterns are experimentally validated in Fig. 3.10, with strong agreement in both amplitude rings and phase helicity. The minor deviations observed between simulation and measurement can be attributed to practical factors such as probe alignment error, fabrication imperfections, and environmental reflections during testing.

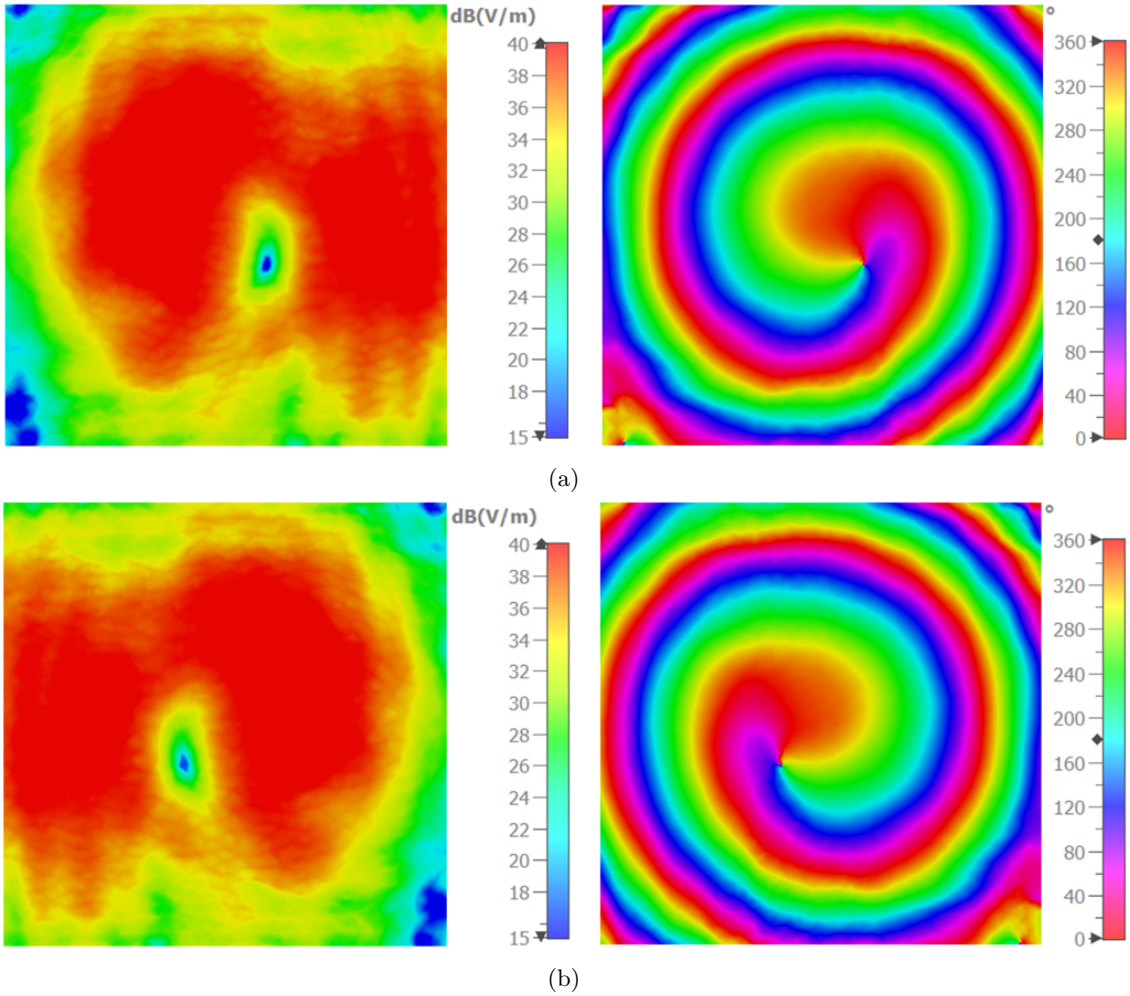

Figure 3.9: Simulated amplitude and phase distributions of the y-component in the plane at $z = 60$ mm from the antenna surface at 28 GHz: (a) Port 3 excitation (OAM mode $l = +1$); (b) Port 4 excitation (OAM mode $l = -1$).

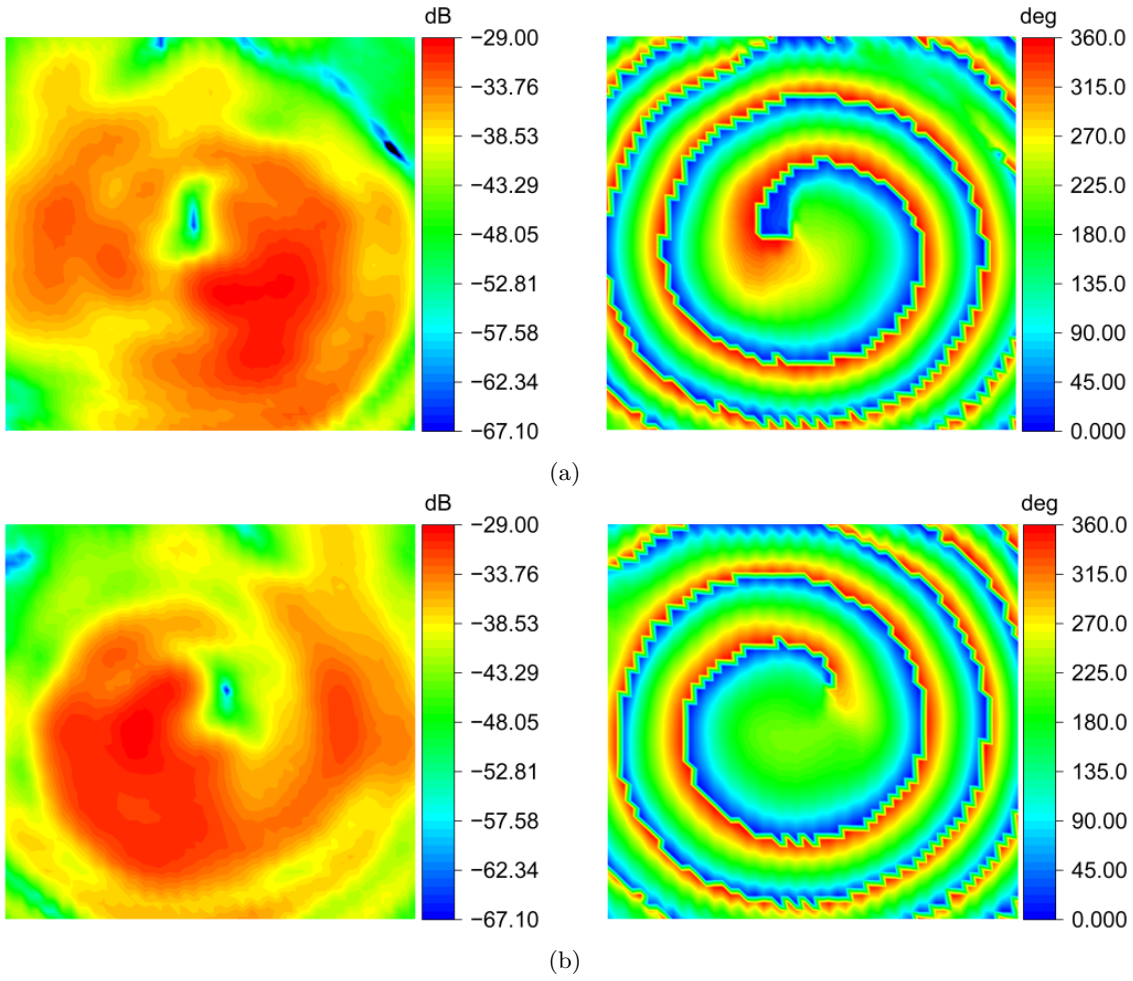

Figure 3.10: Measured amplitude and phase distributions of the y-component in the plane at $z = 60$ mm from the antenna surface at 28 GHz: (a) Port 3 excitation (OAM mode $l = +1$); (b) Port 4 excitation (OAM mode $l = -1$).

3.3.5 Far-Field Radiation Patterns

To further validate the far-field OAM radiation, normalized gain patterns at 5.8 and 28 GHz were obtained through full-wave simulations and anechoic chamber measurements. Figs. 3.11 and 3.12 illustrate the radiation profiles under different port excitations at the two operating frequencies, each corresponding to OAM modes $l = \pm 1$.

At 5.8 GHz, Fig. 3.11 presents the simulated and measured gain radiation patterns. When Port 1 is excited, the antenna generates an OAM beam with $l = -1$ (Fig. 3.11a), while Port 2 excitation yields the $l = +1$ mode (Fig. 3.11b). In both cases, boresight nulls—indicative of phase singularities—are clearly observed, and the radiation lobes are symmetrically distributed. The

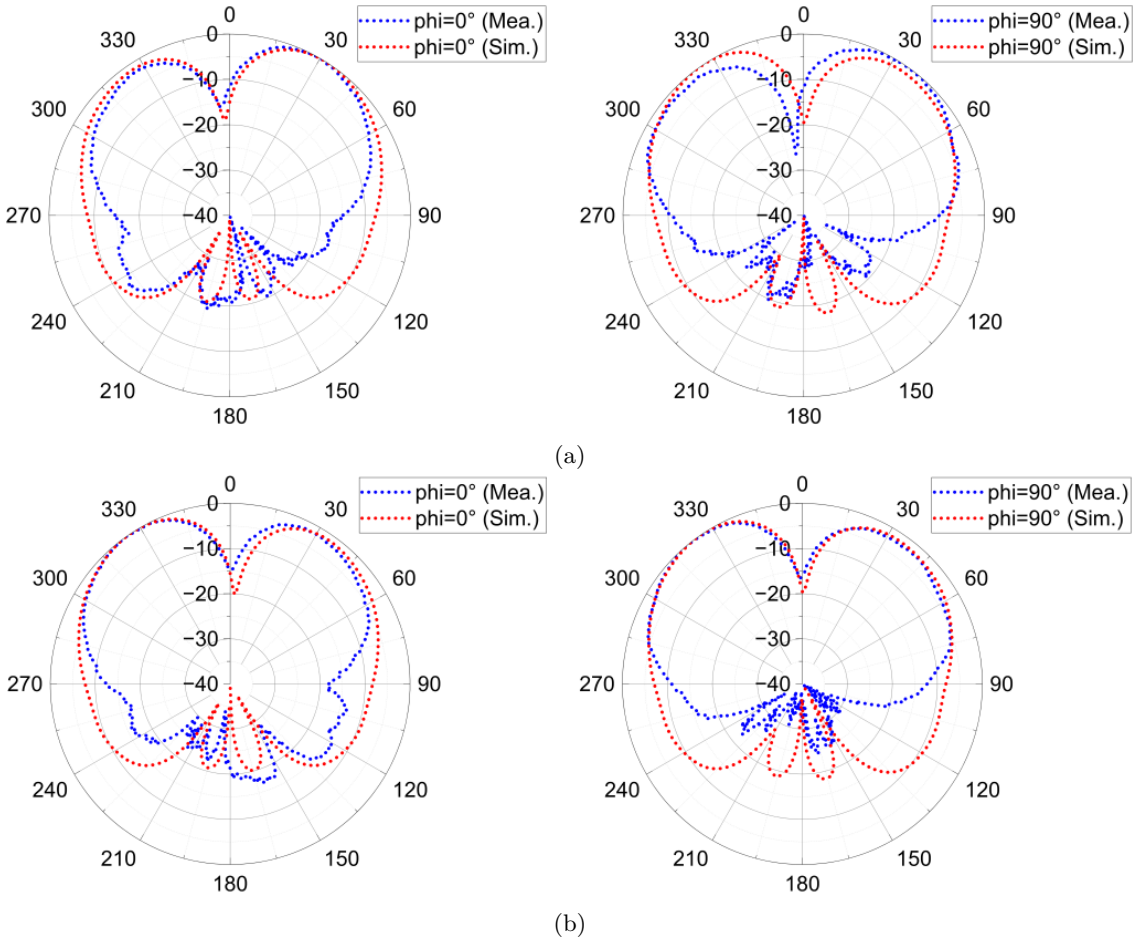

Figure 3.11: Simulated and measured normalized gain radiation patterns at 5.8 GHz: (a) Port 1 excitation ($l = -1$); (b) Port 2 excitation ($l = +1$).

agreement between simulation and measurement confirms the antenna's mode-switchable OAM capability in the microwave band.

At 28 GHz, the far-field patterns shown in Fig. 3.12 further demonstrate successful OAM mode generation at millimeter-wave frequencies. Port 3 and Port 4 correspond to $l = +1$ and $l = -1$, respectively. As with the lower band, the main lobes remain symmetric and well-defined, and a pronounced null along the axis is evident in both measurement and simulation.

Minor discrepancies between simulation and measurement—such as slight variations in side lobe levels or beam tilt—can be attributed to fabrication tolerances, measurement uncertainties, and environmental reflections in the chamber. Nonetheless, the results consistently demonstrate the proposed antenna's capability to radiate mode-switchable OAM beams across dual frequency bands.

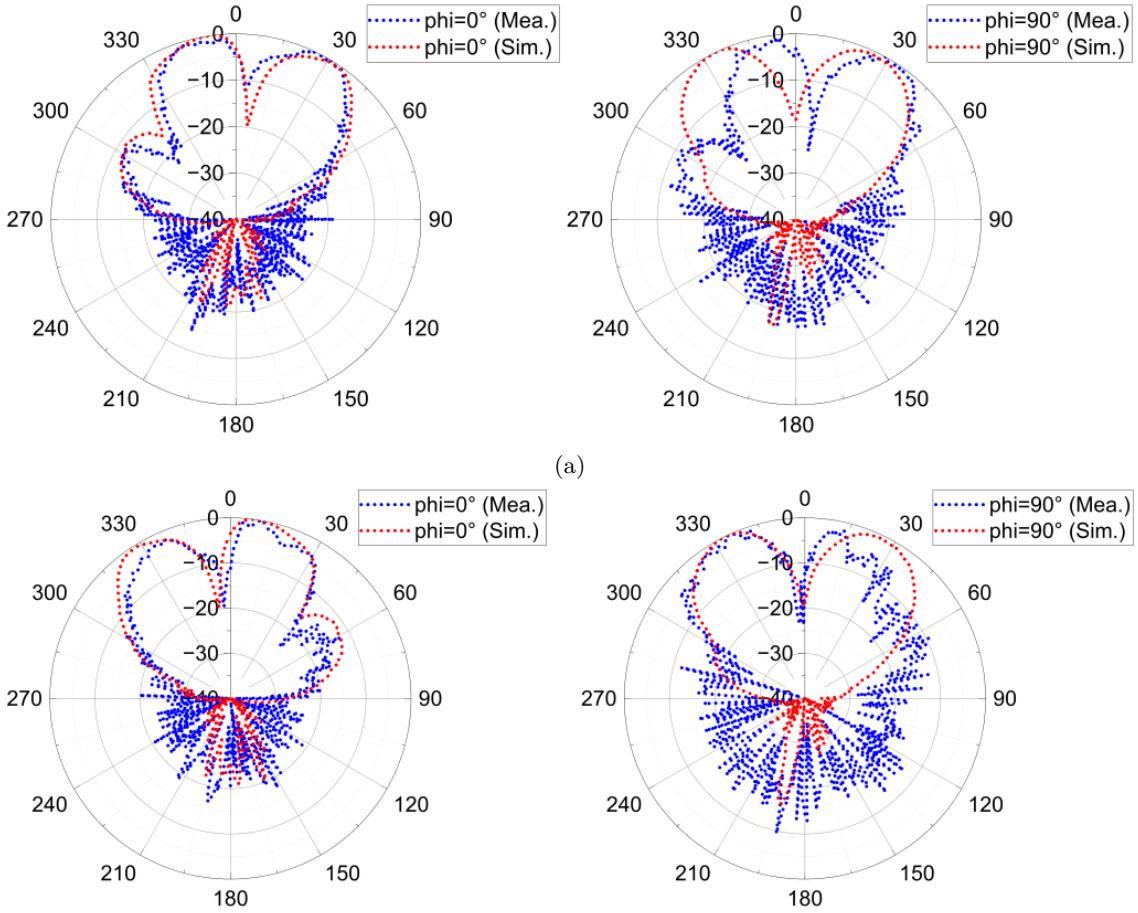

Figure 3.12: Simulated and measured normalized gain radiation patterns at 28 GHz: (a) Port 3 excitation ($l = +1$); (b) Port 4 excitation ($l = -1$).

3.4 Performance Comparison

Table 3.2 compares the proposed antenna with representative frequency-tunable and dual-band OAM antennas reported in the literature. Three salient advantages are observed:

- **True microwave and mm-wave integration:** Only the present work supports simultaneous operation at 5.8 and 28 GHz, whereas the cited designs remain confined to the sub-6 GHz band.
- **Compact single-layer hardware:** The prototype occupies merely $88.8 \times 88.8 \times 0.508$ mm^3 on a single dielectric layer, in contrast to the larger or multilayer implementations of prior work.

Table 3.2: Performance comparison with reported frequency-tunable and dual-band OAM antennas

Ref.	**[65]**	**[135]**	**[68]**	**[136]**	**This Work**
Frequency (GHz) and l	3.8 ($l = \pm1$) 4.0 ($l = \pm1$) 4.15 ($l = \pm1$)	3.8 ($l = \pm1$) 4.1 ($l = \pm1$) 4.4 ($l = \pm1$)	5.3 ($l = +1$) 5.77 ($l = +1$)	5.1 ($l = 0$) 5.6 ($l = -1$)	5.8 ($l = \pm1$) 28 ($l = \pm1$)
Type	Single-band (frequency-tunable)	Single-band (frequency-tunable)	Dual-band	Dual-band	Dual-band
Simultaneous microwave and mm-wave operation	No	No	No	No	Yes
Gain (dBi)	7.8–8.5	6.4–6.9	10	10.5 (at 5.1 GHz) 7.9 (at 5.6 GHz)	5.069 (at 5.8 GHz) 9.157 (at 28 GHz)
Isolation (dB)	> 20	> 20	Single port	> 34	> 30
Bandwidth (%)	1%	1%	5% (at 5.3 GHz) 6% (at 5.77 GHz)	2% (at 5.1 GHz) 2.5% (at 5.6 GHz)	11.9% (at 5.8 GHz) 2.7% (at 28 GHz)
Size (mm^3)	$155 \times 181 \times 0.762$	$123 \times 123 \times 1.524$	$150 \times 140 \times 1.6$	$80 \times 80 \times 2.2$	$88.8 \times 88.8 \times 0.508$
Substrate layers	1	2	1	3	1
Structure	UCA	UCA	UCA	UCA	UCA
Feeding network complexity	High	High	Medium	High	Low

Note: l = corresponding OAM modes.

- **Simple, mode-switchable feeding network:** Mode switching between $l = \pm1$ is realized through a symmetric dual-port scheme that requires no external phase-shifting networks, whereas earlier UCAs rely on more complex power-divider networks, varactor-tuned feeds, or other dedicated phase-shifting circuits.

Overall, the proposed single-layer UCAs deliver mode-switchable OAM operation simultaneously in the microwave (5.8 GHz) and mm-wave (28 GHz) bands, outperforming prior art with their smaller footprint, simpler feed, and consistently good matching and isolation.

3.5 Summary

This chapter presented the design and performance evaluation of a single-layer, dual-band, mode-switchable OAM antenna operating at 5.8 and 28 GHz. Section 3.1 defined the target requirements, including dual-band operation, OAM mode switching ($l = \pm1$) via a symmetric dual-port feed, compact single-layer structure, good impedance matching (reflection below –10 dB), and high port isolation (> 30 dB). Section 3.2 detailed the antenna configuration and working mechanism: two concentric UCAs with 8 elliptical patch elements each, rotated and series-fed to realize the required $\pm45°$ phase progression, and symmetric dual-port excitation for conjugate mode generation without external phase shifters. Geometric parameters on Rogers RO4350B were optimized for aperture

sharing and isolation. Section 3.3 described full-wave simulation and experimental validation: S-parameter measurements confirmed impedance matching and isolation at both bands; near-field scans demonstrated clear spiral phase and doughnut amplitude for $l = \pm 1$; far-field patterns exhibited axial nulls. Finally, in Section 3.4, a performance comparison highlighted the antenna's simultaneous microwave and mm-wave operation, compact footprint ($88.8 \times 88.8 \times 0.508$ mm^3), and simple feed network, outperforming prior designs. The results validate the feasibility of low-profile, dual-band, mode-switchable OAM antennas for integrated microwave and mm-wave wireless systems.

Chapter 4

Conclusion and Future Work

4.1 Summary of Research

This thesis presented the design, simulation, and experimental validation of a mode-switchable dual-band OAM antenna that operates at both 5.8 and 28 GHz. The proposed antenna employs a co-layer shared-aperture architecture and utilizes a symmetric dual-port feeding mechanism to enable conjugate mode switching between $l = \pm 1$ OAM states without requiring external phase-shifting circuits.

The main contributions are summarized as follows:

- A dual-band UCAs design was proposed to generate mode-switchable OAM beams at two frequency bands using a compact co-layer structure;
- A symmetric feeding strategy was implemented to switch between conjugate OAM modes, ensuring structural simplicity and high port isolation (>30 dB);
- Full-wave simulations and experimental measurements were conducted, including S-parameters, near-field amplitude and phase distributions, and far-field gain patterns, all confirming the antenna's dual-band OAM generation capabilities;

- A dual-band, mode-switchable OAM antenna solution was introduced for next-generation microwave and mm-wave wireless communication systems, supporting spectrum-efficient and mode-diverse transmission.

4.2 Future Work

While the proposed design demonstrates promising performance, several directions remain open for further investigation:

- **Higher-order OAM modes:** Future studies could explore the generation and reconfiguration of higher-order OAM modes (e.g., $l = \pm 2, \pm 3$, etc.) to further enhance spatial multiplexing capabilities;
- **OAM–MIMO hybrid systems:** Integrating OAM with MIMO architectures may enable three-dimensional spectral reuse across frequency, spatial, and mode domains, thereby improving overall system capacity;
- **System-level integration and real-world deployment:** Adapting the antenna for specific application scenarios—such as vehicular networks, indoor wireless coverage, or IoT systems—will require additional research on structural optimization, packaging, and environmental resilience.

In conclusion, OAM-based antennas hold significant potential for next-generation high-capacity wireless communication systems. The approach proposed in this thesis provides a compact and practical solution for dual-band OAM implementation and lays a solid foundation for future advancements in more complex and integrated communication architectures.

References

[1] W. Hong, Z. H. Jiang, C. Yu, D. Hou, H. Wang, C. Guo, Y. Hu, L. Kuai, Y. Yu, Z. Jiang *et al.*, "The role of millimeter-wave technologies in 5g/6g wireless communications," *IEEE Journal of Microwaves*, vol. 1, no. 1, pp. 101–122, 2021.

[2] C. Dehos, J. L. González, A. De Domenico, D. Ktenas, and L. Dussopt, "Millimeter-wave access and backhauling: The solution to the exponential data traffic increase in 5g mobile communications systems?" *IEEE Communications Magazine*, vol. 52, no. 9, pp. 88–95, 2014.

[3] D. Choudhury, "5g wireless and millimeter wave technology evolution: An overview," in *2015 IEEE MTT-S International Microwave Symposium*. IEEE, 2015, pp. 1–4.

[4] X. Wang, J. Hu, H. Lin, S. Garg, G. Kaddoum, M. J. Piran, and M. S. Hossain, "Qos and privacy-aware routing for 5g-enabled industrial internet of things: A federated reinforcement learning approach," *IEEE Transactions on Industrial Informatics*, vol. 18, no. 6, pp. 4189–4197, 2021.

[5] M. Aazam, K. A. Harras, and S. Zeadally, "Fog computing for 5g tactile industrial internet of things: Qoe-aware resource allocation model," *IEEE Transactions on Industrial Informatics*, vol. 15, no. 5, pp. 3085–3092, 2019.

[6] T. Zhang, Y. Xu, J. Loo, D. Yang, and L. Xiao, "Joint computation and communication design for uav-assisted mobile edge computing in iot," *IEEE Transactions on Industrial Informatics*, vol. 16, no. 8, pp. 5505–5516, 2019.

[7] C. Lin, G. Han, X. Qi, J. Du, T. Xu, and M. Martínez-García, "Energy-optimal data collection for unmanned aerial vehicle-aided industrial wireless sensor network-based agricultural monitoring system: A clustering compressed sampling approach," *IEEE Transactions on Industrial Informatics*, vol. 17, no. 6, pp. 4411–4420, 2020.

[8] M. R. Akdeniz, Y. Liu, M. K. Samimi, S. Sun, S. Rangan, T. S. Rappaport, and E. Erkip, "Millimeter wave channel modeling and cellular capacity evaluation," *IEEE Journal on Selected Areas in Communications*, vol. 32, no. 6, pp. 1164–1179, 2014.

[9] T. S. Rappaport, Y. Xing, G. R. MacCartney, A. F. Molisch, E. Mellios, and J. Zhang, "Overview of millimeter wave communications for fifth-generation (5g) wireless networks—with a focus on propagation models," *IEEE Transactions on Antennas and Propagation*, vol. 65, no. 12, pp. 6213–6230, 2017.

[10] Z. Pi and F. Khan, "An introduction to millimeter-wave mobile broadband systems," *IEEE Communications Magazine*, vol. 49, no. 6, pp. 101–107, 2011.

[11] Y.-P. Zhang, P. Wang, and A. Goldsmith, "Rainfall effect on the performance of millimeter-wave mimo systems," *IEEE Transactions on Wireless Communications*, vol. 14, no. 9, pp. 4857–4866, 2015.

[12] G. R. MacCartney Jr, S. Sun, T. S. Rappaport, Y. Xing, H. Yan, J. Koka, R. Wang, and D. Yu, "Millimeter wave wireless communications: New results for rural connectivity," in *Proceedings of the 5th workshop on all things cellular: operations, applications and challenges*, 2016, pp. 31–36.

[13] R. W. Heath, N. Gonzalez-Prelcic, S. Rangan, W. Roh, and A. M. Sayeed, "An overview of signal processing techniques for millimeter wave mimo systems," *IEEE Journal of Selected Topics in Signal Processing*, vol. 10, no. 3, pp. 436–453, 2016.

[14] A. Ghosh, "The 5g mmwave radio revolution," *Microwave Journal*, vol. 5, no. 1, pp. 4–9, 2017.

[15] J. Lee, E. Tejedor, K. Ranta-aho, H. Wang, K.-T. Lee, E. Semaan, E. Mohyeldin, J. Song, C. Bergljung, and S. Jung, "Spectrum for 5g: Global status, challenges, and enabling technologies," *IEEE Communications Magazine*, vol. 56, no. 3, pp. 12–18, 2018.

[16] M. Agiwal, A. Roy, and N. Saxena, "Next generation 5g wireless networks: A comprehensive survey," *IEEE Communications Surveys & Tutorials*, vol. 18, no. 3, pp. 1617–1655, 2016.

[17] M. Series, "Imt vision–framework and overall objectives of the future development of imt for 2020 and beyond," *Recommendation ITU*, vol. 2083, no. 0, pp. 1–21, 2015.

[18] 3GPP, "Study on scenarios and requirements for next generation access technologies," *Tech. Rep. TR38.913*, 2016.

[19] A. F. Molisch, V. V. Ratnam, S. Han, Z. Li, S. L. H. Nguyen, L. Li, and K. Haneda, "Hybrid beamforming for massive mimo: A survey," *IEEE Communications Magazine*, vol. 55, no. 9, pp. 134–141, 2017.

[20] M. Shafi, A. F. Molisch, P. J. Smith, T. Haustein, P. Zhu, P. De Silva, F. Tufvesson, A. Benjebbour, and G. Wunder, "5g: A tutorial overview of standards, trials, challenges, deployment, and practice," *IEEE Journal on Selected Areas in Communications*, vol. 35, no. 6, pp. 1201–1221, 2017.

[21] T. Bai and R. W. Heath, "Coverage and rate analysis for millimeter-wave cellular networks," *IEEE Transactions on Wireless Communications*, vol. 14, no. 2, pp. 1100–1114, 2014.

[22] S. Rangan, T. S. Rappaport, and E. Erkip, "Millimeter-wave cellular wireless networks: Potentials and challenges," *Proceedings of the IEEE*, vol. 102, no. 3, pp. 366–385, 2014.

[23] ITU-R, "Future technology trends of terrestrial imt systems towards 2030 and beyond," International Telecommunication Union, ITU-R Report M.2472-0, 2020.

[24] J. G. Andrews, S. Buzzi, W. Choi, S. V. Hanly, A. Lozano, A. C. Soong, and J. C. Zhang, "What will 5g be?" *IEEE Journal on Selected Areas in Communications*, vol. 32, no. 6, pp. 1065–1082, 2014.

[25] G. Geraci, A. Garcia-Rodriguez, M. M. Azari, A. Lozano, M. Mezzavilla, S. Chatzinotas, Y. Chen, S. Rangan, and M. Di Renzo, "What will the future of uav cellular communications be? a flight from 5g to 6g," *IEEE Communications Surveys & Tutorials*, vol. 24, no. 3, pp. 1304–1335, 2022.

[26] W. Roh, J.-Y. Seol, J. Park, B. Lee, J. Lee, Y. Kim, J. Cho, K. Cheun, and F. Aryanfar, "Millimeter-wave beamforming as an enabling technology for 5g cellular communications: Theoretical feasibility and prototype results," *IEEE Communications Magazine*, vol. 52, no. 2, pp. 106–113, 2014.

[27] S. Kutty and D. Sen, "Beamforming for millimeter wave communications: An inclusive survey," *IEEE Communications Surveys & Tutorials*, vol. 18, no. 2, pp. 949–973, 2015.

[28] H. Shokri-Ghadikolaei, C. Fischione, G. Fodor, P. Popovski, and M. Zorzi, "Millimeter wave cellular networks: A mac layer perspective," *IEEE Transactions on Communications*, vol. 63, no. 10, pp. 3437–3458, 2015.

[29] J. Deng, O. Tirkkonen, R. Freij-Hollanti, T. Chen, and N. Nikaein, "Resource allocation and interference management for opportunistic relaying in integrated mmwave/sub-6 ghz 5g networks," *IEEE Communications Magazine*, vol. 55, no. 6, pp. 94–101, 2017.

[30] Y. Zhu, G. Zheng, L. Wang, K.-K. Wong, and L. Zhao, "Content placement in cache-enabled sub-6 ghz and millimeter-wave multi-antenna dense small cell networks," *IEEE Transactions on Wireless Communications*, vol. 17, no. 5, pp. 2843–2856, 2018.

[31] T. S. Rappaport, S. Sun, R. Mayzus, H. Zhao, Y. Azar, K. Wang, G. N. Wong, J. K. Schulz, M. Samimi, and F. Gutierrez, "Millimeter wave mobile communications for 5g cellular: It will work!" *IEEE Access*, vol. 1, pp. 335–349, 2013.

[32] M. Xiao, S. Mumtaz, Y. Huang, L. Dai, Y. Li, M. Matthaiou, G. K. Karagiannidis, E. Björnson, K. Yang, I. Chih-Lin *et al.*, "Millimeter wave communications for future mobile networks," *IEEE Journal on Selected Areas in Communications*, vol. 35, no. 9, pp. 1909–1935, 2017.

[33] Z. Ren, A. Zhao, and S. Wu, "Mimo antenna with compact decoupled antenna pairs for 5g mobile terminals," *IEEE Antennas and Wireless Propagation Letters*, vol. 18, no. 7, pp. 1367–1371, 2019.

[34] W. Hong, K.-H. Baek, and S. Ko, "Millimeter-wave 5g antennas for smartphones: Overview and experimental demonstration," *IEEE Transactions on Antennas and Propagation*, vol. 65, no. 12, pp. 6250–6261, 2017.

[35] S. Loyka and C. D. Charalambous, "A general formula for compound channel capacity," *IEEE Transactions on Information Theory*, vol. 62, no. 7, pp. 3971–3991, 2016.

[36] C. E. Shannon, "A mathematical theory of communication," *The Bell System Technical Journal*, vol. 27, no. 3, pp. 379–423, 1948.

[37] L. Hanlen and A. Grant, "Capacity analysis of correlated mimo channels," *IEEE Transactions on Information Theory*, vol. 58, no. 11, pp. 6773–6787, 2012.

[38] T. Yoo and A. Goldsmith, "Capacity and power allocation for fading mimo channels with channel estimation error," *IEEE Transactions on Information Theory*, vol. 52, no. 5, pp. 2203–2214, 2006.

[39] F. Rusek, D. Persson, B. K. Lau, E. G. Larsson, T. L. Marzetta, O. Edfors, and F. Tufvesson, "Scaling up mimo: Opportunities and challenges with very large arrays," *IEEE Signal Processing Magazine*, vol. 30, no. 1, pp. 40–60, 2012.

[40] A. Lozano and N. Jindal, "Transmit diversity vs. spatial multiplexing in modern mimo systems," *IEEE Transactions on Wireless Communications*, vol. 9, no. 1, pp. 186–197, 2010.

[41] A. M. Yao and M. J. Padgett, "Orbital angular momentum: origins, behavior and applications," *Advances in Optics and Photonics*, vol. 3, no. 2, pp. 161–204, 2011.

[42] W. Zhang, S. Zheng, Y. Chen, X. Jin, H. Chi, and X. Zhang, "Orbital angular momentum-based communications with partial arc sampling receiving," *IEEE Communications Letters*, vol. 20, no. 7, pp. 1381–1384, 2016.

[43] R. Chen, H. Zhou, M. Moretti, X. Wang, and J. Li, "Orbital angular momentum waves: Generation, detection, and emerging applications," *IEEE Communications Surveys & Tutorials*, vol. 22, no. 2, pp. 840–868, 2019.

[44] N. Ahmed, Z. Zhao, L. Li, H. Huang, M. P. Lavery, P. Liao, Y. Yan, Z. Wang, G. Xie, Y. Ren *et al.*, "Mode-division-multiplexing of multiple bessel-gaussian beams carrying orbital-angular-momentum for obstruction-tolerant free-space optical and millimetre-wave communication links," *Scientific Reports*, vol. 6, no. 1, pp. 1–10, 2016.

[45] F. Tamburini, E. Mari, A. Sponselli, B. Thidé, A. Bianchini, and F. Romanato, "Encoding many channels on the same frequency through radio vorticity: first experimental test," *New Journal of Physics*, vol. 14, no. 3, pp. 1–18, 2012.

[46] A. E. Willner, J. Wang, and H. Huang, "A different angle on light communications," *Science*, vol. 337, no. 6095, pp. 655–656, 2012.

[47] J. Wang, J.-Y. Yang, I. M. Fazal, N. Ahmed, Y. Yan, H. Huang, Y. Ren, Y. Yue, S. Dolinar, M. Tur *et al.*, "Terabit free-space data transmission employing orbital angular momentum multiplexing," *Nature Photonics*, vol. 6, no. 7, pp. 488–496, 2012.

[48] Y. Yan, G. Xie, M. P. Lavery, H. Huang, N. Ahmed, C. Bao, Y. Ren, Y. Cao, L. Li, Z. Zhao *et al.*, "High-capacity millimetre-wave communications with orbital angular momentum multiplexing," *Nature Communications*, vol. 5, no. 1, pp. 1–9, 2014.

[49] X. Hui, S. Zheng, Y. Chen, Y. Hu, X. Jin, H. Chi, and X. Zhang, "Multiplexed millimeter wave communication with dual orbital angular momentum (oam) mode antennas," *Scientific Reports*, vol. 5, no. 1, pp. 1–9, 2015.

[50] P. Xu, H. Liu, R. Li, K. Zhang, and L. Li, "Dual-band spin-decoupled metasurface for generating multiple coaxial oam beams," *IEEE Transactions on Antennas and Propagation*, vol. 70, no. 11, pp. 10 678–10 690, 2022.

[51] W. Cheng, W. Zhang, H. Jing, S. Gao, and H. Zhang, "Orbital angular momentum for wireless communications," *IEEE Wireless Communications*, vol. 26, no. 1, pp. 100–107, 2019.

[52] J. Li, X. Kong, J. Wang, Z. Miao, X. Wang, X. Shen, and L. Zhao, "Dual-band polarization-insensitive orbital angular momentum beam generation based on 1-bit polarization-converting transmitting coding metasurface," *International Journal of RF and Microwave Computer-Aided Engineering*, vol. 32, no. 11, pp. 1–8, 2022.

[53] S. Iqbal, S. Liu, J. Luo, L. Zhang, H. A. Madni, and T. J. Cui, "Controls of transmitted electromagnetic waves for diverse functionalities using polarization-selective dual-band 2 bit coding metasurface," *Journal of Optics*, vol. 22, no. 1, pp. 1–14, 2019.

[54] J. Zhu, Y. Yang, S. Liao, and Q. Xue, "Aperture-shared millimeter-wave/sub-6 ghz dual-band antenna hybridizing fabry–pérot cavity and fresnel zone plate," *IEEE Transactions on Antennas and Propagation*, vol. 69, no. 12, pp. 8170–8181, 2021.

[55] J. F. Zhang, Y. J. Cheng, Y. R. Ding, and C. X. Bai, "A dual-band shared-aperture antenna with large frequency ratio, high aperture reuse efficiency, and high channel isolation," *IEEE Transactions on Antennas and Propagation*, vol. 67, no. 2, pp. 853–860, 2019.

[56] Y. Cheng and Y. Dong, "Dual-broadband dual-polarized shared-aperture magnetoelectric dipole antenna for 5g applications," *IEEE Transactions on Antennas and Propagation*, vol. 69, no. 11, pp. 7918–7923, 2021.

[57] C. Wang, W. Cao, W. Ma, Y. Tong, and Y. Zhu, "A sigle-layer dual-band shared-aperture antenna with high gain and sidelobe suppression based on high-order mode for vehicular communications," *IEEE Transactions on Vehicular Technology*, vol. 73, no. 1, pp. 473–481, 2024.

[58] D. E. Serup, G. F. Pedersen, and S. Zhang, "Dual-band shared aperture reflectarray and patch antenna array for s- and ka-bands," *IEEE Transactions on Antennas and Propagation*, vol. 70, no. 3, pp. 2340–2345, 2022.

[59] M. Ikram, N. Nguyen-Trong, and A. Abbosh, "Multiband mimo microwave and millimeter antenna system employing dual-function tapered slot structure," *IEEE Transactions on Antennas and Propagation*, vol. 67, no. 8, pp. 5705–5710, 2019.

[60] Q. Liu, Z. N. Chen, Y. Liu, F. Li, Y. Chen, and Z. Mo, "Circular polarization and mode reconfigurable wideband orbital angular momentum patch array antenna," *IEEE Transactions on Antennas and Propagation*, vol. 66, no. 4, pp. 1796–1804, 2018.

[61] C. Deng, K. Zhang, and Z. Feng, "Generating and measuring tunable orbital angular momentum radio beams with digital control method," *IEEE Transactions on Antennas and Propagation*, vol. 65, no. 2, pp. 899–902, 2016.

[62] H. Naseri, P. PourMohammadi, N. Melouki, A. Iqbal, and T. A. Denidni, "A low-profile antenna system for generating reconfigurable oam-carrying beams," *IEEE Antennas and Wireless Propagation Letters*, vol. 22, no. 2, pp. 402–406, 2022.

[63] L. Kang, H. Li, J. Zhou, and S. Zheng, "An oam-mode reconfigurable array antenna with polarization agility," *IEEE Access*, vol. 8, pp. 40 445–40 452, 2020.

[64] H. Li, L. Kang, and K. Dong, "Generating tunable orbital angular momentum radio beams with dual-circular-polarization and dual-mode characteristics," *IEEE Access*, vol. 8, pp. 211 248–211 254, 2020.

[65] H. Naseri, P. Pourmohammadi, N. Melouki, F. Ahmed, A. Iqbal, and T. Denidni, "Frequency-adjustable oam antenna with co-divergent beams for iot applications," *AEU-International Journal of Electronics and Communications*, vol. 177, pp. 1–10, 2024.

[66] H. Naseri, P. PourMohammadi, N. Melouki, F. Ahmed, A. Iqbal, and T. A. Denidni, "Reconfigurable oam antenna with flexibility on mode numbers, polarization, and frequency," *IEEE Antennas and Wireless Propagation Letters*, vol. 23, no. 6, pp. 1710–1714, 2024.

[67] B. Liu, Y. Cui, and R. Li, "A broadband dual-polarized dual-oam-mode antenna array for oam communication," *IEEE Antennas and Wireless Propagation Letters*, vol. 16, pp. 744–747, 2016.

[68] M. V. Rao, Y. B. Modugu, D. Mondal, S. Yuvaraj, and M. Kartikeyan, "Generation of dual-band oam beam using planar uniform circular array for vehicular communications," *Microwave and Optical Technology Letters*, vol. 66, no. 1, pp. 1–6, 2024.

[69] H. Li, L. Kang, and R. Chen, "Design of a shared-aperture co-polarized antenna with minimal mutual coupling for practical integration in a dual-mode oam array," *IEEE Transactions on Circuits and Systems II: Express Briefs*, vol. 71, no. 10, pp. 4456–4460, 2024.

[70] F. Tamburini, E. Mari, B. Thidé, C. Barbieri, and F. Romanato, "Experimental verification of photon angular momentum and vorticity with radio techniques," *Applied Physics Letters*, vol. 99, no. 20, 2011.

[71] E. Mari, F. Spinello, M. Oldoni, R. A. Ravanelli, F. Romanato, and G. Parisi, "Near-field experimental verification of separation of oam channels," *IEEE Antennas and Wireless Propagation Letters*, vol. 14, pp. 556–558, 2014.

[72] F. Tamburini, B. Thidé, V. Boaga, F. Carraro, M. Del Pup, A. Bianchini, C. Someda, and F. Romanato, "Experimental demonstration of free-space information transfer using phase modulated orbital angular momentum radio," *arXiv preprint arXiv:1302.2990*, 2013.

[73] M. Barbuto, F. Trotta, F. Bilotti, and A. Toscano, "Circular polarized patch antenna generating orbital angular momentum," *Progress In Electromagnetics Research*, vol. 148, pp. 23–30, 2014.

[74] D. S. Gyan, K. P. Ray, and A. K. Poddar, "Generation of higher-order oam waves with single-point fed circular microstrip antenna using bifurcated cylindrical harmonics," *IEEE Transactions on Antennas and Propagation*, vol. 72, no. 9, pp. 6950–6958, 2024.

[75] Z. Zhang, S. Xiao, Y. Li, and B.-Z. Wang, "A circularly polarized multimode patch antenna for the generation of multiple orbital angular momentum modes," *IEEE Antennas and Wireless Propagation Letters*, vol. 16, pp. 521–524, 2017.

[76] X. He, L. Deng, B. Feng, K. L. Chung, L. Yin, and L. Chen, "Angular momentum multiplexing via a shared aperture patch antenna," *IEEE Transactions on Antennas and Propagation*, vol. 71, no. 7, pp. 5532–5541, 2023.

[77] Z. He, Y. Wang, X. Wang, A. S. Kupriianov, V. R. Tuz, and V. I. Fesenko, "Multi-band orbital angular momentum mode-division multiplexing by a compact set of microstrip ring-shaped resonator antenna," *Optics Express*, vol. 30, no. 26, pp. 46 209–46 226, 2022.

[78] J. J. Chen, Q. N. Lu, F. F. Dong, J. J. Yang, and M. Huang, "Wireless oam transmission system based on elliptical microstrip patch antenna," *Optics Express*, vol. 24, no. 11, pp. 11 531–11 538, 2016.

[79] S. Zheng, X. Hui, X. Jin, H. Chi, and X. Zhang, "Transmission characteristics of a twisted radio wave based on circular traveling-wave antenna," *IEEE Transactions on Antennas and Propagation*, vol. 63, no. 4, pp. 1530–1536, 2015.

[80] W. Zhang, S. Zheng, X. Hui, R. Dong, X. Jin, H. Chi, and X. Zhang, "Mode division multiplexing communication using microwave orbital angular momentum: An experimental study," *IEEE Transactions on Wireless Communications*, vol. 16, no. 2, pp. 1308–1318, 2017.

[81] G. Junkin, "A circularly polarized single-frequency multimode helical beam antenna," *IEEE Transactions on Antennas and Propagation*, vol. 67, no. 3, pp. 1459–1466, 2019.

[82] Y. Chen, S. Zheng, H. Chi, X. Jin, and X. Zhang, "Half-mode substrate integrated waveguide antenna for generating multiple orbital angular momentum modes," *Electronics Letters*, vol. 52, no. 9, pp. 684–686, 2016.

[83] Y. Chen, S. Zheng, Y. Li, X. Hui, X. Jin, H. Chi, and X. Zhang, "A flat-lensed spiral phase plate based on phase-shifting surface for generation of millimeter-wave oam beam," *IEEE Antennas and Wireless Propagation Letters*, vol. 15, pp. 1156–1158, 2016.

[84] S. Yu, L. Li, G. Shi, C. Zhu, and Y. Shi, "Generating multiple orbital angular momentum vortex beams using a metasurface in radio frequency domain," *Applied Physics Letters*, vol. 108, no. 24, 2016.

[85] Y. Shuang, H. Zhao, W. Ji, T. J. Cui, and L. Li, "Programmable high-order oam-carrying beams for direct-modulation wireless communications," *IEEE Journal on Emerging and Selected Topics in Circuits and Systems*, vol. 10, no. 1, pp. 29–37, 2020.

[86] H.-F. Huang and S.-N. Li, "High-efficiency planar reflectarray with small-size for oam generation at microwave range," *IEEE Antennas and Wireless Propagation Letters*, vol. 18, no. 3, pp. 432–436, 2019.

[87] G. Ding, K. Chen, X. Luo, J. Zhao, T. Jiang, and Y. Feng, "Dual-helicity decoupled coding metasurface for independent spin-to-orbital angular momentum conversion," *Physical Review Applied*, vol. 11, no. 4, pp. 1–11, 2019.

[88] Z. H. Jiang, L. Kang, W. Hong, and D. H. Werner, "Highly efficient broadband multiplexed millimeter-wave vortices from metasurface-enabled transmit-arrays of subwavelength thickness," *Physical Review Applied*, vol. 9, no. 6, pp. 1–13, 2018.

[89] M. L. Chen, L. J. Jiang, and E. Wei, "Ultrathin complementary metasurface for orbital angular momentum generation at microwave frequencies," *IEEE Transactions on Antennas and Propagation*, vol. 65, no. 1, pp. 396–400, 2016.

[90] M. L. Chen, L. J. Jiang, and W. E. Sha, "Artificial perfect electric conductor-perfect magnetic conductor anisotropic metasurface for generating orbital angular momentum of microwave with nearly perfect conversion efficiency," *Journal of Applied Physics*, vol. 119, no. 6, 2016.

[91] J. Liang and S. Zhang, "Orbital angular momentum (oam) generation by cylinder dielectric resonator antenna for future wireless communications," *IEEE Access*, vol. 4, pp. 9570–9574, 2016.

[92] Z. Yu, N. Guo, and J. Fan, "Water spiral dielectric resonator antenna for generating multimode oam," *IEEE Antennas and Wireless Propagation Letters*, vol. 19, no. 4, pp. 601–605, 2020.

[93] Y. Pan, S. Zheng, J. Zheng, Y. Li, X. Jin, H. Chi, and X. Zhang, "Generation of orbital angular momentum radio waves based on dielectric resonator antenna," *IEEE Antennas and Wireless Propagation Letters*, vol. 16, pp. 385–388, 2017.

[94] T. Zhihong, Y. P. Zhang, C. Luxey, A. Bisognin, D. Titz, and F. Ferrero, "A ceramic antenna for tri-band radio devices," *IEEE Transactions on Antennas and Propagation*, vol. 61, no. 11, pp. 5776–5780, 2013.

[95] L. Zhang, K. Y. See, B. Zhang, and Y. P. Zhang, "Integration of dual-band monopole and microstrip grid array for single-chip tri-band application," *IEEE Transactions on Antennas and Propagation*, vol. 61, no. 1, pp. 439–443, 2013.

[96] D. Wang and C. H. Chan, "Multiband antenna for wifi and wigig communications," *IEEE Antennas and Wireless Propagation Letters*, vol. 15, pp. 309–312, 2016.

[97] X.-H. Ding, W.-W. Yang, W. Qin, and J.-X. Chen, "A broadside shared aperture antenna for (3.5, 26) ghz mobile terminals with steerable beam in millimeter-waveband," *IEEE Transactions on Antennas and Propagation*, vol. 70, no. 3, pp. 1806–1815, 2022.

[98] X.-H. Ding, W.-W. Yang, H. Tang, L. Guo, and J.-X. Chen, "A dual-band shared-aperture antenna for microwave and millimeter-wave applications in 5g wireless communication," *IEEE Transactions on Antennas and Propagation*, vol. 70, no. 12, pp. 12 299–12 304, 2022.

[99] Y. Wang and F. Xu, "Shared aperture 4g lte and 5g mm-wave antenna in mobile phones with enhanced mm-wave radiation in the display direction," *IEEE Transactions on Antennas and Propagation*, vol. 71, no. 6, pp. 4772–4782, 2023.

[100] X. Yang, G. Zhang, Y. Ji, Z. Zhang, L. Ge, C.-Y.-D. Sim, and W. He, "Joint microwave and millimeter-wave antenna design for uav-enabled communications," *IEEE Transactions on Industrial Informatics*, vol. 19, no. 11, pp. 10 739–10 750, 2023.

[101] Y.-X. Sun and K. W. Leung, "Substrate-integrated two-port dual-frequency antenna," *IEEE Transactions on Antennas and Propagation*, vol. 64, no. 8, pp. 3692–3697, 2016.

[102] P. Mei, S. Zhang, and G. F. Pedersen, "A dual-polarized and high-gain x-/ka-band shared-aperture antenna with high aperture reuse efficiency," *IEEE Transactions on Antennas and Propagation*, vol. 69, no. 3, pp. 1334–1344, 2021.

[103] J. Ren, Z. Wang, Y.-X. Sun, R. Huang, and Y. Yin, "Ku/ka-band dual-frequency shared-aperture antenna array with high isolation using frequency selective surface," *IEEE Antennas and Wireless Propagation Letters*, vol. 22, no. 7, pp. 1736–1740, 2023.

[104] B. J. Xiang, S. Y. Zheng, H. Wong, Y. M. Pan, K. X. Wang, and M. H. Xia, "A flexible dual-band antenna with large frequency ratio and different radiation properties over the two bands," *IEEE Transactions on Antennas and Propagation*, vol. 66, no. 2, pp. 657–667, 2018.

[105] L. Allen, M. W. Beijersbergen, R. Spreeuw, and J. Woerdman, "Orbital angular momentum of light and the transformation of laguerre-gaussian laser modes," *Physical Review A*, vol. 45, no. 11, pp. 1–6, 1992.

[106] A. M. Yao and M. J. Padgett, "Orbital angular momentum: origins, behavior and applications," *Advances in Optics and Photonics*, vol. 3, no. 2, pp. 161–204, 2011.

[107] A. E. Willner, H. Huang, Y. Yan, Y. Ren, N. Ahmed, G. Xie, C. Bao, L. Li, Y. Cao, Z. Zhao *et al.*, "Optical communications using orbital angular momentum beams," *Advances in Optics and Photonics*, vol. 7, no. 1, pp. 66–106, 2015.

[108] S. Zheng, X. Hui, J. Zhu, H. Chi, X. Jin, S. Yu, and X. Zhang, "Orbital angular momentum mode-demultiplexing scheme with partial angular receiving aperture," *Optics Express*, vol. 23, no. 9, pp. 12 251–12 257, 2015.

[109] G. A. Turnbull, D. A. Robertson, G. M. Smith, L. Allen, and M. Padgett, "The generation of free-space laguerre-gaussian modes at millimetre-wave frequencies by use of a spiral phaseplate," *Optics Communications*, vol. 127, no. 4-6, pp. 183–188, 1996.

[110] J. A. Anguita, M. A. Neifeld, and B. V. Vasic, "Turbulence-induced channel crosstalk in an orbital angular momentum-multiplexed free-space optical link," *Applied Optics*, vol. 47, no. 13, pp. 2414–2429, 2008.

[111] J. Lin, X.-C. Yuan, S. Tao, and R. Burge, "Multiplexing free-space optical signals using superimposed collinear orbital angular momentum states," *Applied Optics*, vol. 46, no. 21, pp. 4680–4685, 2007.

[112] A. H. Dorrah, M. Zamboni-Rached, and M. Mojahedi, "Experimental demonstration of tunable refractometer based on orbital angular momentum of longitudinally structured light," *Light: Science & Applications*, vol. 7, no. 1, pp. 1–12, 2018.

[113] X. Sun and I. B. Djordjevic, "Physical-layer security in orbital angular momentum multiplexing free-space optical communications," *IEEE Photonics Journal*, vol. 8, no. 1, pp. 1–10, 2016.

[114] F. Zhu, S. Huang, W. Shao, J. Zhang, M. Chen, W. Zhang, and J. Zeng, "Free-space optical communication link using perfect vortex beams carrying orbital angular momentum (oam)," *Optics Communications*, vol. 396, pp. 50–57, 2017.

[115] G. Gibson, J. Courtial, M. J. Padgett, M. Vasnetsov, V. Pas'ko, S. M. Barnett, and S. Franke-Arnold, "Free-space information transfer using light beams carrying orbital angular momentum," *Optics Express*, vol. 12, no. 22, pp. 5448–5456, 2004.

[116] A. E. Willner, J. Wang, and H. Huang, "A different angle on light communications," *Science*, vol. 337, no. 6095, pp. 655–656, 2012.

[117] J. Wang, J.-Y. Yang, I. M. Fazal, N. Ahmed, Y. Yan, H. Huang, Y. Ren, Y. Yue, S. Dolinar, M. Tur *et al.*, "Terabit free-space data transmission employing orbital angular momentum multiplexing," *Nature Photonics*, vol. 6, no. 7, pp. 488–496, 2012.

[118] B. Thidé, H. Then, J. Sjöholm, K. Palmer, J. Bergman, T. Carozzi, Y. N. Istomin, . f. N. Ibragimov, and R. Khamitova, "Utilization of photon orbital angular momentum in the low-frequency radio domain," *Physical Review Letters*, vol. 99, no. 8, pp. 1–4, 2007.

[119] F. E. Mahmouli and S. D. Walker, "4-gbps uncompressed video transmission over a 60-ghz orbital angular momentum wireless channel," *IEEE Wireless Communications Letters*, vol. 2, no. 2, pp. 223–226, 2013.

[120] H. Sasaki, D. Lee, H. Fukumoto, Y. Yagi, T. Kaho, H. Shiba, and T. Shimizu, "Experiment on over-100-gbps wireless transmission with oam-mimo multiplexing system in 28-ghz band," in *2018 IEEE Global Communications Conference (GLOBECOM)*, 2018, pp. 1–6.

[121] Y. Yagi, H. Sasaki, T. Yamada, and D. Lee, "200 gb/s wireless transmission using dual-polarized oam-mimo multiplexing with uniform circular array on 28 ghz band," *IEEE Antennas and Wireless Propagation Letters*, vol. 20, no. 5, pp. 833–837, 2021.

[122] Y. Yagi, H. Sasaki, T. Semoto, T. Kageyama, T. Yamada, J. Mashino, and D. Lee, "Field experiment of 117 gbit/s wireless transmission using oam multiplexing at a distance of 200 m on 40 ghz band," in *2021 IEEE International Conference on Communications Workshops (ICC Workshops)*, 2021, pp. 1–5.

[123] K. Liu, Y. Cheng, Z. Yang, H. Wang, Y. Qin, and X. Li, "Orbital-angular-momentum-based electromagnetic vortex imaging," *IEEE Antennas and Wireless Propagation Letters*, vol. 14, pp. 711–714, 2014.

[124] S. Franke-Arnold, L. Allen, and M. Padgett, "Advances in optical angular momentum," *Laser & Photonics Reviews*, vol. 2, no. 4, pp. 299–313, 2008.

[125] S. M. Barnett, "Optical angular-momentumflux," *Journal of Optics B: Quantum and Semiclassical Optics*, vol. 4, no. 2, pp. 1–11, 2001.

[126] S. M. Mohammadi, L. K. S. Daldorff, J. E. S. Bergman, R. L. Karlsson, B. Thide, K. Forozesh, T. D. Carozzi, and B. Isham, "Orbital angular momentum in radio—a system study," *IEEE Transactions on Antennas and Propagation*, vol. 58, no. 2, pp. 565–572, 2010.

[127] J. Humblet, "Sur le moment d'impulsion d'une onde électromagnétique," *Physica*, vol. 10, no. 7, pp. 585–603, 1943.

[128] R. A. Beth, "Mechanical detection and measurement of the angular momentum of light," *Physical Review*, vol. 50, no. 2, pp. 1–13, 1936.

[129] Y. Zhao, J. S. Edgar, G. D. Jeffries, D. McGloin, and D. T. Chiu, "Spin-to-orbital angular momentum conversion in a strongly focused optical beam," *Physical Review Letters*, vol. 99, no. 7, pp. 1–4, 2007.

[130] L. Allen, M. Padgett, and M. Babiker, "Iv the orbital angular momentum of light," in *Progress in Optics*. Elsevier, 1999, vol. 39, pp. 291–372.

[131] S. M. Barnett and L. Allen, "Orbital angular momentum and nonparaxial light beams," *Optics Communications*, vol. 110, no. 5-6, pp. 670–678, 1994.

[132] A. E. Willner, H. Song, K. Zou, H. Zhou, and X. Su, "Orbital angular momentum beams for high-capacity communications," *Journal of Lightwave Technology*, vol. 41, no. 7, pp. 1918–1933, 2023.

[133] M. V. Rao, D. Mondal, J. Malik, M. Kartikeyan, and S. Yuvaraj, "Series-feed uca antenna for generating highly azimuthal symmetric oam beam for unmanned aerial vehicles," *AEU-International Journal of Electronics and Communications*, vol. 171, pp. 1–6, 2023.

[134] C. A. Balanis, *Antenna Theory: Analysis and Design*, 4th ed. John Wiley & Sons, 2016, pp. 363–364.

[135] H. Naseri, P. PourMohammadi, N. Melouki, F. Ahmed, A. Iqbal, and T. A. Denidni, "Reconfigurable oam antenna with flexibility on mode numbers, polarization, and frequency," *IEEE Antennas and Wireless Propagation Letters*, vol. 23, no. 6, pp. 1710–1714, 2024.

[136] H. Li, L. Kang, and R. Chen, "Design of a shared-aperture co-polarized antenna with minimal mutual coupling for practical integration in a dual-mode oam array," *IEEE Transactions on Circuits and Systems II: Express Briefs*, vol. 71, no. 10, pp. 4456–4460, 2024.